PONTIFICAL CATHOLIC UNIVERSITY OF MINAS GERAIS
Graduate Program in Mechanical Engineering

Pedro Augusto Ramos

HIGH TEMPERATURE OXIDATION BEHAVIOR OF NOVEL NB-MODIFIED HEAT-RESISTANT CAST AUSTENITIC STAINLESS STEEL

Belo Horizonte
2021

Pedro Augusto Ramos

HIGH TEMPERATURE OXIDATION BEHAVIOR OF NOVEL NB-MODIFIED HEAT-RESISTANT CAST AUSTENITIC STAINLESS STEEL

Thesis presented as part of the graduate program in Mechanical Engineering at the Pontifical Catholic University of Minas Gerais, as a partial requirement to obtain a doctoral degree in Mechanical Engineering.

Advisor: Prof. Dr. Ing. Pedro Paiva Brito

Research line: Materials and manufacturing processes

Belo Horizonte

2021

FICHA CATALOGRÁFICA
Elaborada pela Biblioteca da Pontifícia Universidade Católica de Minas Gerais

Ramos, Pedro Augusto
R175h High temperature oxidation behavior of novel NB-modified heat-resistant cast austenitic stainless steel / Pedro Augusto Ramos. Belo Horizonte, 2021.
109 f. : il.

Orientador: Pedro Paiva Brito
Tese (Doutorado) – Pontifícia Universidade Católica de Minas Gerais. Programa de Pós-Graduação em Engenharia Mecânica

1. Aço inoxidável. 2. Aço austenítico. 3. Nióbio. 4. Metais - Propriedades mecanicas. 5. Aço - Tratamento térmico. 6. Aço - Corrosão. 7. Resistência de materiais. 8. Microestrutura. 9. Tensões residuais. 10. Oxidação. I. Brito, Pedro Paiva. II. Pontifícia Universidade Católica de Minas Gerais. Programa de Pós-Graduação em Engenharia Mecânica. III. Título.

CDU: 669.14

Ficha catalográfica elaborada por Fabiana Marques de Souza e Silva - CRB 6/2086

Pedro Augusto Ramos

HIGH TEMPERATURE OXIDATION BEHAVIOR OF NOVEL NB-MODIFIED HEAT-RESISTANT CAST AUSTENITIC STAINLESS STEEL

Thesis presented as part of the graduate program in Mechanical Engineering at the Pontifical Catholic University of Minas Gerais, as a partial requirement to obtain a doctoral degree in Mechanical Engineering.

_____

Prof. Dr. Ing. Pedro Paiva Brito – PUC Minas (Orientador)

_____

Prof. Dr. José Rubens Gonçalves Carneiro – PUC Minas (Membro interno)

_____

Prof.ª Dr.ª Sara Silva Ferreira de Dafé – PUC Minas (Membro interno)

_____

Prof.ª Dr.ª Vanessa de Freitas Cunha Lins – UFMG (Membro externo)

_____

Prof. Dr. Carlos Alberto Della Rovere – UFSCar (Membro externo)

Belo Horizonte, August 13, 2021.

ACKNOWLEDGEMENTS

First and foremost, I thank God, He who supported me, gave me strength and guidance during all the moments of this work, and to Mary Most Holy, Mother of God, for her powerful intercession for my needs.

I thank my parents, Wilson and Gislene, for encouraging me on the path of education as a way to improve the society in which we live and become a better and more capable person.

I am grateful to my wife, Amanda, who gave me strength during all the stages of this endeavor, which was a challenge for both of us, especially since we faced this challenge together during the first years of our married life.

I am grateful to the experts and teachers who advised me in order to enable and improve and this research, especially my advisor Prof. Pedro Paiva Brito who always encouraged me, patiently assisted me, and bolstered my confidence in the difficult moments of this work.

Thanks are due to all of my friends, teachers and collaborators of PUC Minas and the University of Saarland (Germany), who contributed to my efforts thoughfully, provided me with structure and assisted me in the execution of the essays, especially to the scientific initiation student Jonathan Mendes of Chagas Crosara.

This work was carried out with the support of the Coordination for the Improvement of Higher Education Personnel - Brazil (CAPES) - Financing Code 001.

The studies in Germany carried out in this work were carried out with the support of the Coordination for the Improvement of Higher Education Personnel - Brazil (CAPES) through the PROBRAL project - 88887.143947 / 2017-00 (Migrado - SICAPES3) - *Thermomechanical processing of emerging metallic materials*.

"Humility is the first step towards wisdom."

Saint Thomas Aquinas

ABSTRACT

The A297 cast austenitic stainless steels have good mechanical properties for high temperature and moderate pressure applications. The common applications of these steels include ovens for cracking oil, steel and power plants where good mechanical and oxidation resistance are required. A recurring problem in the utilization of these materials is the loss of strength after prolongued heating due to the formation of precipitates at grain boundaries. The development of new alloys less susceptible to embrittlement, at a lower cost and with greater dimensional stability is required by users to decrease maintenance costs and improve productivity. In the present work, an A297 Gr. HH austenitic stainless steel modified with niobium additions was studied, with the objective of exploring the relationship between the microstructure and the chemical composition and seeking to understand the influence on high temperature oxidation resistance. It is known that niobium refines microstrucutre and can be used to promote the precipitation of carbides, as well as to increase the mechanical strength of these alloys. The studied material was evaluated in terms of microstructure (SEM-EDX/EBSD and XRD) and oxidation behavior at 900°C. The oxide layers were characterized in terms of phase composition, residual stresses and the overall oxidation behavior was assessed by mass gain measurements. The material performance was verified through the combination of these properties and mainly by understanding the material microstructural evolution in use caused by the addition of niobium as well as the role of this element in the oxidation resistance. It was found that the addition of niobium indirectly improved the oxidation resistance increasing oxide layer stability against spalling due to lower residual stresses presented due to the niobium addition and the precipitation that occurred in the material reducing its thermal expansion coefficient.

Keywords: Microstructural evolution. Heat-resistant cast austenitic stainless steels. Niobium. Residual stresses. High temperature oxidation resistance.

RESUMO

Os aços inoxidáveis austeníticos fundidos A297 têm boas propriedades mecânicas para aplicações de alta temperatura e pressão moderada. As aplicações comuns desses aços incluem fornos para craqueamento de óleo, usinas siderúrgicas e de energia, onde uma boa resistência mecânica e à oxidação são necessárias. Um problema recorrente na utilização desses materiais é a perda de resistência após aquecimento prolongado devido à formação de precipitados nos contornos dos grãos. O desenvolvimento de novas ligas menos suscetíveis à fragilização, com menor custo e maior estabilidade dimensional é exigido dos usuários para diminuir os custos de manutenção e melhorar a produtividade. No presente trabalho, um aço A297 Gr. inoxidável austenítico HH modificado com adições de nióbio foi estudado, com o objetivo de explorar a relação entre a microestrutura e a composição química e buscar compreender a influência na resistência à oxidação em altas temperaturas. Sabe-se que o nióbio refina a microestrutura e pode ser usado para promover a precipitação de carbonetos, bem como para aumentar a resistência mecânica dessas ligas. O material estudado foi avaliado em termos de microestrutura (MEV-EDS / EBSD e DRX) e quanto ao seu comportamento na oxidação a 900 °C. As camadas de óxido foram caracterizadas em termos de composição de fase, tensões residuais e o comportamento geral de oxidação foi avaliado por medições de ganho de massa. O desempenho do material foi verificado através da combinação dessas propriedades e principalmente pelo entendimento da evolução microestrutural do material em uso causada pela adição de nióbio, bem como o papel deste elemento na resistência à oxidação. Verificou-se que a adição de nióbio melhorou a resistência à oxidação indiretamente aumentando a estabilidade da camada de óxido contra o desplacamento devido as menores tensões residuais apresentadas devido à adição de nióbio e a precipitação que ocorreu no material reduzindo seu coeficiente de expansão térmica.

Palavras-chave: Evolução microestrutural. Aços inoxidáveis austeníticos fundidos resistentes ao calor. Nióbio. Tensão residual. Resistência à oxidação em altas temperaturas.

LIST OF FIGURES

LIST OF TABLES

LIST OF ABBREVIATIONS AND ACRONYMS

A297	ASTM A-297 standard
ASM	American Society of Materials
ASTM	American Society for Testing and Materials
°C	Degrees celsius
Cr_7C_3	Primary chromium carbide
CTE	Coefficient Thermal Expansion
D(α)	Grazing incidence penetration depth
Dx(T)	Length variantion as a function of temperature
Gr.HH	HH steel grade
Gr.HK	HK steel grade
Gr.HP	HP steel grade
Hkl	Miller indexes
K	Degrees kelvin
MPa	Mega Pascal
M_7C_3	Primary chromium carbide
$M_{23}C_6$	Secondary chromium carbide
NbC	Niobium carbide
$Ni_{16}Nb_6Si_7$	G phase primary stoichiometry
$Nb_3Ni_2Si_8$	G phase secondary stoichiometry
OPS	Oxide polishing suspension
PB	Primary beam on grazing incidence diffraction method
PBR	Pilling-Bedworth ratio
PUC	Pontifical Catholic University
SB	Secondary beam on grazing incidence diffraction method
SEM – EBSD	Scanning Electron Microscope - Electron Backscatter Diffraction
SEM	Scanning Electron Microscope
SiO_2	Silicon Oxide
TiN	Titanium nitride
T_f	Melting temperature

UdS	Saarland University
XRD	X-rays diffraction
$\varepsilon_{\alpha\psi}$	Experimentally determined lattice parameter
α	Difference between the diffraction angle and the angle of incidence
Ψ	Angle between the sample surface and the normal diffraction plane

SUMMARY

1 INTRODUCTION

1.1 Brief Review

The development of new materials for numerous applications is a point of significant interest in modern engineering. For the development of these products, the characterization of the materials is an extremely important activity not only to validate the behavior of a given material, but also in order to gain more insight into how the characteristics and properties of these materials act in their final applications.

Austenitic stainless steels are frequently used for applications at high temperatures and in critical working conditions close to their mechanical resistance limits such as pressure and tension. It is frequently necessary to develop metal alloys that withstand severe application conditions, with lower costs and higher efficiency is frequent, and it is not different with ASTM A297 cast stainless steels (Fe-Ni-Cr-C alloys), which is commonly used for these applications and studied in this work with some modifications in its chemical composition, is no exception. Therefore, further complementary tests about the result of the alloy elements addition and their influences on the microstructure and stainless steels oxidation phenomena are necessary to optimize the next generation of materials.

Austenitic stainless steels are known for their elevated high temperature oxidation resistance and mechanical strength. They are used as a structural part of ovens for cracking hydrocarbons and equipment that work at high temperatures in the steel industries (ABBASI *et al*., 2019). One of the alternatives investigated to achieve this goal is the introduction of niobium in steel, which promotes the formation of carbides and may improve the mechanical strength. In addition to the operational conditions, it is possible to note other influencing factors that can limit materials resistance and durability such as its geometry, loading mode, adherence of the oxide layers and the presence of discontinuities or cracks along its structure.

This material is used at high temperatures due to its increase in creep resistance and also by the precipitation of carbides, due to the addition of some specific elements such as niobium (ABBASI *et al.*, 2019; MADERN *et al.*, 2018). Therefore, the main chemical modifications carried out in this study, such as the

increase in carbon content and the addition of niobium, aim to guarantee high mechanical resistance due to carbide precipitation.

The problem is that both the mechanical resistance, and the high temperature oxidation resistance of these materials must be taken into account to guarantee the integrity of the structures in which they are used by creating a more resistant chromia-based passive layer. The addition of niobium alters the microstructure of the material, modifies the composition of the carbides, the contents of chromium in matrix solution; therefore, influence of such changes on the oxidation resistance must therefore be studied for these materials.

This study entailed the use of microstructural characterization, high temperatures oxidation tests and oxide layers analysis correlating the results with the final properties obtained in the oxidized layer of the material in order to understand the behavior and improve the use of A297 heat-resistant austenitic stainless steel HH with niobium in its applications.

Brazil leads in niobium production worldwide, in addition to possessing the majority of the reserves of this mineral, so steels with the addition of this element are also of great economic significance and technological importance for the country. The effect of niobium addition in this specific alloy (Gr.HH) and the relationship of these additions to the increase in mechanical strength, high temperatures oxidation resistance, as well as the formation of residual stresses in the oxidized layer were evaluated in this work.

The degree of technological innovation and the aim of this work was linked to the possibility of obtaining a stable alloy, with niobium additions, from the microstructural part as well as to the oxidation process, being ideal for applications with high loads at high temperatures.

Past studies for the development of austenitic stainless steels have focused on increasing the mechanical strength and creep resistance of these materials through the precipitation of new phases. Niobium provides carbides precipitation as well as thermal stability for this steel. Few studies have addressed the issue of oxidation of this type of material with niobium additions. This project studied precipitation of niobium carbides, oxidation resistance and the residual stresses evolution in the oxide layer of a cast austenitic stainless steel ASTM A297 Gr. HH Nb-alloyed modified, at high temperatures.

1.2 Objectives

The study of ASTM A297 Gr. HH modified steel is very important due to its application in many places as described above. Thus, the main objectives were as follows:

a) To characterize the metallic substrate and oxide layer of materials with and without niobium in conditions such as cast and aged, with exposure to high temperatures in an atmospheric environment;
b) To examine the thermal stability of carbides as a function of temperature and different niobium additions, as well as the stable phases at high temperatures through thermodynamic simulations (Matcalc®) and microscopy tests;
c) To measure the mass variation and identify the oxidation mechanisms of materials exposed to high temperatures in an atmospheric environment, as well as the role of the passive protective layer and the evolution of the observed oxides;
d) To evaluate the oxide layer stability and the residual stresses generation at high temperatures after the different oxidation conditions (cyclic/isotherm) demonstrating the role of niobium in this process.

1.3 Thesis structure and organization

This thesis consists of 6 chapters. Chapter 1 is an introduction to the scope of the research which has been undertaken.

Chapter 2 provides a literature review with some important works using similar materials.

Chapter 3 presents the microstructure and cyclic oxidation behavior of modified Nb-alloyed A297 HH refractory austenitic stainless steel. The thermodynamical simulations as equilibrium diagrams, carbon and chromium partitioning as well as solidification process of the metallic substrate were explored in this chapter.

Chapter 4 presents the oxide layer evolution of cast Fe24Cr12NiXNb heat-resistant cast steels at 900°c in atmospheric air. A detailed oxide layer characterization was done in this chapter.

Chapter 5 presents the residual stress analysis in thermally grown oxide scales developed on Nb-alloyed refractory austenitic stainless steels and the relation with the substrate thermal expansion analysis. EBSD (Electron backscatter diffraction) analyses were done in order to validade Sin^2Psi method due to non-texturized multilayer oxide scale.

The chapters 3, 4 and 5 referring to the results obtained in this thesis were written in article format and the format followed the guidelines of each journal in which they were published in.

Chapter 6 brings the final considerations of the thesis, including the main conclusions, suggestions for future works, and original contributions.

2 LITERATURE REVIEW

2.1 Heat-resistant cast austenitic stainless steels

Stainless steels are well-known materials for the high chromium content responsible for creating the passive surface layer that makes them more resistant to the corrosive effects of the medium than other materials, in addition to their high mechanical strengths at elevated temperatures (CASTRO, 2012). According to ASM (American Society of Materials), the most prominent grades for cast stainless steel are classes C, for application in aqueous corrosive environments (up to 650 ºC) and class H, object of study of this work, for applications in high temperatures (above 650 ºC) (NUNES, 2005). Among the various applications of these materials, the most common, for type H steels, are steel equipment (Figures 01 and 02), gas turbines, equipment for power generation and petrochemical processing equipment.

Figure 1 - A297 stainless steel oven base tray

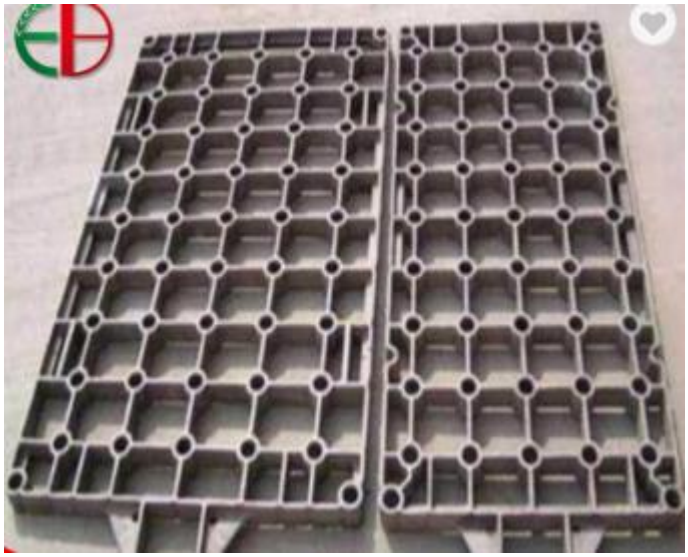

Source: Eternal Bliss Casting.com

Figure 2 – Stainless steel structure for cracking ovens

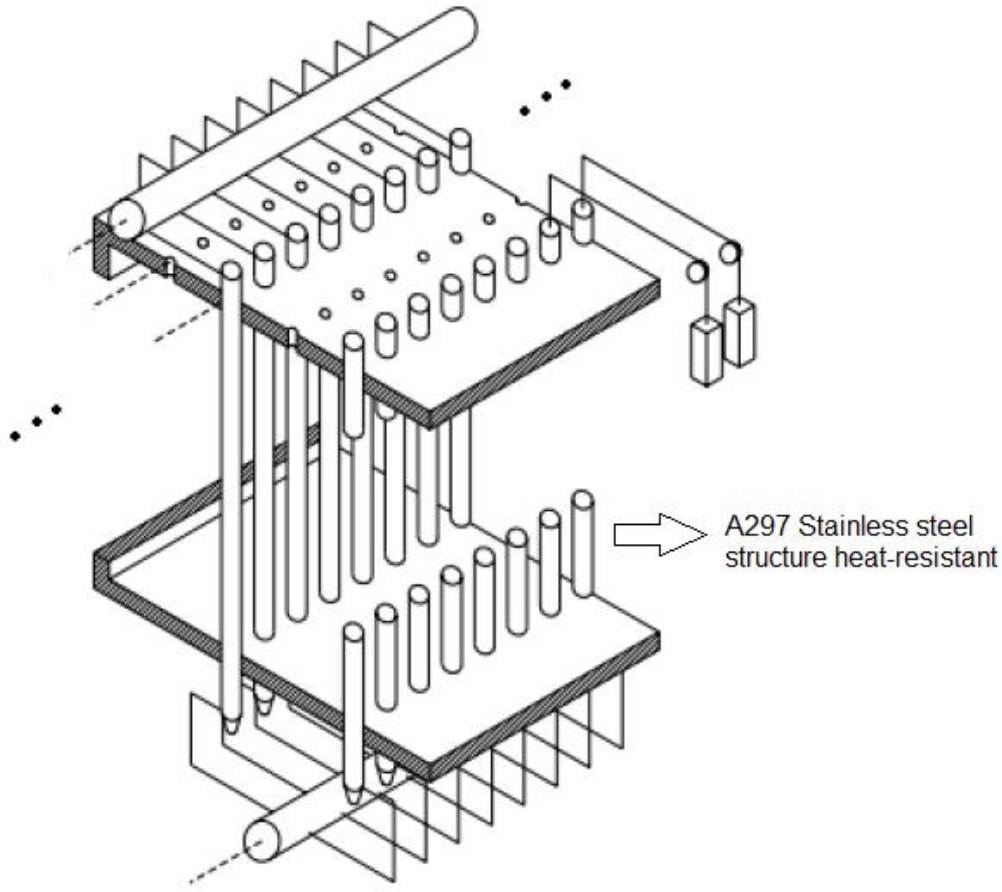

Source: Modified of Fernandes, K. C. *et al.*, 2013

High-temperature resistant steels include HH, HK and HP, which are used in applications up to 1150 ºC, with good oxidation resistance and frequently found in the steel market. HP steels are one of the most used grades of cast austenitic steels, and can be modified with niobium and other alloying elements in order to provide greater mechanical performance and superior characteristics during thermomechanical requests.

The chemical composition and average mechanical properties of different A297 steel grades are presented in Tables 1 and 2, respectively.

Table 1 - Chemical composition ranges (%wt) of HH, HK and HP grades

Chemical elements	HH	HK	HP
C	0.2-0.5	0.2-0.6	0.35-0.75
Si	2	2	2.5
Cr	24-28	24-28	24-28
Ni	11-14	18-22	33-37

Source: ASTM A297, 2017

The Table 02 shows some mechanical properties between HH, HK and HP steels.

Table 2 - Mechanical properties of HH, HK and HP grades

Parameter	HH	HK	HP
Tensile Strength (MPa)[a]	515	450	430
Yield Strength (MPa)[a]	240	240	235
Elongation (%)[b]	10	10	4.5

Source: ASTM A297, 2017

[a]: Minimum limits

[b]: Stretching obtained with testing on a 50 mm (2”) specimen

Stainless steels are classified into groups such as austenitic, ferritic, martensitic, duplex and precipitation hardenable. The correct manipulation of the chemical composition allows different microstructures to be obtained. The microstructure is mainly affected by the levels of chromium and nickel equivalent, which are stabilizing elements of ferrite and austenite respectively (ARAUJO, 2015; PAUPLER, 1988).

The difference of A297 HH steel to the others is its nickel content, which is between 11 and 14% (the lowest among the others mentioned in this study) as shown in Table 01. Beyond microstructural changes proved by nickel addition, it also improves the oxidation resistance of the alloy. As the addition of this element has a very high cost, there is a tendency to use the HH grade in industry and steel mills, due to its relatively lower cost compared to the others.

The growing demand for higher productivity led to the demand for better mechanical performance in cast austenitic stainless steels and the microstructural modification with different amounts of niobium began to be evaluated and studied for this purpose. (BARBABELA *et al.*, 1991).

The roles of each chemical element, although well understood individually, need to be investigated in a situation where they are together and exposured to the work environments characteristic of these materials.

The difference between the A297 steel grades is in their chemical compositions that reflect on different microstructures formation and make them have different mechanical properties and oxidation resistance.

The formation of carbides is the key point in the study of the microstructure of these materials. Stainless steels for high temperature applications have a considerable carbon content responsible for a microstructural evolution during hot work, with the appearance of carbides, according to the service temperature, maintaining high mechanical resistance mainly with respect to creep (NUNES *et al.*, 2007). Because of the importance of precipitation phenomena regarding mechanical strength of these alloys, a number of studies have been conducted to investigate the issue. For instance, there are finite element simulation based on diffusive theories, free energy, nucleation and precipitate evolution theories that can be used to study these materials in order to relate the computed predicted precipitates to microstructural evolution during their practical use (ABBASI *et al.*, 2019; SHIM *et al.*, 2010).

A297 standard steels have an austenitic matrix with high amounts of carbides due to their carbon and chromium content. Microstructural modifications such as increasing the carbon content and including niobium have been researched and may cause a replacement of part of the potential chromium carbides for niobium carbides that promote the refinement of the microstructure and the finer precipitation at high temperatures, generating increased mechanical strength due to secondary chromium carbides precipitation that were also studied in this work (BUCHANAN; KRAL, 2012; NUNES *et al.*, 2007) (BARBABELA *et al.*, 1991; NUNES *et al.*, 2007; SPEER *et al.*, 2017).

The presence of NbC improves structural and thermal stability because these carbides form/dissolve at higher temperatures than chromium carbides, contributing to the restriction of movement of materials volumetric defects, sliding of grain

boundaries and by generating anchor points for nucleation of new phases that will form during cooling (COX, 1978; SHINODA *et al.*, 1978; WEN-TAI; HONEYCOMBE, 1985).

When adding niobium, and therefore favoring the formation of NbC, there is a fragmentation of the primary chromium carbides that are present in the material. The amount of precipitation, microstructure refinement and M_7C_3 (Cr_7C_3) chromium carbide fragmentation is a function of the niobium content present in the alloy (DE ALMEIDA SOARES *et al.*, 1992). Niobium has a potential to be explored due to its greater interaction with carbon when compared to other elements, such as chromium for example, replacing these elements in the formation of carbides, in addition to its higher solidification temperature during processing and stainless steel casting (BARBABELA *et al.*, 1991; SPEER *et al.*, 2017).

With the addition of niobium, there is an increase in the ratio between niobium carbides and chromium carbides (phases present in the material), due to this strong reactivity of niobium with carbon (BARBABELA *et al.*, 1991). According to (SHI; LIPPOLD, 2008), the ratio between niobium and chromium will determine which carbides will be precipitated. A greater ratio leads to a higher probability of NbC formation during solidification.

The experiments made on cast HP austenitic stainless steel by Barbela (1991), for example, they revealed the presence of chromium carbides of the M_7C_3 type in alloys with 0.69%Nb and 1.23%Nb, but only $M_{23}C_6$ carbides in alloys with 1.97%Nb due to the lower carbon availability for primary chromium carbides formation. Therefore, if the concentration of niobium is high enough, it can occur, almost in its totality, only secondary carbides formation of the type $M_{23}C_6$ (DE ALMEIDA SOARES *et al.*, 1992). According to (BARBABELA *et al.*, 1991) chromium and niobium carbides precipitate in interdendritic regions in the austenitic stainless steel.

For high-strength steels, the niobium addition can provide performance improvements in innovative products, such as quenched steels or that have mechanical strength gain induced by plastic deformation (SPEER *et al.*, 2017). However, at high temperatures, niobium carbide can be converted into G phase ($Ni_{16}Nb_6Si_7$), a fragile deleterious phase, whose interface with the matrix can be a preferred site for crack nucleation. (BARBABELA *et al.*, 1991).

Researches are found in the literature correlating the addition of niobium and even other elements such as yttrium or titanium to the change of the basic mechanical properties and mainly the carbides morphology formed in the “as cast” and aged condition (NUNES *et al.*, 2007). The focus is on the microstructural evolution of carbides, on embrittlement by the G phase formation (interdendritic high hardness phase composed of niquel, silicon and niobium, usually with $Ni_{16}Nb_6Si_7$ stoichiometry), chemical compositions and mechanical resistance after aging at high temperatures (BUCHANAN; KRAL, 2012; JAVAHERI *et al.*, 2014).

A297 Gr. HH austenitic stainless steels are used in high temperatures and under high mechanical loads. As these steels have a high carbon content and different alloying elements such as chromium, niobium, manganese, among others, it is expected that during heating and hot working, the diffusion process will be favored in such a way that significant microstructural modifications are possible. In general, for the A297 alloys, the carbon partition during solidification will determine the phases present in the material. As more alloying elements are added, that react strongly with carbon such as niobium for example, a smaller carbon amount will be distributed for the precipitation of chromium carbides in the austenitic matrix. According to (SHI; LIPPOLD, 2008) the microstructural evolution is result of the alloy chemical composition and the thermodynamic conditions that promote the diffusion and the appearance of new phases.

According to some authors, depending on the alloy composition, NbC is not stable at the working temperature (815 - 850°C) decomposing to form the deleterious G phase $Ni_{16}Nb_6Si_7$ (CHEN; THOMAS; KNOWLES, 2004; ECOB; LOBB; KOHLER, 1987; PIEKARSKI, 2001; POWELL; PILKINGTON; MILLER, 1988) or $Nb_3Ni_2Si_8$ (SHINOZAKI *et al.*, 1999). Above 1100°C NbC is stable again, dissolving only at even higher temperatures close to 1345 ° C, depending on alloy composition (DE ALMEIDA SOARES *et al.*, 1992). During cooling, the NbC solidification occurs at high temperatures and then the remaining free carbon joins the chromium to form the primary chromium carbides at slightly lower temperatures.

According to (DE ALMEIDA; RIBEIRO; LE MAY, 2002), it is common to observe the formation of secondary chromium carbides ($M_{23}C_6$), in heat-resistant cast austenitic stainless steels during aging at high temperatures, which are the result of the connection of the few carbon that was expelled from the NbC and the high chromium available in the austenitic matrix, these carbides arise from a

favorable thermodynamic condition. The work done by (GONG; TU; YOON, 1999) showed that after a partial NbC dissolution and carbon release at temperatures around 800°C, $M_{23}C_6$ is therefore formed. After a long-term exposure to a temperature of approximately 850°C, the condition is known as completely aged (NISHIMOTO *et al.*, 2001), where the carbides are already in a different from the one known in the “as cast” condition.

Just as carbon undergoes its partition between phases, depending on the niobium content during the solidification or cooling process, the same occurs with the chromium partition. The thermodynamic processes that govern these diffusions are already well known in materials science and engineering and have been developed again in the works of (SHIKANAI; MITAO; ENDO, 2008; SPEER *et al.*, 2003), as well as the relation between carbon, niobium and chromium was developed by (BARBABELA *et al.*, 1991) for HP steels.

It is known that there is a thermodynamic movement and a stronger tendency for carbon to join niobium and culminate in the NbC-type carbides precipitation, in addition to decrease the chromium carbides fraction precipitated by the absence of the amount of carbon that was previously present (BARBABELA *et al.*, 1991). Therefore, it is expected that there is a chromium partition that would initially precipitate in the form of carbides, primary or secondary, going to the austenitic matrix. Chromium enrichment of the austenitic matrix can be expected to be an important factor to increase high temperature oxidation resistance through the supplementation of chromium to maintain the passive oxide layer. (BIRKS; MEIER; PETTIT, 2006). Thus, new efforts should be undertaken to understand more deeply the effect of niobium as an alloying element in different conditions, in order to optimize the performance of this new generation of modified steels. (SPEER *et al.*, 2017).

2.2 Oxidation behavior of Fe-Cr-Ni alloys

Oxidation resistance is a property of a material to withstand degradation when subjected to corrosive environments, normally under high temperatures, through the generation of oxides. The material is protected by the formation of these oxide layers that will prevent oxidation from penetrate into the material and these layers act as a protective film for the metallic substrate (TOLPYGO; CLARKE, 1999).

During the process of exposing alloys to high temperatures, an oxide layer is generated, resulting from the union of oxygen atoms with metal atoms of the substrate. Considering Wagner's theory and the diffusive movements in the layers growth, chromium and silicon oxides can be considered as protective layers and are the first to be formed directly in contact with the metallic substrate. Some elements have specific properties to prevent the corrosive process, such as chromium and aluminum. They are able to form an integral and adherent barrier to avoid contact of the substrate with the oxidizing atmosphere. The critical chromium content is a determinant factor for the formation of this protective layer and to prevent the formation of non-protective oxides (eg, iron oxides) (ZHANG *et al.*, 2019).

Silicon also acts as a protective element for the material. Its addition helps in oxidation and carburization resistance and has been studied in contents above 2.5% by weight (BARBABELA *et al.*, 1991; DE ARAÚJO, 2017). After some time at high temperatures, silicon oxide (SiO_2) forms at the oxide/substrate interface due to its greater thermodynamic stability according to the Ellingham diagram, preventing the chromium and other elements diffusion from the metallic substrate for the layer of external oxides (BIRKS; MEIER; PETTIT, 2006).

The generation of this layer is linked to the alloy chemical composition and the supply of ions for its growth. The layer growth model can be explained by Wagner's theory, which is widely accepted and known. This theory demonstrates that the layer growth rate occurs as a function of the ions diffusion that pass through the layer in a substitutional or interstitial way (WAGNER, 1951).

According to (LI *et al.*, 2016), the different phases formed at different temperatures can accelerate or delay the oxidation process depending on its characteristics. Chemical elements maps along the cross-section of the specimen proved to be an interesting resource to reveal the elements responsible for the formation of each specific phase and their arrangement in the multiphase layer. (LI *et*

al., 2012). The oxide layer adherence and its resistance to ions diffusion are key-factors to prolong the useful life of a material exposed to high temperatures oxidation.

To evaluate oxidation resistance some tests can be performed. High temperature oxidation tests can be isothermal or cyclic. The isothermal oxidation tests consist of subjecting the samples to high temperatures during the proposed period without cooling intervals and the cyclic oxidation tests have, within the proposed period and temperature, cooling intervals and new subsequent heating cycles. Mass measurements of the samples after oxidation can be done *ex situ* with an analytical balance or *in situ* as performed by (CHEN *et al.*, 2018) through a thermal analyzer and a photoelectric microbalance.

One of the factors that affects the adhesion and mechanical integrity of oxides formed at elevated temperatures is the state of stresses present in the layer. According to (SALEHI DOOLABI *et al.*, 2017), cyclic oxidation tests show greater layer detachment due to successive incompatible thermal expansions between the substrate and the oxide layer generated in each thermal cycle. Different coefficients of thermal expansion as well as residual stresses are indicated as the cause of this phenomenon. The same phenomenon was observed in other studies such as (BOUCHAUD; BALMAIN; PEDRAZA, 2008) e (TOLPYGO; CLARKE, 2000a).

The material performance at high temperatures depends on its conservation in the corrosive environment, which is observed through factors such as: the chemical stability of the material, the formation and growth rate of passive oxide layers, adherence of these layers to the substrate, magnitude of thermal stresses, which may vary according to the operating conditions and temperature cycles to which the material has been subjected (EVANS, 1995).

It is known that the oxides, due to its lower thermal expansion coefficient (CTE), expand less than the metallic substrate and because this continuous process of expansion and contraction occurring several times, the generation of thermal residual stresses responsible for great damage to the layers is common. (HUNTZ; SCHÜTZE, 1994; RAKOTOVAO *et al.*, 2018; TOLPYGO; CLARKE, 1999) showed in their work that the thermal stresses generated as well as the growth stresses developed during these oxidation tests are the main responsible for damaging the oxide layer and exposing the metallic substrate to the oxidizing atmosphere.

The stresses are present in most cases as being of compression in the oxide layer and tensile stresses in the metallic substrate, which causes its elongation and creep (TOLPYGO; CLARKE, 2000a). In Figure 03 it is possible to observe the process of generating thermal stress due to the cooling cycles as well as creep phenomenon.

Figure 1 – Thermal stress generation in oxide layers according to the creep rate of the metallic substrate

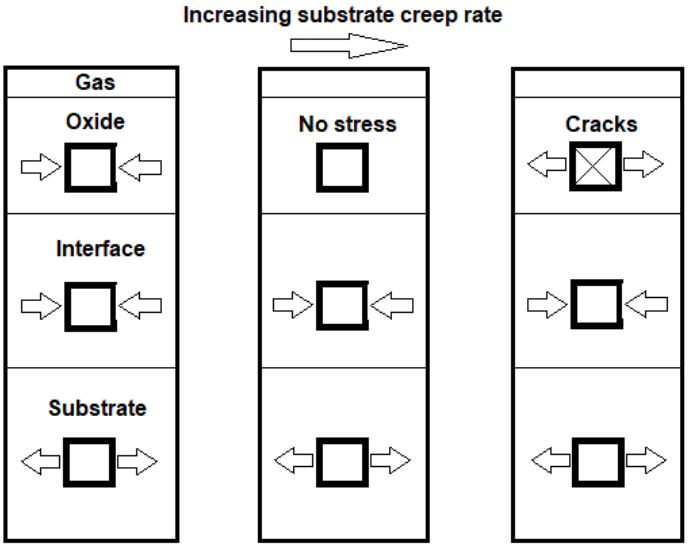

Source: Modified and translated, Evans, H.E (1995), pag. 8

During cooling, but at high temperatures, as the substrate thermal expansion coefficient is bigger than oxide thermal expansion coefficient, substrate shrinks more than oxide and creep occurs. There is an shrinkage of the substrate, followed by creep and the oxide layer is subject to a lower compression stress or even to a tensile stress as the substrate creep rate increases. The compression stress practically disappears in the oxide layer as shown in Figure 03 (TOLPYGO; CLARKE, 2000a).

Another point that contributes significantly to the increase in residual stresses is the volumetric variation due to the phase transformation in metallic substrate (SALEHI DOOLABI *et al.*, 2017).

The adhesion and stability of the oxide layer indirectly ensures that the material plays its role in terms of mechanical strength and structural integrity. Detachment generates oxidized chemical elements selective loss that were incorporated in that layer and expose the metallic substrate to the oxidizing atmosphere, which can

cause an accelerated oxidation of the substrate or oxidation between cracks in the layer when they occur (“*breakaway oxidation”*) (BIRKS; MEIER; PETTIT, 2006; CHEN *et al.*, 2018). The layer failure may be related to its removal by chemical agents, or by mechanical action, but it occurs mainly by detachment generated by the thermal stresses gradient after cooling cycles (CHYRKIN *et al.*, 2015) or induced by growth and through geometric factors of the piece as described in the previous sections (BAXTER; NATESAN, 1983).

The Pilling-Bedworth theory explains the origin of growth stresses in flat samples. Although the origins of growth stresses are complex, it is believed that it is greatly affected by the molar volumes of the oxide and the metal, as well as by the compatibility between their crystalline structures. The volume ratio between the oxide and the substrate at the growth interface can be expressed by equation 01. According to Pilling-Bedworth oxides with a volume ratio (oxide/metal) greater than one, develop compressive stresses and less than one, develop tensile stresses (XU; GAO, 2000).

$$PBR = \frac{Oxide\ Volume}{Metal\ Volume} \tag{1}$$

This is a theory that provides the basis for the formation of recent growth models and understanding of oxidation systems based on the oxide molar volume and the substrate. Although the Pilling-Bedworth theory was originally developed for pure metals, it is metal alloys that are often used in conditions that require oxidation resistance.

According to (XU; GAO, 2000), the application of equation 01 in the analysis of oxidation of metal alloys, can lead to large discrepancies due to the content of a specific element that has been oxidized. Therefore, (XU; GAO, 2000) proposed a new equation that better portrays this metal alloys oxidation and that can be described in equation 02 below:

$$PBR(alloys) = \frac{One\ mol\ volume\ of\ A_xO_x}{X\ mols\ volume\ of\ A\ in\ the\ alloy} \tag{2}$$

Another point of influence on stresses is the oxide growth manner. The generated oxide will normally appear in the direction in which there is lower stresses, and if the oxide grows in a region with restriction, for example in a geometrically curved region, it will develop greater stresses that are related to this geometric factor.

According to diffusional theory of (WAGNER, 1951), high stresses can be generated when an oxide structure does not support oxygen atoms. Lower stresses are generated when the metal structure has small volumetric deffects that adjust and absorb the deformation generated by the inclusion of oxygen atoms.

2.3 Oxide layer residual stresses measurements by XRD diffraction

X-ray diffraction tests measure the stresses generated at high temperatures oxidation. Currently, it is possible to analyze them at room temperature (residual stress), or during their growth on a metallic substrate through *in situ* tests, differentiating the growth stresses and the thermal stresses resulting from cooling.

Over time and technological advances, the X-ray diffraction tests (XRD) has become a widely used tool in the oxide layers stress analysis. This method is based on comparing the interplanar distance of a tensioned phase with its interplanar distance in the standard condition without stress/deformation, using Bragg's law. In addition to identify the present phases in crystalline structures, the XRD can capture changes of 0.5% in interplanar distance, which generates a resolution limit for residual deformations close to 5×10^{-4}. In order to determine the stresses magnitude, it is necessary to know the modulus of elasticity and the poisson's ratio of the analyzed phase.

It is worth mentioning that it is hard to separate the growth stresses from the thermal stresses and phase changes, since the test is performed after the cooling process and provides unified information. However, some studies show the possibility of performing the analysis *in situ* and with Syncrotron light, which is a high-intensity X-ray beam, providing information that allows to identify the cause and the moment of the stress appearance during the layer growth (RAKOTOVAO *et al.*, 2018).

The traditional method of analyzing residual stresses by X-ray diffraction captures the displacement of diffraction peaks, which are associated with the interplanar distance, on the 2Ɵ scale for different “psi” angles (sample inclination angles). In this case, a specific diffraction plane is chosen, which showed good signal quality and peak formation in the diffractogram, and the interplanar distance is measured using Bragg's geometric law. The inclination angles are varied and the greater the 2Ɵ scanning angle in which the peak is located, the greater the sensitivity to deformations present in the crystalline structure due to the size of the lattice parameter of that phase in that plane, this techinique facilitates the visualization and measurement of stresses (GENZEL, 2005).

It is possible to see in Figure 04, the diffractometer rotation angles and their schematic shape, in addition to the reference axes of the sample (S) and of the laboratory (L) for residual stress analysis:

Figure 2 – Diffractometer angles and planes of rotation

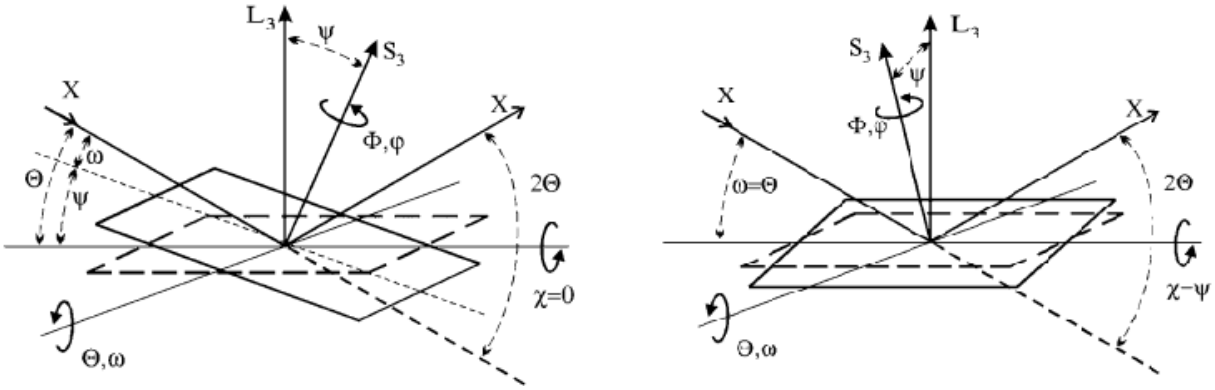

Source: (WELZEL *et al.*, 2005)

After that, the residual deformation is plotted as a function of the inclination at which that measurement was made. Thus, a bi-axial stress model converts this deformation into stress based on the mechanical constants. For highly textured or single-crystal films, Bragg's analysis geometry displays only a few specific diffraction planes (hkl). The volume diffracted by the Bragg geometry is proportional to the thickness of the film, depending on the angle of incidence and the wavelength used. Due to the high penetration depth during this analysis, information from the substrate can be acquired, which is often undesirable for thin film studies. Instead of that, at high scanning angles the peaks are very weak and out of shape, difficult to be observed due to the small volume analyzed by x-ray, and consequently, it is also hard to properly identify the stress level (MA; HUANG; CHEN, 2002).

According to (MA; HUANG; CHEN, 2002) a new approach called grazing incidence geometry has been proposed, producing peaks of greater intensity that facilitate the residual stresses measurement in thin and textured films, since the penetration depth is controllable when compared to the traditional method. Thus, the method is convenient for the evaluation of residual stresses in these situations in which the assessed volume of the sample will contain more information about the (desired) surface than on the (undesired) substrate, for example.

It is possible to see in Figure 05, the angles and the schema of the X-ray diffraction method with grazing incidence for residual stresses analysis in thin films:

Figure 3 – Incidence and diffracted beams with respect to the sample surfasse

Source: (GENZEL, 2005) modificado

In this image the incident beam is called “PB” (primary beam) and the diffracted beam “SB” (secondary beam), the angles α and β are the angles of incidence and diffraction formed with the sample surface. The represented distance D(α) is the penetration depth, which can be easily controlled and has an approximately constant value, in this mode with grazing incidence, over the entire sweep length of the test.

Using grazing incidence, the residual stress values are determined by a linear regression that relates the deformation in the lattice parameter with the term $\cos^2\alpha\sin^2\psi$, following the form of equation (3):

$$\varepsilon_{\alpha\psi} = \tfrac{1}{2}S_2\sigma\cos^2\alpha\sin^2\psi + \tfrac{1}{2}S_2\sigma\sin^2\psi - S_1\sigma \qquad (3)$$

where $\varepsilon_{\alpha\psi}$ is the experimentally determined lattice parameter, α is the difference between the diffraction angle and the angle of incidence, ψ is the angle between the sample surface and the normal diffraction plane.

According to (MA; HUANG; CHEN, 2002) this method presented a good result in comparison to the traditional Bragg method. By changing the incidence angle, it is possible to correlate the residual deformation x depth, generating after apply specifics equations a stress profile or stress gradient according to the thickness of the substrate.

This method produces peaks of greater intensity, its application in some materials is of great importance, as the most common problems are that the diffraction intensity is very low due to the small volume diffracted in conventional methods,

when applied to thin films because just few peaks are revealed due to the crystallographic texture of the material.

An example of using this method is with TiN film, which is used in several applications from microelectronics to tool coatings, and the crystallographic texture (grain orientation) alters the mechanical properties of this film considerably (CHOU; YU; HUANG, 2002).

The crystallographic texture of this film can be discovered through an X-ray diffraction test where the intensity of the peaks reveals the intensity of the orientation of the grains (texture). The approach known as “grazing incidence” increased the diffraction volume of thin films, helping to identify the peaks and the residual stress attributed to that phase (HUANG; MA; CHEN, 2006).

REFERENCES

ABBASI, M. *et al.* G-phase formation in twenty-years aged heat-resistant cast austenitic steel reformer tube. **Materials Characterization**, v. 148, p. 297–306, 2019.

ARAUJO, M. V. P. DE. **Estudo do comportamento em fadiga do aço ASTM A297 Gr HP modificado com nióbio em altas temperaturas**. [s.l.] Universidade de São Paulo, 2015.

BARBABELA, G. D. *et al.* Role of Nb in modifying the microstructure of heat-resistant cast HP steel. **Materials Characterization**, v. 26, n. 3, p. 193–197, 1991.

BAXTER, D. J.; NATESAN, K. MECHANICAL CONSIDERATIONS IN THE DEGRADATION OF STRUCTURAL MATERIALS IN AGGRESSIVE ENVIRONMENTS AT HIGH TEMPERATURES. **Reviews on high temperature materials**, v. 5, n. 3–4, p. 149–250, 1983.

BIRKS, N.; MEIER, G. H.; PETTIT, F. S. **Introduction to the high temperature oxidation of metals, Second edition**. [s.l: s.n.].

BOUCHAUD, B.; BALMAIN, J.; PEDRAZA, F. Cyclic and isothermal oxidation at 1,100 °c of a CVD aluminised directionally solidified Ni superalloy. **Oxidation of Metals**, v. 69, n. 3–4, p. 193–210, 2008.

BUCHANAN, K. G.; KRAL, M. V. Crystallography and morphology of niobium carbide in as-cast HP-niobium reformer tubes. **Metallurgical and Materials Transactions A: Physical Metallurgy and Materials Science**, v. 43, n. 6, p. 1760–1769, 2012.

CASTRO, D. B. V. DE. **Estudo do comportamento em fadiga do aço ASTM A297 Gr HP modificado com nióbio em altas temperaturas**. [s.l.] Universidade de São Paulo, 2012.

CHEN, H. *et al.* Oxidation behavior of Fe-20Cr-25Ni-Nb austenitic stainless steel in high-temperature environment with small amount of water vapor. **Corrosion Science**, v. 145, p. 90–99, 2018.

CHEN, Q. Z.; THOMAS, C. W.; KNOWLES, D. M. Characterisation of 20Cr32Ni1Nb alloys in as-cast and Ex-Service condition by SEM, TEM and EDX. **Materials Science and Engineering A**, v. 374, n. 1–2, p. 398–408, 2004.

CHOU, W. J.; YU, G. P.; HUANG, J. H. Mechanical properties of TiN thin film coatings on 304 stainless steel substrates. **Surface and Coatings Technology**, v. 149, n. 1, p. 7–13, 2002.

CHYRKIN, A. *et al.* Effect of thermal cycling on protective properties of alumina scale grown on thin Haynes 214 foil. **Corrosion Science**, v. 98, p. 688–698, 2015.

COX, G. J. RE-EXAMINATION OF COMPOSITIONAL EFFECTS IN CAST, AUSTENITIC HEAT-RESISTING STEELS WITH PARTICULAR REFERENCE TO THE USE OF NIOBIUM. **Br Foundryman**, v. 71, n. 12, p. 263–278, 1978.

DE ALMEIDA, L. H.; RIBEIRO, A. F.; LE MAY, I. Microstructural characterization of modified 25Cr-35Ni centrifugally cast steel furnace tubes. **Materials Characterization**, v. 49, n. 3, p. 219–229, 2002.

DE ALMEIDA SOARES, G. D. *et al.* Niobium additions in HP heat-resistant cast stainless steels. **Materials Characterization**, v. 29, p. 387–396, 1992.

ECOB, R. C.; LOBB, R. C.; KOHLER, V. L. The formation of G-phase in 20/25 Nb stainless steel AGR fuel cladding alloy and its effect on creep properties. **Journal of Materials Science**, v. 22, n. 8, p. 2867–2880, 1987.

EVANS, H. E. Stress effects in high temperature oxidation of metals. **International Materials Reviews**, v. 40, n. 1, p. 1–40, 1995.

GENZEL, C. **X-ray residual stress analysis in thin films under grazing incidence - Basic aspects and applications**. Materials Science and Technology. **Anais**...2005

GONG, J. M.; TU, S. T.; YOON, K. B. Damage assessment and maintenance strategy ofhydrogen reformer furnace tubes. **Engineering Failure Analysis**, v. 6, n. 3, p. 143–153, 1999.

HUANG, J. H.; MA, C. H.; CHEN, H. Effect of Ti interlayer on the residual stress and texture development of TiN thin films. **Surface and Coatings Technology**, v. 200, n. 20–21, p. 5937–5945, 2006.

HUNTZ, A. M.; SCHÜTZE, M. Stresses generated during oxidation sequences and high temperature fracture. **Materials at High Temperatures**, v. 12, n. 2–3, p. 151–161, 1994.

JAVAHERI, V. *et al.* The effect of Nb and Ti on structure and mechanical properties of 12Ni-25Cr-0.4C austenitic heat-resistant steel after aging at 900 °c for 1000 h. **Journal of Materials Engineering and Performance**, v. 23, n. 10, p. 3558–3566, 2014.

LI, D. SHENG *et al.* High-Temperature Oxidation Resistance of Austenitic Stainless Steel Cr18Ni11Cu3Al3MnNb. **Journal of Iron and Steel Research International**, v. 19, n. 5, p. 74–78, 2012.

LI, H. *et al.* A new insight into high-temperature oxidation mechanism of super-austenitic stainless steel S32654 in air. **Journal of Alloys and Compounds**, v. 686, p. 326–338, 2016.

MA, C. H.; HUANG, J. H.; CHEN, H. Residual stress measurement in textured thin film by grazing-incidence X-ray diffraction. **Thin Solid Films**, v. 418, n. 2, p. 73–78, 2002.

MADERN, N. *et al.* Characterization of refractory steel oxidation at high temperature. **Corrosion Science**, v. 132, p. 223–233, 2018.

NISHIMOTO, K. *et al.* Changes in microstructure of HP-modified, heat-resisting cast alloys under long-term aging. Repair weld cracking of service-exposed, HP-modified, heat-resisting cast alloys (2nd report). **Welding International**, 2001.

NUNES, F. C. **alteração da microestrutura e das propriedades mecânicas pela adição de ítrio em aços inoxidáveis do tipo-HP modificado fundidos por centrifugação**. [s.l.] Universidade Federal do Rio de Janeiro, 2005.

NUNES, F. C. *et al.* Microstructural changes caused by yttrium addition to NbTi-modified centrifugally cast HP-type stainless steels. **Materials Characterization**, v. 58, n. 2, p. 132–142, 2007.

PAUPLER, P. G. E. Dieter. Mechanical Metallurgy. 3rd ed., Mc Graw-Hill Book Co., New York 1986. XXIII + 751 p., DM 138.50, ISBN 0–07–016893–8. **Crystal Research and Technology**, 1988.

PIEKARSKI, B. Effect of Nb and Ti additions on microstructure, and identification of precipitates in stabilized Ni-Cr cast austenitic steels. **Materials Characterization**, v. 47, n. 3–4, p. 181–186, 2001.

POWELL, D. J.; PILKINGTON, R.; MILLER, D. A. The precipitation characteristics of 20% Cr/25% NiNb stabilised stainless steel. **Acta Metallurgica**, v. 36, n. 3, p. 713–724, 1988.

RAKOTOVAO, F. *et al.* In situ Synchrotron X-Ray diffraction study of high-temperature stress relaxation in chromia scales containing the reactive element yttrium. **Acta Materialia**, v. 159, p. 276–285, 2018.

SALEHI DOOLABI, M. *et al.* Comparison of Isothermal with Cyclic Oxidation Behavior of “Cr-Aluminide” Coating on Inconel 738LC at 900 °C. **Oxidation of Metals**, v. 87, n. 1–2, p. 57–74, 2017.

SHI, S.; LIPPOLD, J. C. Microstructure evolution during service exposure of two cast, heat-resisting stainless steels - HP-Nb modified and 20-32Nb. **Materials Characterization**, v. 59, n. 8, p. 1029–1040, 2008.

SHIKANAI, N.; MITAO, S.; ENDO, S. Recent development in microstructural control technologies through the thermo-mechanical control process (TMCP) with JFE Steel’s high-performance plates. **JFE Technical Report**, n. 11, p. 011–02, 2008.

SHIM, J. H. *et al.* Numerical simulation of long-term precipitate evolution in austenitic heat-resistant steels. **Calphad: Computer Coupling of Phase Diagrams and Thermochemistry**, v. 34, n. 1, p. 105–112, 2010.

SHINODA, T. *et al.* EFFECT OF SINGLE AND COMBINED ADDITIONS OF Ti AND Nb ON THE STRUCTURE AND STRENGTH OF THE CENTRIFUGALLY CAST HK40 STEEL. **Trans Iron Steel Inst Jpn**, v. 18, n. 3, p. 139–148, 1978.

SHINOZAKI, K. *et al.* Deterioration of weldability of long-term aged HP heat-resistant cast steel containing Nb, Mo, and W. **Welding International**, v. 13, n. 1, p. 39–48, 1999.

SPEER, J. *et al.* Carbon partitioning into austenite after martensite transformation. **Acta Materialia**, v. 51, n. 9, p. 2611–2622, 2003.

SPEER, J. G. *et al.* **Nb-microalloying in next-generation flat-rolled steels: An overview**. Materials Science Forum. **Anais**...2017

TOLPYGO, V. K.; CLARKE, D. R. **Alumina scale failure resulting from stress relaxation**. Surface and Coatings Technology. **Anais**...1999

TOLPYGO, V. K.; CLARKE, D. R. Spalling failure of α-alumina films grown by oxidation: I. Dependence on cooling rate and metal thickness. **Materials Science and Engineering A**, v. 278, n. 1–2, p. 142–150, 2000.

WAGNER, C. Atoms Movements. **ASTM**, p. 153–163, 1951.

WELZEL, U. *et al.* **Stress analysis of polycrystalline thin films and surface regions by X-ray diffractionJournal of Applied Crystallography**, 2005.

WEN-TAI, H.; HONEYCOMBE, R. W. K. Structure of centrifugally cast austenitic stainless steels: Part 1 HK 40 as cast and after creep between 750 and 1000°C. **Materials Science and Technology (United Kingdom)**, v. 1, n. 5, p. 385–389, 1985.

XU, C.; GAO, W. Pilling-bedworth ratio for oxidation of alloys. **Materials Research Innovations**, v. 3, n. 4, p. 231–235, 2000.

3 ARTICLE 1 - MICROSTRUCTURE AND CYCLIC OXIDATION BEHAVIOR OF MODIFIED NB-ALLOYED A297 HH REFRACTORY AUSTENITIC STAINLESS STEEL

The chapter 3 refers to the results obtained in this article mentioned in the title of the chapter. It was written in article format and the format followed the guidelines of the journal.

Authors:

Ramos, P. A., Coelho, R.S., Pinto, H.C., Soldera, F., Mücklich, F., Brito, P. P.

Paper published by Materials Chemistry and Physics.

RAMOS, P. A. *et al.* Microstructure and cyclic oxidation behavior of modified Nb-alloyed A297 HH refractory austenitic stainless steel. **Materials Chemistry and Physics**, v. 263, p. 124361, 2021.

Microstructure and cyclic oxidation behavior of modified Nb-alloyed A297 HH refractory austenitic stainless steel

Abstract

The modified ASTM A297 Gr. HH austenitic stainless steels are a group of refractory alloys designed for high temperature applications that required elevated mechanical strength, such as those found in petrochemical furnace structures and in the steel industry. This study examines the overall microstructural features and cyclic oxidation behaviour of modified HH steels with 0.09%Nb and 0.77%Nb additions. The investigations involved thermodynamic simulations and microstructure analyses conducted by optical and scanning electron microscopy of the substrate materials in the as-cast and aged conditions. The cyclic oxidation tests were performed at 900°C in atmospheric conditions with oxidation times up to 960h. The resulting oxide scales were analysed by X-ray diffraction and scanning electron microscopy. The thermodynamic simulations and microstructure analyses of the as-cast steels revealed larger amounts of niobium carbides in the 0.77%Nb steel than in the 0.09%Nb steel, in connection with larger amounts of chromium in solution. Despite this precipitation difference, no significant changes were noticed in the long-term oxidation behaviour of the tested materials.

Key-Words: High temperature oxidation; refractory steel; thermodynamic simulations; niobium; microstructure.

3.1 Introduction

The cast ASTM A297 HH austenitic stainless steels are classified as refractory steels which exhibit elevated oxidation resistance and mechanical strength. They are used as structural parts in hydrocarbon cracking furnaces and in several steel-making industry equipment that experience elevated working temperatures under high loads [1,2]. The ASTM A297 standard specifies several types of H-grade steels that are designated for high temperature applications. The most common grades are HP, HK, HH steels, which exhibit predominantly variations in nickel concentration.

These steels have chromium contents above 20%, which promotes corrosion and carburization resistance due to the formation of a very adherent and stable oxide layer, which protects the material from the corrosive environments [3,4]. The addition of niobium to refractory steels leads to the formation of NbC precipitates instead of chromium carbides and has been reported to enhance creep resistance and mechanical strength at high temperature [5,6]. Cobalt and tungsten additions have also been reported to improve mechanical strength at high temperatures [3,7].

Reliable long-term operation of refractory steels depends on microstructure stability at the high temperature service conditions in which these materials are employed. The work done by [8] showed that at higher aging temperature the ductility is lower because the large secondary chromium carbides precipitation which enhance crack nucleation. As such, a number of investigations have been performed with the objective of understanding the evolution of carbides in these steels and the loss of mechanical strength caused by the formation of brittle interdendritic phases, such as G-phase [1,9–13]. However, considerably less information is available concerning the oxidation resistance of these materials, especially considering the variety of chemical composition modifications that have been introduced in recent years with the objective of enhancing mechanical properties [3,4,14]. Evaluation of the high temperature oxidation is considered interesting for these modified steels, since the presence of niobium may lead to the formation of NbC at the expense of chromium carbides, increasing the amount chromium in solution in the austenitic matrix, which could modify oxidation resistance.

The aim of this study is to analyze the influence of niobium on the microstructure and cyclic oxidation resistance of modified A297 HH austenitic

stainless. Herein resides the main contribution of the present work, since published literature has so far emphasized the influence of niobium on the HP and HK grades, with higher nickel contents, and no similar investigations on the behavior of HH steels were identified. The HH grade was selected because of its competitive price and properties, and the investigations were performed on steels in the as-cast and aged conditions by experimental methods and thermodynamic simulations [10,15–17].

3.2 Experimental procedure

3.2.1 Materials

The materials used in the present study were modified ASTM A297 HH austenitic stainless steels (Fe24Cr12Ni) produced by FULIG® casting company which are currently used in high temperature applications. The modified composition of ASTM A297 HH steels used in the present study is presented in Table 1 and were performed by optical emission spectrometry.

Table 3. 1 – Chemical composition of the materials employed in this study (wt%)

Modified A297 Gr. HH	0.77% Nb	0.09% Nb	Standard limits (max.)
C (modified)	0.73	0.89	0.2-0.5
Si	0.97	1.23	2.00
Mn	0.55	0.50	2.00
P	0.01	0.03	0.04
S	0.00	0.03	0.04
Ni	11.09	12.12	11.0-14.0
Cr	24.79	24.42	24.0-28.0
Mo	0.32	0.12	0.5
Co (modified)	0.28	0.47	-
Nb (modified)	0.77	0.09	-
Ti (modified)	0.10	0.01	-
Fe	60.32	59.74	Balance

3.2.2 Equilibrium thermodynamics simulations

In order to preliminarily assess the influence of the proposed modifications in chemical composition, equilibrium thermodynamic simulations were performed by using the MatCalc engineering® software [16,18,19]. Since the austenitic stainless steels grade analyzed in this work is designed for long term high temperature operation, assumption of equilibrium condition was considered adequate in the present situation [17]. Following the recommendations of previous researchers, the precipitation kinetics models with diffusion database were also considered [2] because they produce reliable results as long as care is taken while assuming certain material parameters that are not easily determined empirically, such as dislocation density, average prior austenite grain size, correct precipitation site, and nucleation rate for specific system.

For the simulations, MatCalc® version 6.03.0033 with Database “mc_fe” alloys 1.2 was employed. Calculations of phase fraction (wt%) *versus* temperature that provided the equilibrium phases in high temperature conditions were performed in order to identify the expected phases in the aged condition and to compare with the semi-quantitative experimental analysis performed by Optical Microscopy (OM) and Scanning Electron Microscopy (SEM). Additional phase boundary analyses of NbC and $M_{23}C_6$ carbides were carried out to assess the influence of niobium on the high temperature stability of these carbides.

Simulation of the solidification process was also performed according to the Scheil model, which considers the same equilibrium regarding carbon content between solid and liquid phases. This simulation was performed in order to verify the first formed phases. The carbon partitioning in the main phases was compared according to the amount of niobium to analyze the carbon distribution and the carbides formation potential with the presence of niobium.

3.2.3 Microstructure characterization

The microstructural study was carried out on as-cast samples and on samples aged for 480h at 900ºC in air. The overall as-cast phase fraction (% volume) was determined by image analysis using ImageJ® software version 1.52a.

In order to preserve and raise the electrical conductivity of the samples for electron microscopy analyses and preserve the oxide layer integrity, copper protective coatings were applied before mounting. The process consisted of applying a 20 nm layer by plasma sputtering with the composition of 8% Au + 20% Pd (%wt) at a pressure of $1x10^{-2}$ mbar, current of 20-25 mA for 5 minutes. After this coverage, 10 µm of copper was electrochemically deposited through the solution of 20g $CuSO_4$ + 100g H2O, with a voltage of 1.5V DC for 12 minutes. The samples were embedded in high-strength conductive resin, grinded and polished up to 1 µm with OPS.

The microstructure and layer cross sections of the materials was characterized by Leica DM6000M optical multifocus microscopy (OM) and in a dual-beam focused ion beam/scanning electron microscopy (FIB/SEM) workstation (FEI Helios NanoLab 600) equipped with Energy Dispersive X-ray spectroscopy (EDX) analyses. The metallographic sample preparation, prior to these analyses, was performed by grinding with SiC paper #80, #180, #320, #600, #1200, #2500 and polishing with 6, 3, 1 and 0.25 µm (OPS) diamond solution without etching.

Phase analyses of the oxide layers were performed by X-ray Diffraction (XRD) using an Empyrean PANalytical diffractometer with radiation source "Co Kα" and 40 KV in a 2θ range from 20° up to 80° in the symmetrical Bragg Brentano geometry combined with the EDX analyzes mentioned above that generated a detailed spatial configuration of the elements that make up the layer.

3.2.4 Cyclic Oxidation

The cyclic oxidation tests were carried out in a furnace with atmospheric air at 900°C with cooling cycles at 1h, 5h, 10h, 24h, 48h, 120h, 240h, 480h, 960h. Cooling time to room temperature was 15 min, before the next heating cycle up to 900°C. The mass gain was determined with an analytical precision balance (0.0001g) at the end of each cycle (after cooling). The test coupons were cubic with 10 x 10 x 10 mm

dimensions and were ground to #600 SiC paper. Prior to oxidation, the surfaces of all samples were thoroughly cleaned with ethanol and completely dried.

3.3 Results and discussion

3.3.1 Thermodynamic analysis

Results of thermodynamic analysis are presented in Figure 1 in the form of phase fraction (wt.%) equilibrium diagrams for the two modified HH steels (0.09 and 0.77%Nb). It is important to consider, as shown in Table 1, that the investigated alloys exhibit differences in other alloying elements, apart from niobium, such as carbon and molybdenum, that can alter carbide content and composition. In an attempt to verify to which extent these variations could influence the final microstructure, simulations were performed in which only the niobium content in each alloy was varied. Thus, in Figure 1(a) and 1(b), the phase fractions were determined based on the chemical composition of each alloy, as presented in Table 1, for the actual 0.09 and 0.77%Nb steels, respectively. In addition, in Figure 1(c) two situations are analyzed: the niobium content is kept fixed at 0.09% and the values of the remaining elements were considered equal to those registered in Table 1 for the 0.09%Nb alloy (solid line) and for the 0.77%Nb alloy (dotted line). In Figure 1(d), the same analyses was performed but considering a fixed niobium content of 0.77%.

Considering the results presented in Figure 1(a) and 1(b), it is possible to notice that in equilibrium conditions the secondary $M_{23}C_6$ chromium carbides, NbC and (Ti,Nb)C precipitates are stable at 900°C for both analyzed compositions. On the other hand, G-phase was not found to be stable in equilibrium conditions at temperatures above 700°C. By analyzing the results of the simulated compositions presented in Figure 1(c) and 1(d), it is possible to see that the overall composition differences do promote changes in phase fraction, notably regarding the formation range of primary M_7C_3 carbides. However, the effect of niobium is predominant relative both to NbC (as expected) and secondary $M_{23}C_6$ carbide fractions in the 800 to 1100°C temperature range, which is important for the present study considering the common application conditions for these materials and the temperature employed for evaluating the oxidation resistance (900°C).

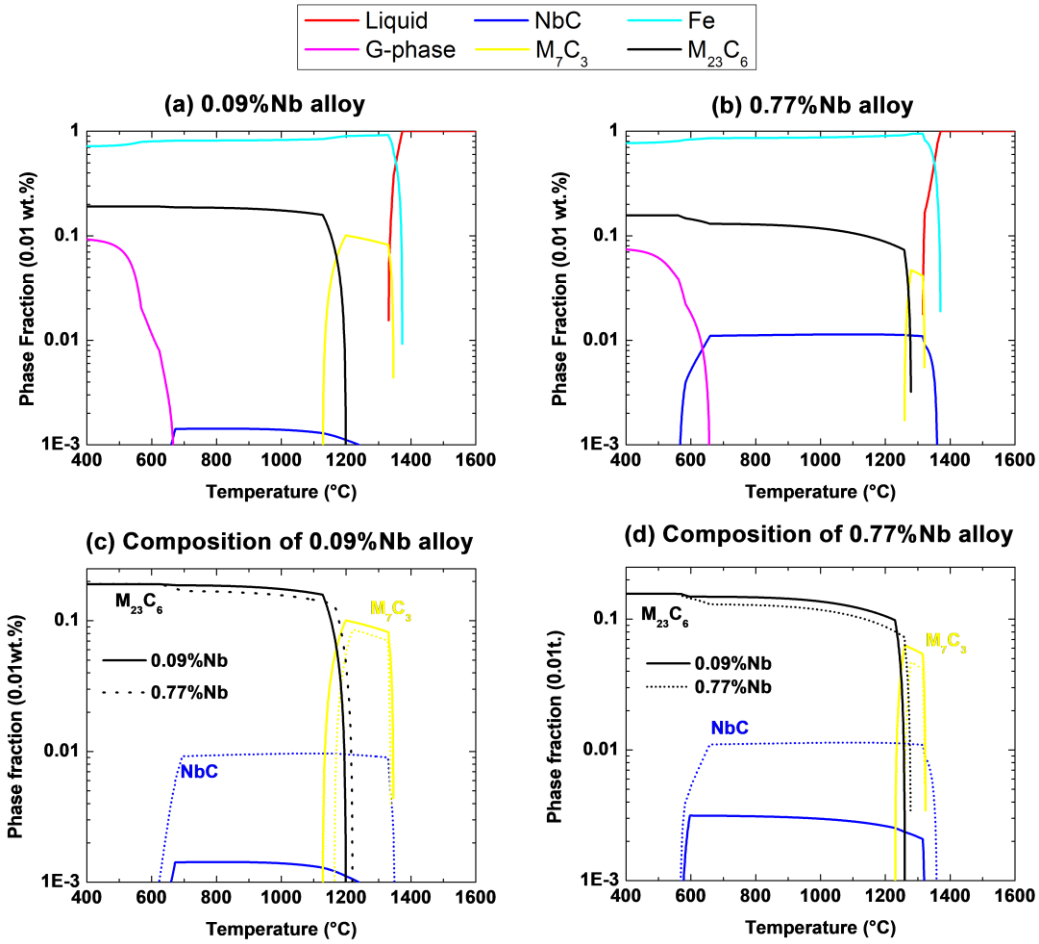

Figure 3. 1 – Phase fraction (wt%) diagrams for the modified HH steels: (a) 0.09%Nb, (b) 0.77%Nb, (c) 0.09%Nb with varying composition of the remaining elements and (d) 0.77%Nb with varying composition of the remaining elements.

The increase in niobium content from 0.09 to 0.77% is expected to favor niobium carbide precipitation and to increase the amount of chromium dissolved in the austenite matrix. This was confirmed by the thermodynamic analyses and is shown in Figure 2 which presents the chromium content of the steel matrix and carbides. The chromium enrichment of the austenite matrix indicated in Figure 2 suggests the potential for improvement in corrosion resistance. It was also possible to observe a change in the niobium-carbide to chromium-carbide ratio. In the 0.09%Nb alloy the calculated ratio between niobium carbides and chromium carbides was found to be 0.0068 while for the 0.77%Nb alloy this ratio was determined to be equal to 0.067. The results indicate therefore that with larger niobium additions, a smaller proportion of chromium carbides are formed, which increases chromium availability in the austenitic matrix.

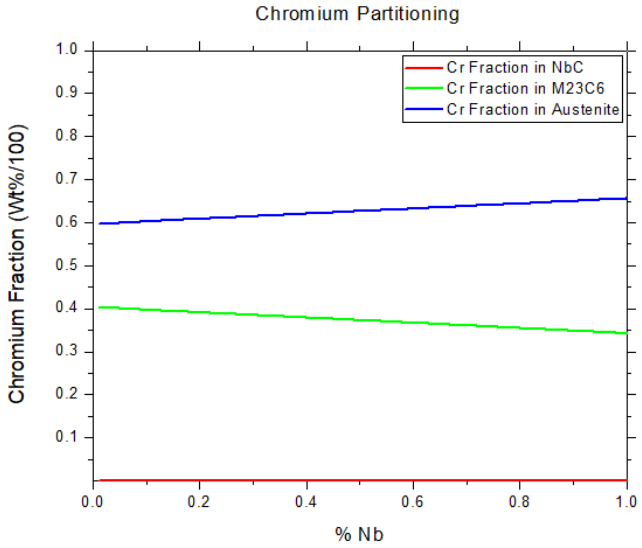

Figure 3. 2 – Chromium partitioning in phases and phase fraction (Wt%)

A sample of the modified steel microstructure is presented in Figure 3, which was obtained by SEM in backscattered secondary electron (BSE) mode to reveal differences in chemical composition in the analyzed region. The image was obtained from the aged 0.77%Nb steel (480 hours at 900°C) and the variations in contrast suggest the presence of different carbides ($M_{23}C_6$, M_7C_3, NbC and TiNbC precipitates – see Figure 8 and Table 2 for results of local composition analyses), in agreement with the results of the MatCalc® simulations presented in Figure 1. In Figure 3(b) it is possible to notice that the secondary $M_{23}C_6$ carbides present an acicular morphology.

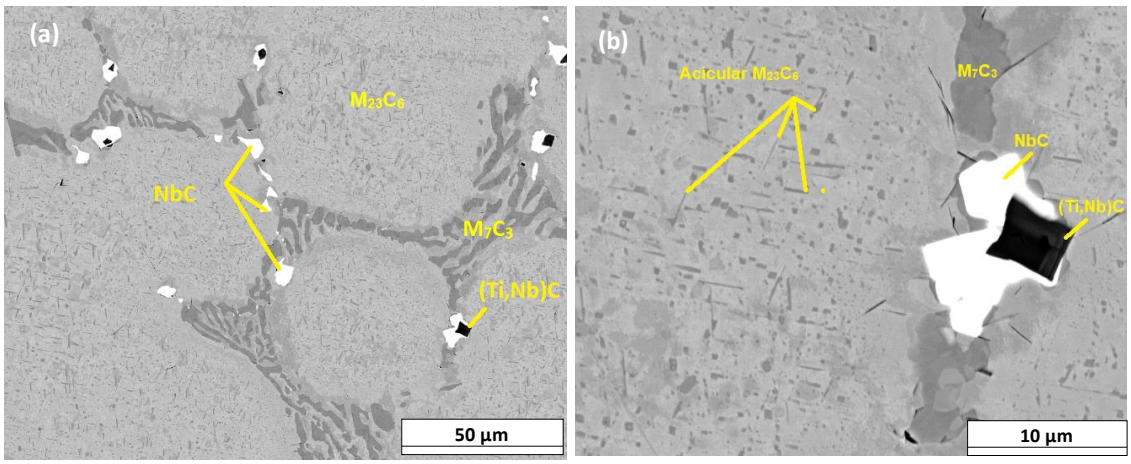

Figure 3. 3 – SEM analyses of the 0.77%Nb steel after aging at 900°C for 480 hours: (a) overview and (b) highlight of the micrustructure revealing the

presence of acicular $M_{23}C_6$ precipitates.

In Figure 4, the thermal stability of the NbC and the secondary $M_{23}C_6$ carbides is analyzed as a function of niobium content. For these calculations, the average chemical composition of the remaining elements was employed (Table 1). The results presented in Figure 4 reveal that the temperature range of both NbC and $M_{23}C_6$ increase with niobium content (the *liquidus* temperature is shifted to higher values), indicating an increase in the stability of NbC and $M_{23}C_6$ carbides, which in turn can be considered to exert a positive effect on the steel refractoriness in field applications [20].

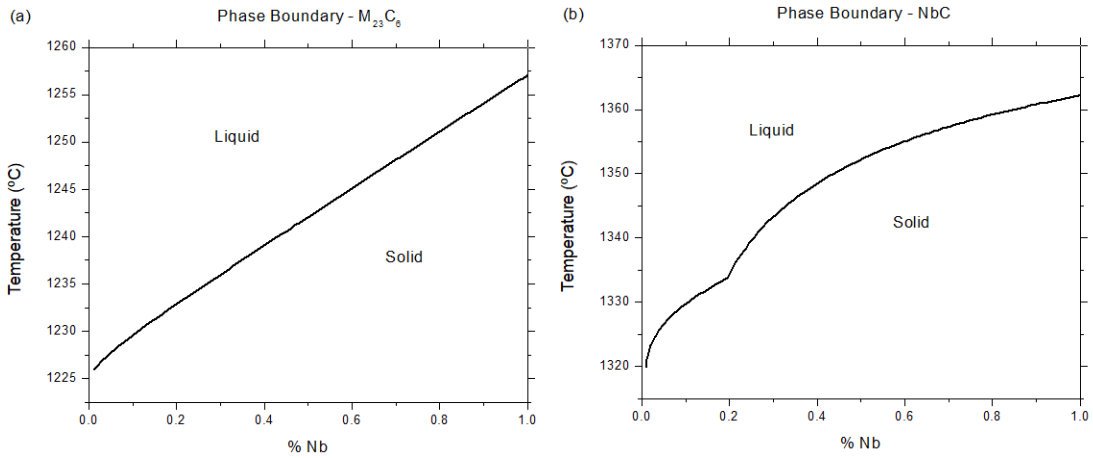

Figure 3. 4 – Phase Boundary analyses for the (a) $M_{23}C_6$ and (b) NbC carbides

In Figure 5, the carbon partitioning among NbC, $M_{23}C_6$ and the austenite matrix as well as the relative fraction of these phases are analyzed as a function of niobium content. The results obtained confirm the expected trend, that NbC formation takes place at the expense of chromium carbides as niobium content increases according to [2,17].

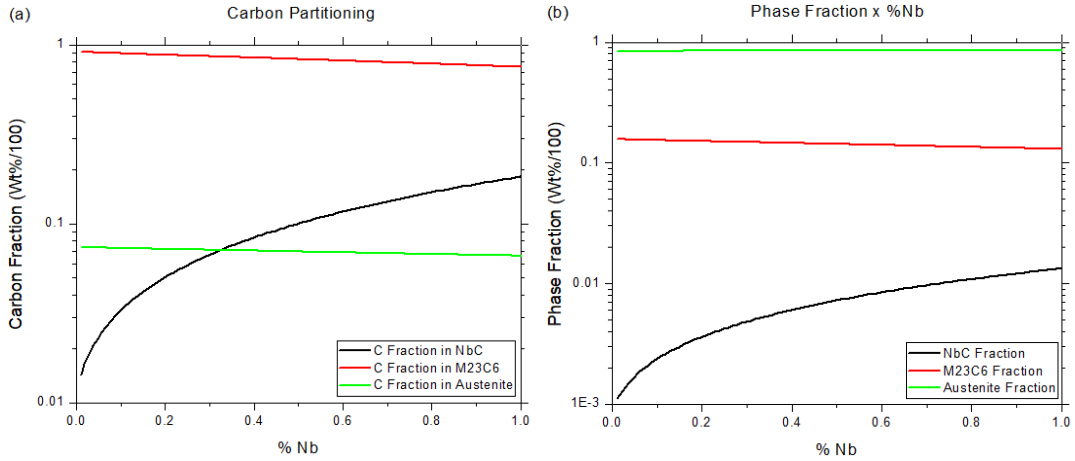

Figure 3. 5 – (a) Carbon partitioning in phases and (b) phase fraction (Wt%) as niobium increases

In Figure 6, results of the solidification process simulation performed according to Scheil model considering carbon back diffusion (same amount of carbon in the liquid and solid phases during solidification process) and 0.77%Nb alloy as Table 1 are presented. The results indicate that solidification starts at 1372° with the liquid to austenite transformation and at 1345°C formation of NbC and (Ti,Nb)C precipitates takes place. The formation of primary chromium carbides is observed at 1328°C with a liquid fraction of 28% and the solidification is concluded at 1260°C. The results obtained indicate that no other chromium carbides are expected to appear during solidification, in agreement with [4,13].

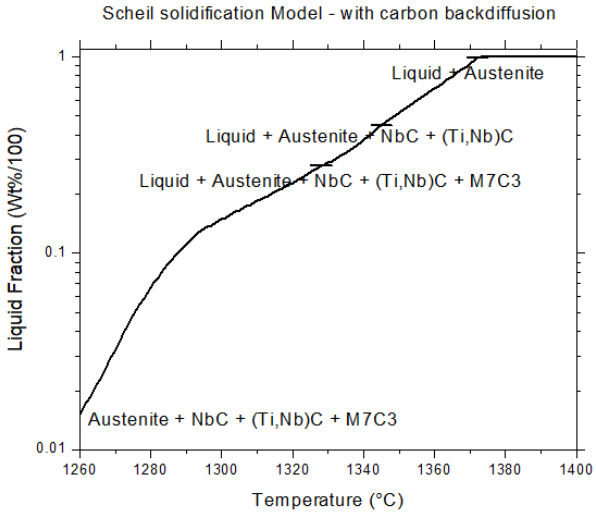

Figure 3. 6 – Simulation of the solidification process using the Scheil solidification model with back diffusion of carbon and 0.77%Nb alloy

3.3.2 Microstructure characterization

The microstructure of the materials used in this study, was observed by OM and the results are presented in Figure 7(a-d) for the 0.09% and 0.77% niobium contents in the as-cast and aged conditions, respectively. The overall as-cast phase fraction (%volume) determined by image analysis revealed that both materials exhibit originally a predominantly austenitic microstructure (approximately 92%) and close to 8% chromium, niobium and niobium-titanium carbides.

The carbides were found, as expected, at the interdendritic sites. No noticeable difference was reported for both materials when comparing as-cast and aged conditions by OM. In order to obtain more detailed information concerning precipitate composition and the finer secondary chromium carbides identified in Figure 3, SEM/EDX analyses were performed on samples in the as-cast and aged conditions, considering the predicted composition obtained by thermodynamic simulations for phase identification [21,22]. The results are presented in Figure 8(a-d).

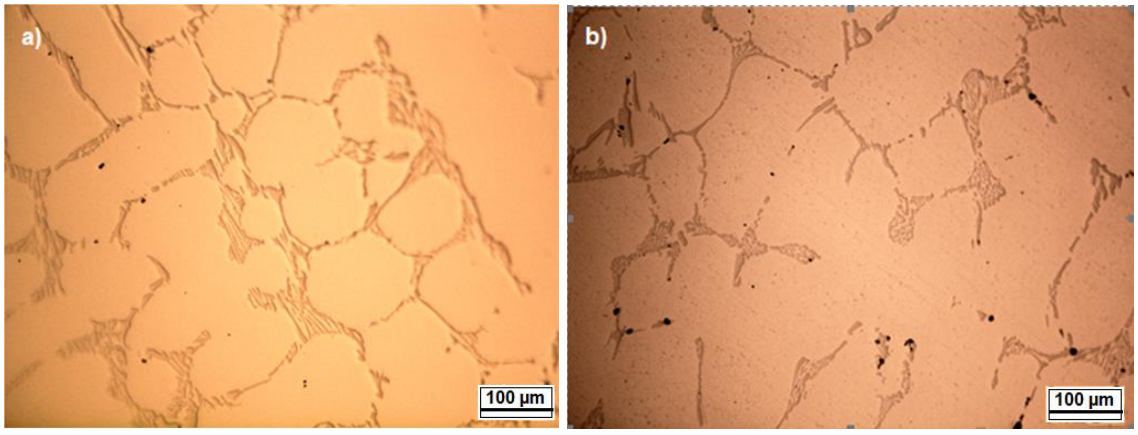

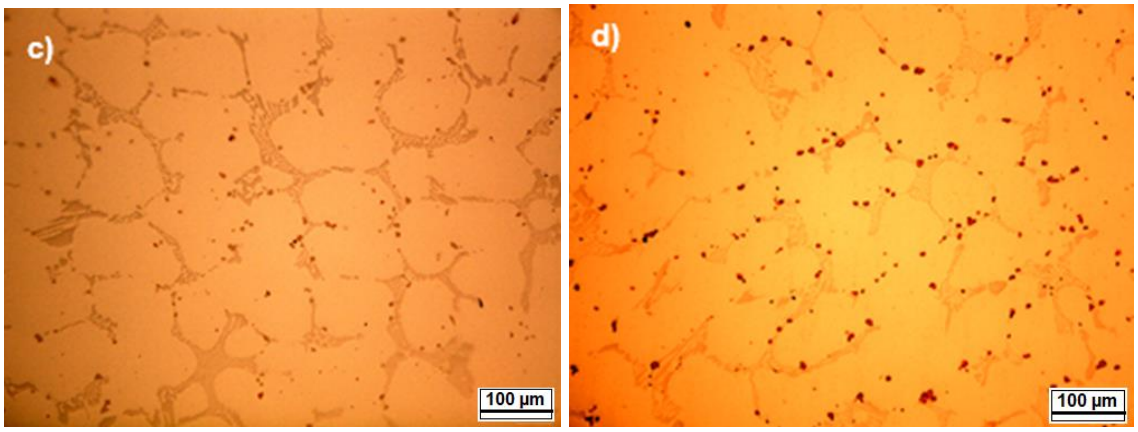

Figure 3. 7 – Optical microscopy analysis of the as-cast (a and c) and aged for 900°C for 480h (b and d) microstructures of the modified HH steel. (a-b) 0.09%Nb, (c-d) 0.77%Nb.

For the 0.09% niobium content, as expected, the microstructure is composed basically of primary chromium carbides (M_7C_3). The presence of M_7C_3 carbides could not be confirmed experimentally by XRD but would be expected in the as-cast condition, according to the simulated solidification sequence shown in Figure 6, and the equilibrium phase fractions shown in Figure 1. The chemical composition analysis by EDX (presented in Table 2), along with the carbide morphology and relative stoichiometry of the possible phases reported in previous works [21,22], further support the presence of M_7C_3 eutectic chromium carbides.

In the as-cast condition, it is possible to notice that with increasing niobium concentration (0.77%Nb), the fraction of NbC precipitates increase at the expense of chromium carbides causing an increase in the chromium levels present in the austenite matrix. This slight chromium enrichment was indicated by EDX analyses (Table 2), which revealed that in the as-cast condition the amounts of chromium present in the austenite matrix were 20% and 23% for the 0.09 and 0.77%Nb steels, respectively. In the aged condition however, further carbide precipitation takes place for both materials, and the amount of chromium in the austenite matrix is reduced (from 23 to 17% in case of the 0.77%Nb steel).

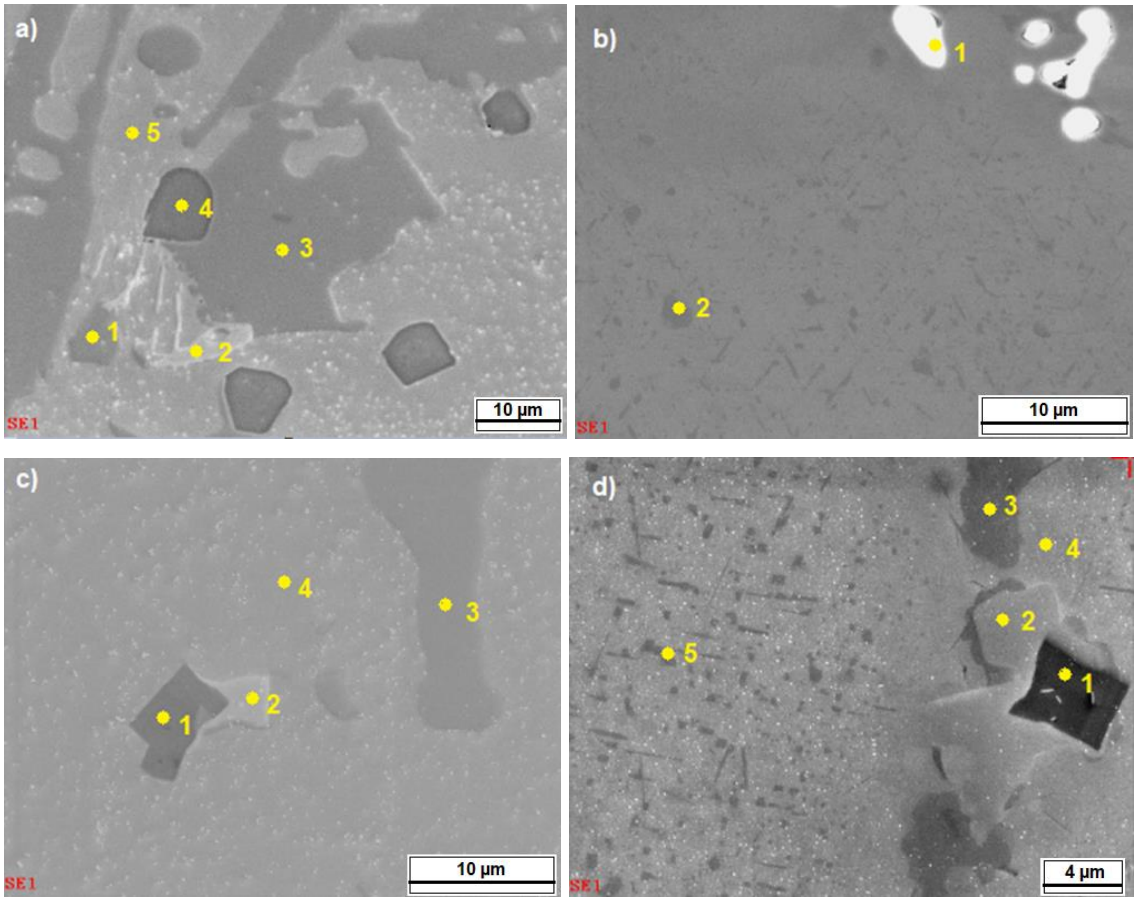

Figure 3. 8 – SEM/EDX analysis of as-cast (a, c) and aged for 900°C for 480h (b, d) microstructures of the modified HH steel (a-b) 0.09%Nb, (c-d) 0.77%Nb.

Based on the performed thermodynamic analyses (Figure 1) and considering the aging conditions employed in the present study (480 hours at 900°C), the expected precipitates are $M_{23}C_6$ secondary carbides. The larger content of chromium in solution observed for the as-cast 0.77%Nb steel apparently favored precipitation of secondary $M_{23}C_6$ carbides after aging relative to the 0.09%Nb steel, as can be noticed by comparing Figures 8(b) and 8(d). In both steels, in the aged conditions, the secondary $M_{23}C_6$ carbides exhibit an acicular morphology as previously noticed in Figure 3 and similar composition (Table 2). The carbides formed with the aging process were found to precipitate in the interior of the austenite grains, in contrast with the primary M_7C_3 primary carbides which were located at the interdendritic regions (Figure 7). The fine acicular morphology noticed for the secondary $M_{23}C_6$ carbides in Figures 3 and 8 of the present work has been previously identified in aged HP steels [23] and is probably due to the lower precipitation temperature compared to the coarser primary M_7C_3 carbides formed directly after solidification.

Table 3. 2 - Summary of the EDX analyses shown in Figure 8

Material	Spot	Composition (wt%)	Phase
As-Cast 0.09%Nb	1	77%Cr17%Nb6%C	M_7C_3
	2	92%Nb8%C	NbC
	3	77%Cr17%Nb6%C	M_7C_3
	4	55%Cr44%S1%C	Sulphur inclusion
	5	65%Fe20%Cr12%Ni2%Si1%C	Austenitic Matrix
Aged 480 h 0.09%Nb	1	64%Al36%O	Aluminium inclusion
	2	71%Cr23%Fe6%C	$M_{23}C_6$
As-Cast 0.77%Nb	1	75%Ti10%Nb14%N2%C	(Ti,Nb)C
	2	89%Nb11%C	NbC
	3	77%Cr16%Fe7%C	M_7C_3
	4	61%Fe23%Cr12%Ni2%Si2%C	Austenitic Matrix
Aged 480h 0.77%Nb	1	80%Ti9%Nb3%Cr8%C	(Ti,Nb)C
	2	87%Nb13%C	NbC
	3	76%Cr19%Fe5%C	M_7C_3
	4	66%Fe17%Cr14%Ni2%Si1%C	Austenitic Matrix
	5	70%Cr25%Fe5%C	$M_{23}C_6$

With the contrast observed for the different carbides, it was possible to perform quantitative phase analysis, which was performed by using the ImageJ software. The results are presented in Figure 9 for the as-cast samples and represent the fraction of NbC plus Cr_7C_3 relative to the austenite content. It was not possible to analyze the samples in the aged condition because of the difficulty in identifying the $Cr_{23}C_6$ carbides due to its small size.

Considering the variations in chemical composition observed in both alloys (Table 1), it is not possible to state unambiguously that niobium alone is responsible for the differences in microstructure observed in Figures 6-8. It remains nevertheless clear, however, that the two tested materials exhibited differences in microstructure consistent with the thermodynamic analyses, which indicates that the addition of niobium should lead to an overall decrease in the amount of precipitated carbides, mainly chromium carbides, in the as-cast materials.

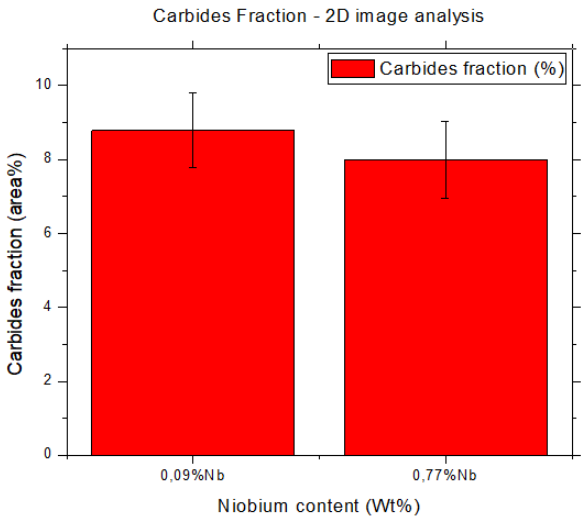

Figure 3. 9 – Carbides fraction (M_7C_3 and NbC) by 2D image analysis

The existing literature suggests that at elevated temperatures the primary chromium carbides M_7C_3 may coarsen and evolve to $M_{23}C_6$ and G-phase (high hardness interdendritic phase composed of nickel, silicon and niobium, generally with $Ni_{16}Nb_6Si_7$ stoichiometry), which is formed by NbC dissolution [2,15,24]. It was not possible to detect the presence of G-phase in the present investigation, probably because of the elevated aging temperature which was selected. According to the thermodynamic equilibrium analysis performed (see results presented in Figure 4) G-phase is unstable at 900°C and should only be present at around 600ºC. Indeed, G-phase precipitation is normally noticed during maintenance periods and with cyclic temperature operations in industry [15,25]. In previous investigations, G-phase appearance was registered in similar alloys submitted to larger aging times, such as 12 years [15] or 16 years [24], or in case of higher niobium, silicon and carbon contents in the composition as [1] during which temperature variations were more significant than in the present case of a controlled isothermal treatment at 900°C.

The more stable $M_{23}C_6$ secondary chromium carbides could be recognized only in aged samples in agreement with Scheil solidification model (first primary chromium carbides precipitation) and with equilibrium phase diagrams and kinetics precipitation simulations (more stable secondary chromium carbide precipitation after aging, see results in Section 3.2).

3.3.3 Cyclic oxidation tests

In Figure 10 the results of the mass change measurements performed during cyclic oxidation of the 0.09 and 0.77%Nb steels in atmospheric air at 900°C are presented. It is possible to notice that up to 120h under cyclic oxidation conditions, the 0.77%Nb alloyed steel exhibited more stable performance, with a lower relative mass gain compared to the modified 0.09%Nb steel. The maximum mass gain for both samples was observed after 120h hours (6 cycles), with values of 0.159 and 0.032 mg/cm^2 for the 0.09 and 0.77%Nb alloys, respectively. Subsequently, slight decreases in mass change were noticed (up to about 480h), which could be an indication of initial oxide spallation. Upon reaching 960h (9 cycles), severe mass loss was observed (-0.76 mg/cm² and -0.94 mg/cm² for the 0.09%Nb and 0.77%Nb samples, respectively). In fact, while handling samples, it was possible to notice that after 240h of cyclic oxidation oxide particles were detached from the metal surface. As such, the process of spallation in cyclic oxidation conditions was similar for both tested materials.

It is possible to speculate that the increased cyclic oxidation resistance observed for the 0.77%Nb steel for the test period of 120 h can be attributed to the lower amount of carbides in the initial as-cast condition, with higher relative amounts of chromium in the austenite matrix. However, with increasing high temperature exposure time, secondary chromium carbide precipitation takes place and the available chromium is reduced. From this point onward, oxide spallation was noticed for both materials, indicating similar long-term oxidation behavior.

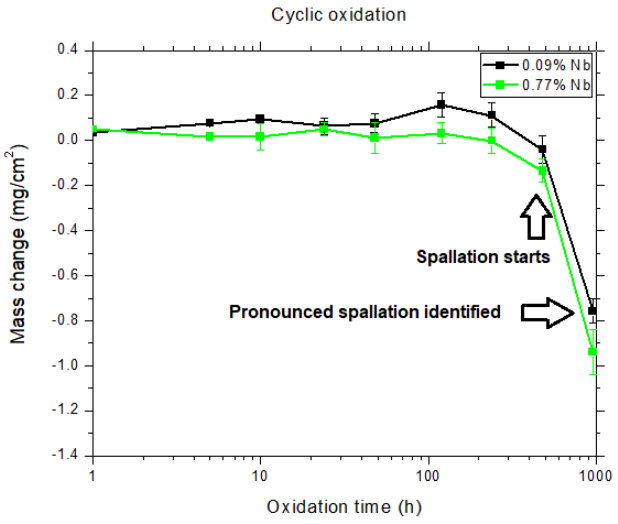

Figure 3. 10 – Cyclic oxidation tests – Atmospheric air (900°C)

3.3.3.1 Oxide layer characterization

The oxide layers formed on the 0.09 and 0.77%Nb steels after the cyclic oxidation tests were analyzed by XRD (Figure 11) and SEM/EDX (Figure 12). The results of the XRD phase analyses indicated that after 960 h cyclic oxidation in atmospheric air, the oxide scales formed on both steels present similar phase composition: Fe_2O_3 (hematite, 01-071-5088), $Cr_{0.03}Fe_{2.96}Ni_{0.01}O_4$ (mixed magnetite oxide, PDF-04-015-0675) and Cr_2O_3 (chromia, PDF-00-038-1479), in agreement with previous results obtained for this alloy in isothermal oxidation conditions [26]. The presence of iron oxides was confirmed by the SEM/EDX analyses presented in Figure 12, which reveals the presence of iron on the surface of the oxide scale (at the oxide/gas interface). Only vestiges of the iron oxide layers detected by XRD can be seen in Figure 12, however, a possible indication that these layers were removed by spallation caused by thermal cycling.

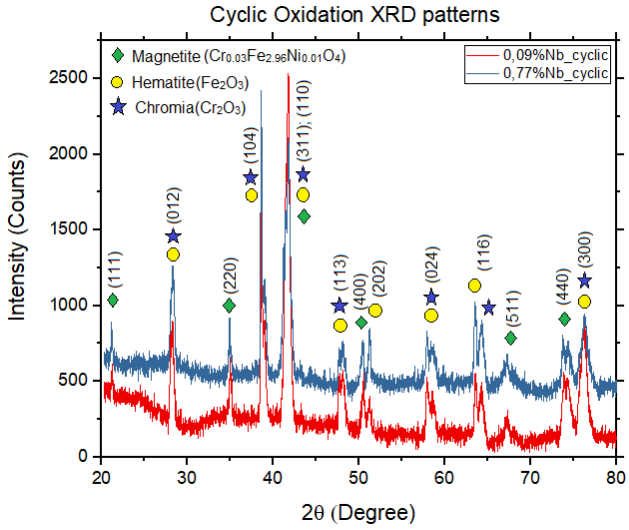

Figure 3. 11 – XRD phase analyses - Cyclic oxidation test – 960h – Atmospheric air (900°C)

The analyses performed by SEM/EDX further revealed the Cr_2O_3 is present as an inner oxide layer, in contact with the metal substrate which is an indication that this is the first formed oxide. As oxidation progresses, silicon oxide (SiO_2) forms at substrate/oxide interface, while hematite (Fe_2O_3) and mixed magnetite ($Cr_{0.03}Fe_{2.96}Ni_{0.01}O_4$) form on top of the Cr_2O_3 layer due to diffusion through the oxide scale and through cracks generated due to increase in internal stresses in this first

protective chromium layer and as the chromium availability decreases [27,28]. After the cyclic oxidation experiment, it was possible to predict the presence of cracks among the chromium oxide layer (Figure 12).

The microstructure analyses of the oxide scales did not reveal significant differences in oxidation behavior, with the same oxide phases developed on both materials (Figure 11) and similar oxide scale morphologies (Figure 12). It was also possible to notice the presence of porosities beneath the oxide/metal interface. These are caused by chromium supply to the oxide layer growth [28]. These results agree with the mass change evolution presented in Figure 10 which also showed a similar behavior towards the final stages of the oxidation process (960 hours).

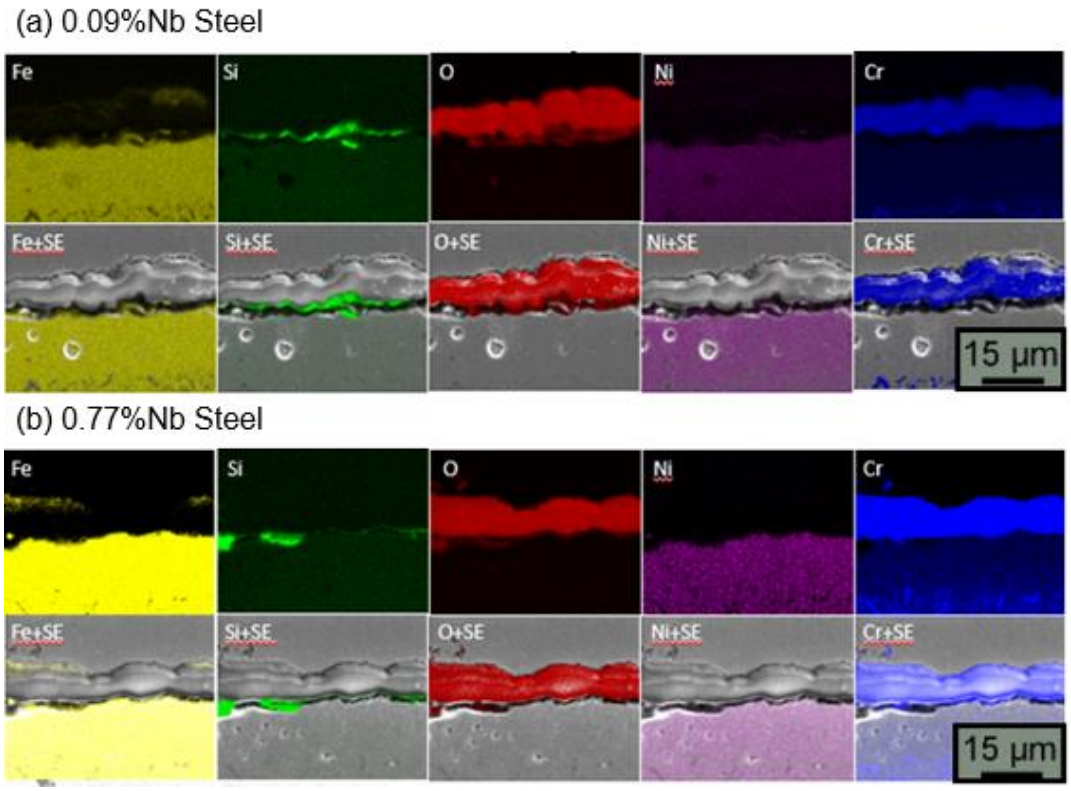

Figure 3. 12 – SEM/EDX - Cyclic oxidation test – 960h – Atmospheric air (900°C)

Figure 13 showed, with secondary electrons, more detailed layer information with chromium oxide layer as the remaining layer in good adherence with the substrate. SiO_2 phase appeared on this interface as a barrier against chromium diffusion and also giving a protective effect for this type of steel. Remaining iron oxides could also be seen on top of the layer after cyclic oxidation resulted from spallation as seen in Figure 10.

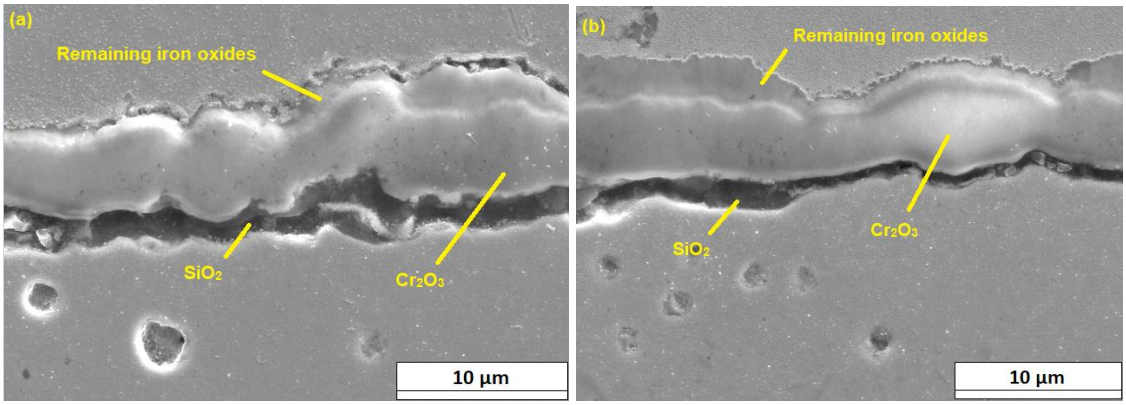

Figure 3. 13 – (a) 0.09% Nb cyclic condition SEM and (b) (a) 0.77% Nb cyclic condition SEM both with 960h at Atmospheric air (900°C)

3.4 Conclusions

In the present study, the microstructure of two modified Nb-alloyed A297 HH steels were analyzed. The experimental results were compared with thermodynamic simulations and the oxide scales developed on both steels after cyclic oxidation at 900°C in atmospheric air for 960 hours were analyzed. The following conclusions could be drawn:

- Microstructure analyses performed by OM and SEM/EDX agreed with the thermodynamic simulations in Matcalc® concerning phase precipitation and chromium content in the austenitic matrix;
- The thermodynamic simulations indicated that the presence of niobium led to an overall decrease in the carbide fraction, while increasing NbC and M_7C_3 stability.
- Microstructure and local chemical composition analyses suggest the presence of M_7C_3, $M_{23}C_6$, NbC and (Ti,Nb)C carbides in as-cast and aged condition.
- Scheil Solidification model analysis indicated the initial formation of M_7C_3 formation in place of $M_{23}C_6$ in the as-cast condition, secondary chromium carbides found in phase diagrams are the more stable form found after high temperature exposure.
- The XRD phase analyses and SEM/EDX analyses of the oxide layers indicated the presence of Fe_2O_3, $Cr_{0.03}Fe_{2.96}Ni_{0.01}O_4$ and Cr_2O_3 in the oxide scales formed on both materials. The steels also exhibited similar mass change evolution with oxidation time.

Acknowledgments

This work was financially supported by the Coordination for the Improvement of Higher Education Personnel – CAPES (grant number 88887.302880/2018-00, PROBRAL project 88881.143948/2017-01 and Finance Code 01) and by the German Academic Exchange Service – DAAD (project DAAD PPP-Brazil 2018 – ID 57390937). The authors are grateful to L. Nakamura for assistance with the thermodynamic analyses, K. Aristizabal and M. A. Guitar for SEM/EDX analyses and S. Slawik for XRD experiments.

References

[1] I.A. Sustaita-Torres, S. Haro-Rodríguez, M.P. Guerrero-Mata, M. De La Garza, E. Valdés, F. Deschaux-Beaume, R. Colás, Aging of a cast 35Cr-45Ni heat resistant alloy, Mater. Chem. Phys. 133 (2012) 1018–1023. https://doi.org/10.1016/j.matchemphys.2012.02.010.

[2] M. Abbasi, I. Park, Y. Ro, Y. Ji, R. Ayer, J.H. Shim, G-phase formation in twenty-years aged heat-resistant cast austenitic steel reformer tube, Mater. Charact. 148 (2019) 297–306. https://doi.org/10.1016/j.matchar.2019.01.003.

[3] N. Madern, J. Monnier, R. Baddour-Hadjean, A. Steckmeyer, J.M. Joubert, Characterization of refractory steel oxidation at high temperature, Corros. Sci. 132 (2018) 223–233. https://doi.org/10.1016/j.corsci.2017.12.029.

[4] Y.X. Xu, J.T. Lu, X.W. Yang, J.B. Yan, W.Y. Li, Effect and role of alloyed Nb on the air oxidation behaviour of Ni-Cr-Fe alloys at 1000 °C, Corros. Sci. 127 (2017) 10–20. https://doi.org/10.1016/j.corsci.2017.08.003.

[5] G.D. de Almeida Soares, L.H. de Almeida, T.L. da Silveira, I. Le May, Niobium additions in HP heat-resistant cast stainless steels, Mater. Charact. 29 (1992) 387–396. https://doi.org/10.1016/1044-5803(92)90045-J.

[6] G.D. Barbabela, L.H. de Almeida, T.L. da Silveira, I. Le May, Role of Nb in modifying the microstructure of heat-resistant cast HP steel, Mater. Charact. 26 (1991) 193–197. https://doi.org/10.1016/1044-5803(91)90053-7.

[7] L.H. De Almeida, A.F. Ribeiro, I. Le May, Microstructural characterization of modified 25Cr-35Ni centrifugally cast steel furnace tubes, Mater. Charact. 49 (2002) 219–229. https://doi.org/10.1016/S1044-5803(03)00013-5.

[8] J. Yan, Y. Gu, Y. Dang, X. Zhao, J. Lu, Y. Yuan, Z. Yang, H. Yin, Effect of carbon on the microstructure evolution and mechanical properties of low Si-containing centrifugal casting 20Cr32Ni1Nb alloy, Mater. Chem. Phys. 175 (2016) 107–117. https://doi.org/10.1016/j.matchemphys.2016.02.077.

[9] K.G. Buchanan, M. V. Kral, Crystallography and morphology of niobium carbide in as-cast HP-niobium reformer tubes, Metall. Mater. Trans. A Phys. Metall. Mater. Sci. 43 (2012) 1760–1769. https://doi.org/10.1007/s11661-011-1025-0.

[10] V. Javaheri, F. Shahri, M. Mohammadnezhad, M. Tamizifar, M. Naseri, The effect of Nb and Ti on structure and mechanical properties of 12Ni-25Cr-0.4C

austenitic heat-resistant steel after aging at 900 °c for 1000 h, J. Mater. Eng. Perform. 23 (2014) 3558–3566. https://doi.org/10.1007/s11665-014-1009-5.

[11] A. Alvino, D. Ramires, A. Tonti, D. Lega, Influence of chemical composition on microstructure and phase evolution of two HP heat resistant stainless steels after long term plant-service aging, Mater. High Temp. 31 (2014) 2–11. https://doi.org/10.1179/0960340913Z.0000000001.

[12] F.C. Nunes, L.H. de Almeida, J. Dille, J.L. Delplancke, I. Le May, Microstructural changes caused by yttrium addition to NbTi-modified centrifugally cast HP-type stainless steels, Mater. Charact. 58 (2007) 132–142. https://doi.org/10.1016/j.matchar.2006.04.007.

[13] M. Viherkoski, E. Huttunen-Saarivirta, E. Isotahdon, M. Uusitalo, T. Tiainen, V.T. Kuokkala, The effect of aging on heat-resistant cast stainless steels, Mater. Sci. Eng. A. 589 (2014) 189–198. https://doi.org/10.1016/j.msea.2013.09.074.

[14] H. Chen, H. Wang, Q. Sun, C. Long, T. Wei, S.H. Kim, J. Chen, C. Kim, C. Jang, Oxidation behavior of Fe-20Cr-25Ni-Nb austenitic stainless steel in high-temperature environment with small amount of water vapor, Corros. Sci. 145 (2018) 90–99. https://doi.org/10.1016/j.corsci.2018.09.016.

[15] S. Shi, J.C. Lippold, Microstructure evolution during service exposure of two cast, heat-resisting stainless steels - HP-Nb modified and 20-32Nb, Mater. Charact. 59 (2008) 1029–1040. https://doi.org/10.1016/j.matchar.2007.08.029.

[16] J.H. Shim, E. Kozeschnik, W.S. Jung, S.C. Lee, D.I. Kim, J.Y. Suh, Y.S. Lee, Y.W. Cho, Numerical simulation of long-term precipitate evolution in austenitic heat-resistant steels, Calphad Comput. Coupling Phase Diagrams Thermochem. (2010). https://doi.org/10.1016/j.calphad.2010.01.001.

[17] J.M. Joubert, W. St-Fleur, J. Sarthou, A. Steckmeyer, B. Fournier, Equilibrium characterization and thermodynamic calculations on highly alloyed refractory steels, Calphad Comput. Coupling Phase Diagrams Thermochem. (2014). https://doi.org/10.1016/j.calphad.2014.02.002.

[18] E. Kozeschnik, J. Svoboda, P. Fratzl, F.D. Fischer, Modelling of kinetics in multi-component multi-phase systems with spherical precipitates II: Numerical solution and application, Mater. Sci. Eng. A. A385 (2004) 157–165. https://doi.org/10.1016/j.msea.2004.06.016.

[19] E. Kozeschnik, J. Svoboda, F.D. Fischer, Modified evolution equations for the

precipitation kinetics of complex phases in multi-component systems, Calphad Comput. Coupling Phase Diagrams Thermochem. 28 (2004) 379–382. https://doi.org/10.1016/j.calphad.2004.11.003.

[20] C.Y. Chen, H.W. Yen, F.H. Kao, W.C. Li, C.Y. Huang, J.R. Yang, S.H. Wang, Precipitation hardening of high-strength low-alloy steels by nanometer-sized carbides, Mater. Sci. Eng. A. 499 (2009) 162–166. https://doi.org/10.1016/j.msea.2007.11.110.

[21] J. Laigo, F. Christien, R. Le Gall, F. Tancret, J. Furtado, SEM, EDS, EPMA-WDS and EBSD characterization of carbides in HP type heat resistant alloys, Mater. Charact. 59 (2008) 1580–1586. https://doi.org/10.1016/j.matchar.2008.02.001.

[22] M. Mohammadnezhad, V. Javaheri, M. Shamanian, S. Rizaneh, J.A. Szpunar, Insight to the microstructure characterization of a HP austenitic heat resistant steel after long-term service exposure, Acta Metall. Slovaca. 24 (2018) 1160. https://doi.org/10.12776/ams.v24i4.1160.

[23] K. Shinozaki, H. Kuroki, Y. Nakao, K. Nishimoto, M. Inui, M. Takahashi, Deterioration of weldability of long-term aged HP heat-resistant cast steel containing Nb, Mo, and W, Weld. Int. 13 (1999) 39–48. https://doi.org/10.1080/09507119909452053.

[24] M.P. Dewar, A.P. Gerlich, Correlation between experimental and calculated phase fractions in aged 20Cr32Ni1Nb austenitic stainless steels containing nitrogen, Metall. Mater. Trans. A Phys. Metall. Mater. Sci. 44 (2013) 627–639. https://doi.org/10.1007/s11661-012-1457-1.

[25] K. HASEGAWA, Repair welding and metallurgy of HP-modified alloy after long term operation., Met. 2001. 5 (2001) 15–17.

[26] P. Ramos, R.S. Coelho, F. Soldera, H.C. Pinto, F. Mücklich, P. Brito, Residual stress analysis in thermally grown oxide scales developed on Nb-alloyed refractory austenitic stainless steels, Corros. Sci. 178 (2021) 109066. https://doi.org/10.1016/j.corsci.2020.109066.

[27] X. Zhang, D. Li, Y. Li, S. Lu, Effect of aging treatment on the microstructures and mechanical properties evolution of 25Cr-20Ni austenitic stainless steel weldments with different Nb contents, J. Mater. Sci. Technol. 35 (2019) 520–529. https://doi.org/10.1016/j.jmst.2018.10.017.

[28] N. Birks, G.H. Meier, F.S. Pettit, Introduction to the high temperature oxidation

of metals, Second edition, 2006. https://doi.org/10.1017/CBO9781139163903.

4 ARTICLE 2 - OXIDE LAYER EVOLUTION OF CAST Fe24Cr12NiXNb HEAT-RESISTANT CAST STEELS AT 900°C IN ATMOSPHERIC AIR

The chapter 4 refers to the results obtained in this article mentioned in the title of the chapter. It was written in article format and the format followed the guidelines of the journal.

Authors:

Ramos, P. A., Coelho, R.S., Pinto, H.C., Soldera, F., Mücklich, F., Brito, P. P.

Paper published by Archives of Foundry Engineering.

RAMOS, P. A. *et al.* Oxide Layer Evolution of Cast Fe24Cr12NiXNb Heat-Resistant Cast Steels at 900° C in Atmospheric Air. **Archives of Foundry Engineering**, p. 119-124-119-124, 2021.

Oxide Layer Evolution of Cast Fe24Cr12NiXNb heat-resistant cast steels at 900°C in Atmospheric Air

Abstract

The austenitic stainless steels are a group of alloys normally used under high mechanical and thermal requests, in which high temperature oxidation is normally present due to oxygen presence. This study examines the oxide layer evolution for Fe24Cr12NiXNb modified austenitic stainless steel A297 HH with 0,09%Nb and 0,77%Nb content at 900°C under atmospheric air and isothermal oxidation. The modifiers elements such as Mo, Co and Ti, added to provide high mechanical strength, varied due to the casting procedure, however main elements such as Cr, Ni, Mn and Si were kept at balanced levels to avoid microstructure changing. The oxide layer analysis was performed by confocal laser scanning microscopy (CLS) and scanning electron microscopy (SEM). The elemental analysis of the different phases was measured with energy dispersive X-ray spectroscopy (EDX). The Nb-alloyed steel generated a thicker Cr oxide layer. Generally elemental Nb did not provide any noticeable difference in oxide scale growth, for the specific range of Nb amount and temperature studied. High temperature oxidation up to 120h was characterized by protective Cr oxidation, after this period a non-protective Fe-based oxidation took place. Cr, Fe and Ni oxides were observed in the multilayer oxide scale.

Key-Words: Austenitic heat-resistant cast steels, Microstructure, Nb-alloyed Steels, Oxide Scale, High Temperature Oxidation.

4.1 Introduction

Austenitic heat resistant cast stainless steels (ASTM A297) are commonly used in reformer furnaces, petrochemical industry and nuclear power plants (~900°C) due to their high oxidation and mechanical resistance at elevated temperatures [1]. These steels have usually Fe, Cr, and Ni as main alloy elements, with some other elements in small amounts to improve, among others, mechanical properties [1–7].

The high temperature oxidation resistance supposes to be obtained by the formation of a protective barrier (oxide scale) between gaseous atmosphere and metal substrate. The oxidation resistance can be achieved, if a good maintenance of this scale and its stability is ensured [8]. Li *et al.* [9] showed that the oxidation behavior depends on several mixed factors such as microstructure, chemical composition of the substrate as well as oxidation condition (isothermal or cyclic) [9–12].

The most extensively investigated class of cast A297 steel , is HP grade, since it has good mechanical behavior (the higher Ni content the better the creep properties in comparison with other A297 grades) [13–15]. The A297 HH steel is an alternative with lower nickel content compared to HP and HK grades, having general composition Fe24Cr12NiχNb (in wt%), and having been developed for better cost-benefit without neglecting its performance. The reduction in Ni content, which consequently produces a decrease in creep properties, requires the increment of new elements such as Co, Ti, and Nb to enhance mechanical properties. In last years the Nb addition has been investigated with the objective of increasing high temperature strength by the precipitation of Nb carbides[1] in the austenitic matrix.

The addition of niobium may change carbide fraction (normally Cr7C3 and Cr23C6) modifying the Cr content in solution. However, the oxide scale evolution depending on the Nb additions is not fully understood [2]. The understanding of oxidation mechanisms and oxide layer development is an important issue closely related with microstructure[16], oxidation properties [17] and improvement in the material life cycle. Since we have a new modified steel, in the present work an experimental investigation was carried out in order to characterize the oxide scale evolution of this Fe24Cr12NiχNb steel (A297 modified HH steel) at 900°C under atmospheric air on

isothermal oxidation which is considered the standard conditions in most field applications.

4.2 Experimental procedure

The austenitic stainless steel A297 Gr. HH modified (Fe24Cr12Ni) with different Nb contents used in the present study were produced by FULIG® casting company and are currently used in high temperature applications. The heat-resistant cast austenitic stainless steels were characterized by chemical composition, as presented in Table 1, by using spectrometer SHIMADZU OES 5500 II. They will be called samples 0,09%Nb and 0,77%Nb.

Table 4. 1 - Chemical composition of the materials employed in the study (wt%)

A297 HH	0.77% Nb	0.09% Nb	Standard limits A297 (max.)
C (mod.*)	0.73	0.89	0.2-0.5
Si	0.97	1.23	2.00
Mn	0.55	0.50	2.00
P	0.01	0.03	0.04
S	0.02	0.03	0.04
Ni	11.09	12.12	11.0-14.0
Cr	24.79	24.42	24.0-28.0
Mo	0.32	0.12	0.5
Co (modified)	0.28	0.47	-
Nb (modified)	0.77	0.09	-
Ti (modified)	0.10	0.01	-
Fe	60.32	59.74	Balance

**Mod.: modified*

The percentages of alloying elements were all of them within A297 standard limits, as well as the levels of impurities, such as P and S.

The long-term high temperature oxidation experiments were performed in a muffle furnace for different isothermal conditions at 900 °C under room air with the different checking times of 1h, 5h, 10h, 24h, 48h, 120h, 240h, 480h and 960h and

the samples were previously polished (Up to SiC grade 600). Foremost, the generated raw oxide layers were characterized by Olympus OLS4100 confocal 3D laser scanning microscopy (CLM).

Then, the cross sections were prepared and covered with plasma sputtering process with 8% Au + 20% Pd at argon pressure of 0,02 mbar, 20-25 mA current for 5 minutes resulting in a 20nm layer making the oxide scale electrically conductive. Thus, electrochemical copper deposition could be done with a copper sheet immersed in a copper solution (20g CuSO4 + 100gH2O) at 1,5V(DC) for 15 min which generated a copper layer above the oxide around 10µm, that is mandatory to avoid oxide scale spallation due to preparation before mounting in conductive resin. Then, metallographic sample preparation was performed up to 0,05 µm with alumina solution at vibratory polisher machine (VIBROMET 2 - BUEHLER) without etching. The three pieces of each sample were measured in order to provide statistics. Samples for microstructural analysis and oxidation tests were cut from the cast blocks with cubic dimensions of 10 x 10 x 10 mm.

The oxide scale morphology, cross section and chemical elements distribution was characterized by a dual-beam focused ion beam/scanning electron microscopy (FIB/SEM) workstation (FEI Helios NanoLab 600) equipped with EDAX energy dispersive X-ray spectroscopy module (EDX).

4.3 Results and discussion

4.3.1 Alloys microstructure

Optical micrographs obtained from the microstructure of the samples 0.09%Nb and 0.77%Nb are presented in Figure 1. They exhibit differences regarding precipitation and dendritic form. The austenitic matrix contains Cr and also Nb/Ti precipitates mainly seen in 0.77%Nb alloy.

In Figure 1(a) the microstructure of the 0.09%Nb alloy is presented revealing precipitates with the typical morphology of primary Cr carbides. In Figure 1(b) the microstructure of the 0.77%Nb alloy is shown, exhibiting the same primary Cr carbides along with new precipitates which were precipitated by the increase in niobium and titanium content.

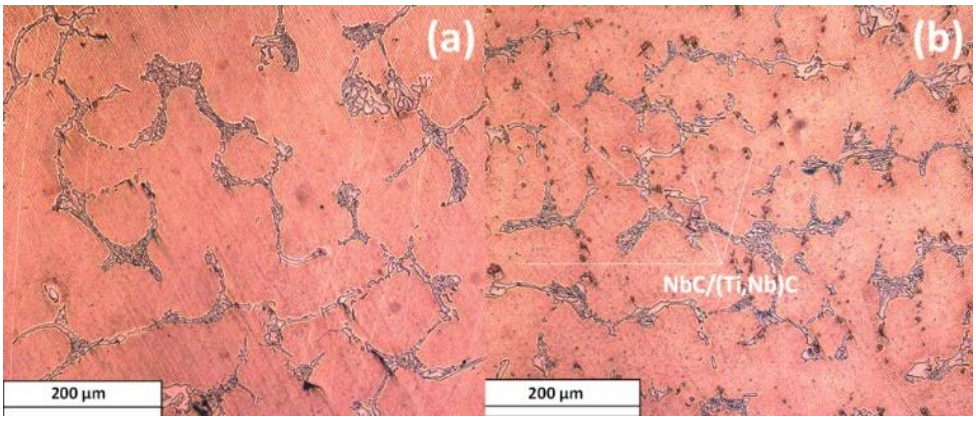

Figure 4. 1 – Optical micrograph of 0.09%Nb(a) and 0.77%Nb(b) alloy

Nb addition provide bigger carbide precipitation and, in this research, we investigated the oxide layer formation during high temperature oxidation in order to analyze whether microstructural changes affects oxide layer formation or not.

4.3.2 Oxide layer evolution and morphology

Considering optical laser micrographs obtained from samples 0.09%Nb and 0.77%Nb which are presented in Figure 2 (superficial morphology) and were obtained from samples after cooling and before plasma sputtering covering (as oxidized condition), it is possible to see clearly the oxides development starting with thin gold color oxide layer (1h), followed by other layer characterized here by darker tones (5h up to 120h) and finally covered by gray layer (clearly seen after 240h).

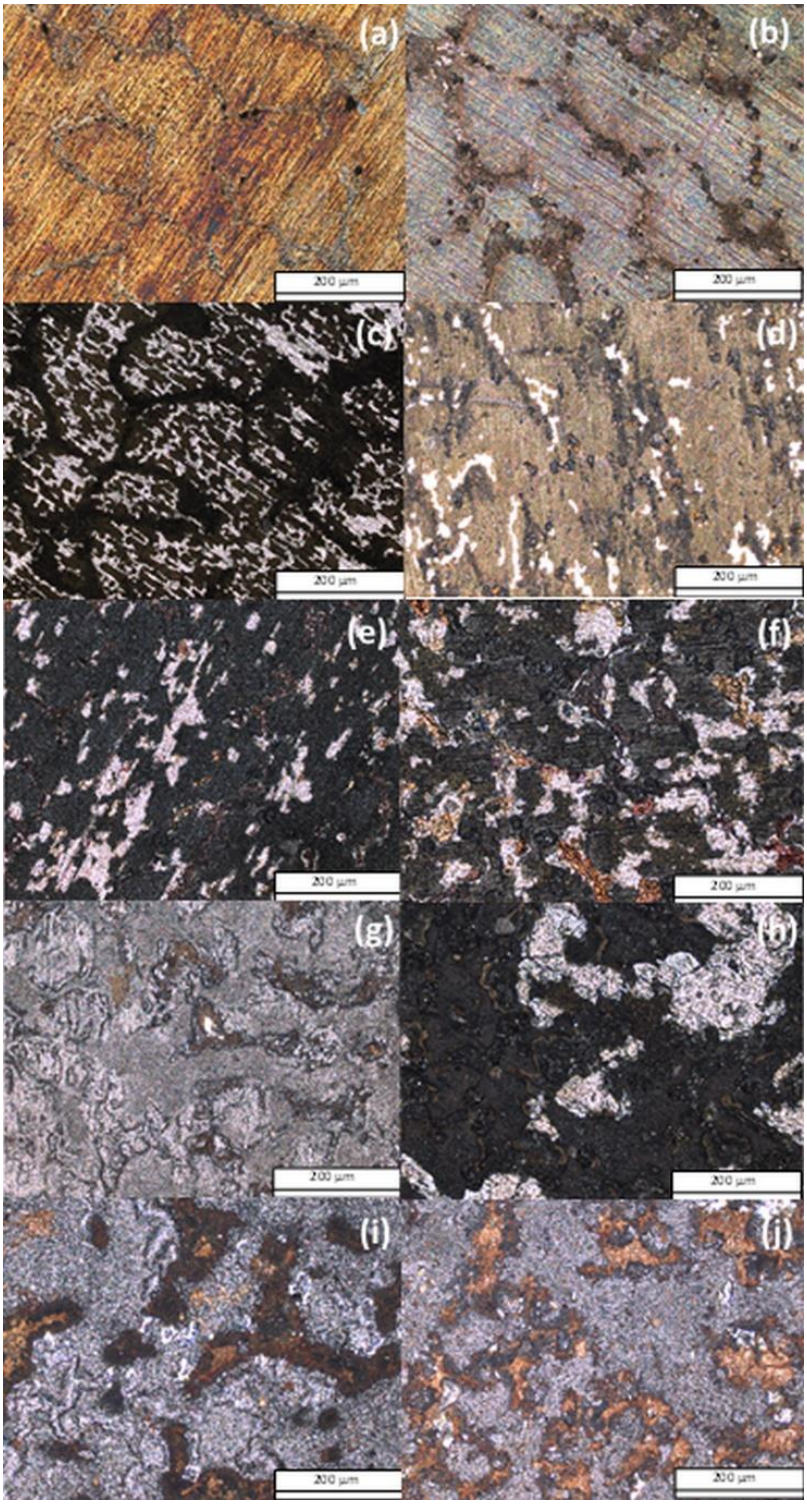

Figure 4. 2 – Oxide layer top morphology observed by optical laser microscopy of samples with 1h(a-b), 5h(c-d), 120h(e-f), 240h(g-h), 960h(i-j) for 0.09%Nb and 0.77%Nb alloy, respectively

The differences between alloys were more significant in 1h and 5h during the beginning of oxidation suggested by chemical composition differences. The oxides

have a spinel-like structure, without visible nodules or cracks on the surface. The oxides formation occurs in the form of islands that keep closer and closer until they form a consistent layer. This formation occurs initially in the dendritic boundaries that is a diffusivity favored region initially for Cr ions and later for the Ni and Fe ions as expected in this kind of steels.

The next step was the observation of oxide layer cross sections after metallographic preparation with copper covering and carefully polishing as described in section 2 of this manuscript. Considering optical laser micrographs obtained from samples 0.09%Nb and 0.77%Nb which are presented in Figure 3 (cross-section). Copper covering was more suitable than Ni covering for protecting the scales during polishing.

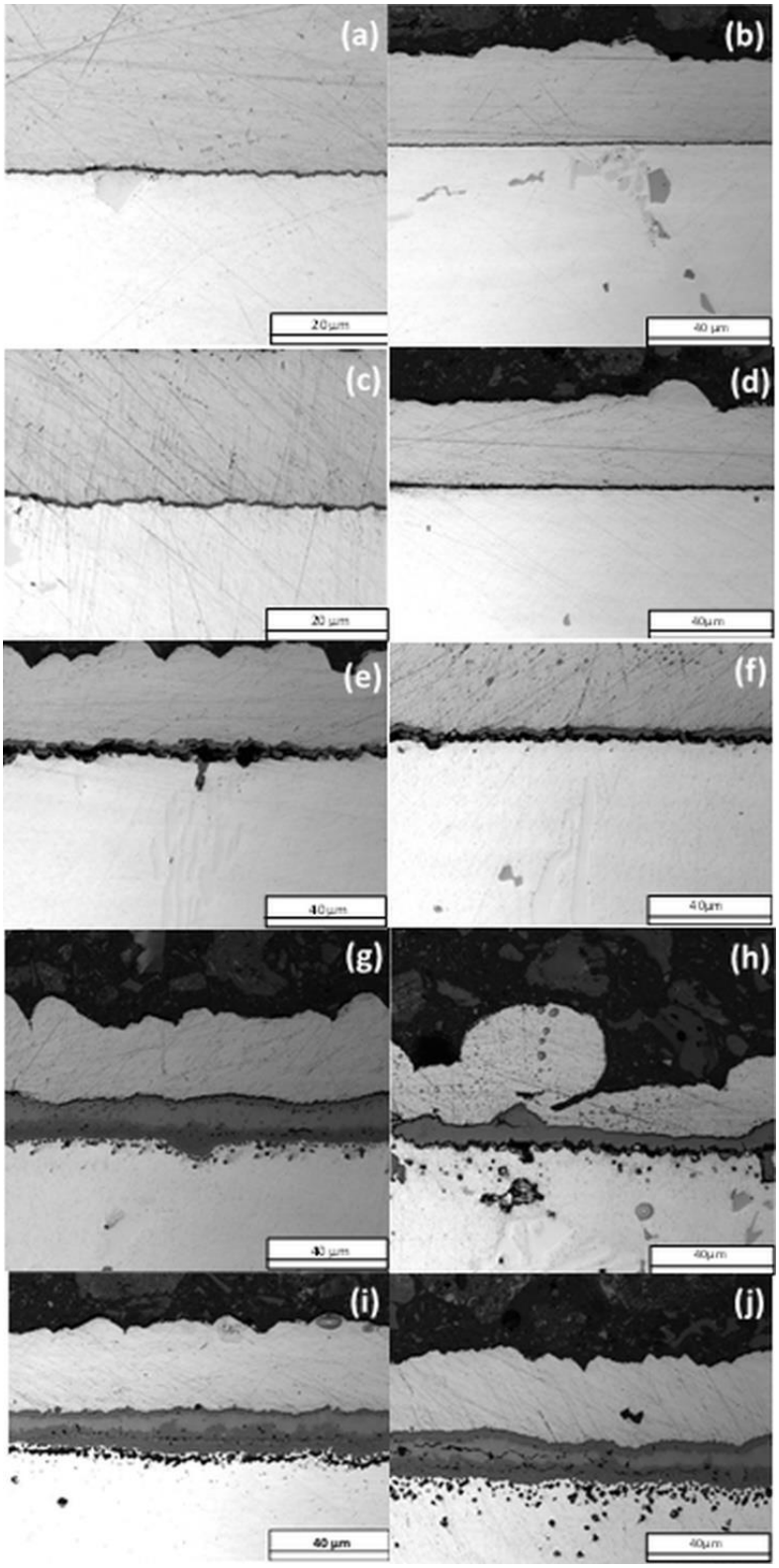

Figure 4. 3 – Oxide layer cross section by optical laser microscopy of samples with 1h(a-b), 5h(c-d), 120h(e-f), 240h(g-h), 960h(i-j) for 0.09%Nb and 0.77%Nb alloy, respectively

In Figure 3, it is possible to determine an oxide growth evolution starting with 1h up to 960h. The optical contrast suggested also a multilayer oxide scale as predicted by top morphology images and also some cracks are now seen due to residual stress caused by fast cooling rates and differences between oxide and metallic substrate thermal expansion coefficients or even due to polishing procedure.

However, from the cross section it is possible to determine in a better way the growth mechanisms and the position of each type of oxide generated in the scale from the substrate [8].

4.3.3 Oxide layer microstructure

The superficial morphology and cross section images were co-related with scanning electron micrographs obtained from samples 0.09%Nb and 0.77%Nb which are presented in Figure 4 (secondary electrons mode).

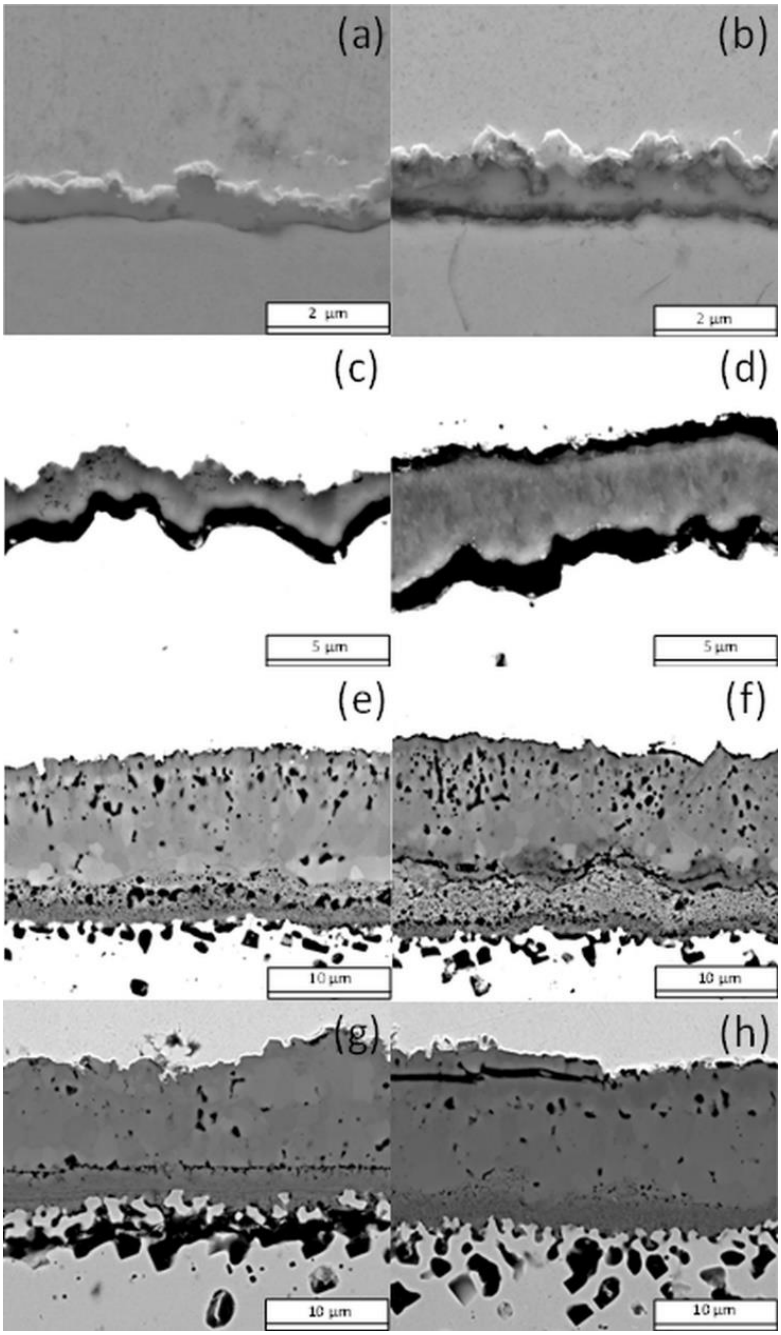

Figure 4. 4 – Oxide layer cross section by scanning electron microscopy of samples 5h(a-b), 120h(c-d), 240h(e-f), 960h(g-h) for 0.09%Nb and 0.77% alloy, respectively

Previous research described through XRD analysis that Cr oxide, magnetite (Cr0.03Fe2.96Ni0.01O4) and hematite were the phases found in both oxide scales here analyzed [17].

For layers up to 120h of oxidation a dense Cr oxide layer is observed which becomes porous overtime, consequently facilitating the others ions diffusion through it. At 240h a multilayer oxide scale is already observed with the appearance of Fe oxides immediately above the Cr oxide. This effect lasts until 960h of oxidation.

Nevertheless, for a more precise knowledge about phase formation and detailed spatial configuration of the phases other techniques related with chemical composition needed be employed like EDX linescans profiles. These analyses can be seen on Figures 5 and 6.

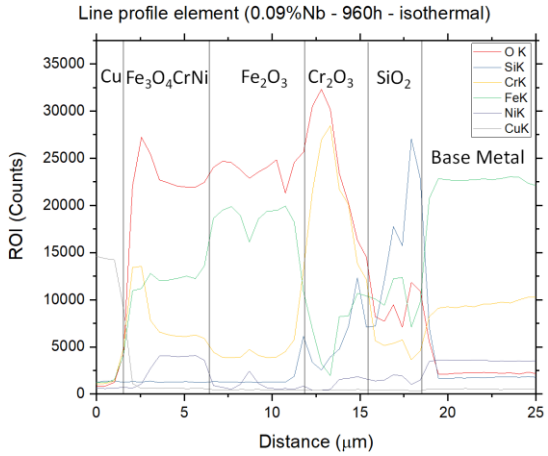

Figure 4. 5 – Oxide layer cross section EDX linescans profile by scanning electron microscopy of samples with 960h of isothermal oxidation, for 0.09%Nb alloy

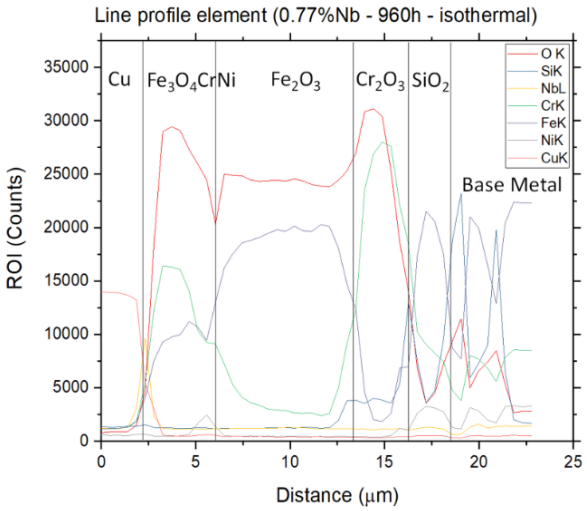

Figure 4. 6 – Oxide layer cross section EDX linescans profile by scanning electron microscopy of samples with 960h of isothermal oxidation, for 0.77%Nb alloy.

With these observations was figured out that up to 120h there is a protective oxidation due to slower thickness evolution and to be just one single chemical composition on the scale, in this case, Cr oxide.

After 240h a non-protective oxidation was observed with multilayer generation and faster thickness growth. Detailed information about the oxide layer formation can just be established with EDX linescans profiles of longest time, so approaching all phases generated during the scale formation.

The austenitic heat resistant steels exposed to high temperatures at atmospheric air generates multiple oxide scale with different phases [2]. Ellingham diagrams are reasonable way to get some information about the growth of these scales, but also other factors can influence in which oxides appear first, like ions diffusion, for example.

Basically, the oxides stability at Ellingham diagrams is based on Gibbs free energy in such reaction for oxide formation. The most thermodynamically stable phases are found close to the substrate and are formed first, being necessary also understand the diffusion, as reported by Wagner theory, in high temperature conditions [8,18] to understand the oxides growth sequence.

In the present work, according to Ellingham diagrams the oxide scale predicted formation were Si oxide (SiO2), Cr oxide (Cr2O3), Fe oxide (magnetite and hematite) considering down-top order from the substrate. This correlates reasonably

the empirical experiments, as can be seen in Figure 5 and 6. It is worth noticing that the oxide scales formed on pure iron (or carbon steels) is structured (from the substrate upwards) by layers of FeO, Fe3O4 and Fe2O3. In the present case, the order is inverted because Fe2O3 is found closer to the substrate (with Cr2O3) due to crystal structure compatibility (Fe2O3 and Cr2O3 both exhibit rhombohedral crystal structures).

The Si and Cr oxides can be considered as protective scales. The diffusivity through Cr oxide is a determinant factor for the formation of non-protective Fe-based oxides [7], as well as oxygen diffusion through the layer and spallation due to cracks formation when oxide scale is submitted to high stress state due to thermal expansion difference during the cooling cycle [8,17].

4.4 Conclusions

In the present work, the ASTM A297 Gr. HH modified austenitic heat-resistant cast steels oxide scale evolution containing 0.09%Nb and 0.77%Nb was investigated. The oxide layers' investigation included superficial observation up to use of techniques such as SEM and EDX analysis to identify the phases. The set of all these analyzes allowed the characterization of the layers. The following conclusions could be done:

- The addition of niobium did not impair the oxidation resistance of the modified steel, since no noticeable differences on oxide scales was observed related to microstructural characteristics or different alloys compositions;
- High temperature oxidation up to 120h was characterized by protective Cr oxidation, after this period a non-protective Fe-based oxidation started generating a multilayer oxide scale;
- Si, Cr, Fe and Ni are the main elements present in the oxide scale for both alloys and the growth order could be related with Ellingham diagrams theory.

Acknowledgments

This work was financially supported by the Coordination for the Improvement of Higher Education Personnel – CAPES (grant number 88887.302880/2018-00, PROBRAL project 88881.143948/2017-01 and Finance Code 01) and by the German Academic Exchange Service – DAAD (project DAAD PPP-Brazil 2018 – ID 57390937). The authors are grateful to Mr. Christoph Pauly for assistance with oxide scale copper covering process, K. Aristizabal and M. A. Guitar for SEM/EDX analyses (UdS - Germany).

References

[1] M. Abbasi, I. Park, Y. Ro, Y. Ji, R. Ayer, J.H. Shim. (2019). G-phase formation in twenty-years aged heat-resistant cast austenitic steel reformer tube. *Mater. Charact.* 148, 297–306. DOI: 10.1016/j.matchar.2019.01.003.

[2] N. Madern, J. Monnier, R. Baddour-Hadjean, A. Steckmeyer, J.M. Joubert. (2018). Characterization of refractory steel oxidation at high temperature. *Corros. Sci.* 132, 223–233. DOI: 10.1016/j.corsci.2017.12.029.

[3] S.Y. Kondrat'ev, V.S. Kraposhin, G.P. Anastasiadi, A.L. Talis. (2015). Experimental observation and crystallographic description of M7C3 carbide transformation in Fe-Cr-Ni-C HP type alloy. *Acta Mater.* 100, 275–281. DOI: 10.1016/j.actamat.2015.08.056.

[4] M.P. Dewar, A.P. Gerlich. (2013). Correlation between experimental and calculated phase fractions in aged 20Cr32Ni1Nb austenitic stainless steels containing nitrogen. *Metall. Mater. Trans. A Phys. Metall. Mater. Sci.* 44, 627–639. DOI: 10.1007/s11661-012-1457-1.

[5] C. Pascal, M. Braccini, V. Parry, E. Fedorova, M. Mantel, D. Oquab, D. Monceau. (2017). Relation between microstructure induced by oxidation and room-temperature mechanical properties of the thermally grown oxide scales on austenitic stainless steels. *Mater. Charact.* 127, 161–170. DOI: 10.1016/j.matchar.2017.03.003.

[6] H. Chen, H. Wang, Q. Sun, C. Long, T. Wei, S.H. Kim, J. Chen, C. Kim, C. Jang. (2018). Oxidation behavior of Fe-20Cr-25Ni-Nb austenitic stainless steel in high-temperature environment with small amount of water vapor. *Corros.*

Sci. 145, 90–99. DOI: 10.1016/j.corsci.2018.09.016.

[7] X. Zhang, D. Li, Y. Li, S. Lu. (2019). Effect of aging treatment on the microstructures and mechanical properties evolution of 25Cr-20Ni austenitic stainless steel weldments with different Nb contents. *J. Mater. Sci. Technol.* 35, 520–529. DOI: 10.1016/j.jmst.2018.10.017.

[8] N. Birks, G.H. Meier, F.S. Pettit. (2006). Introduction to the high temperature oxidation of metals, Second edition. *Cambridge university press.* DOI: 10.1017/CBO9781139163903.

[9] D. sheng Li, Q. xun Dai, X. nong Cheng, R. rong Wang, Y. Huang. (2012). High-Temperature Oxidation Resistance of Austenitic Stainless Steel Cr18Ni11Cu3Al3MnNb. *J. Iron Steel Res. Int.* 19, 74–78. DOI: 10.1016/S1006-706X(12)60103-4.

[10] A.A. Kaya. (2002). Microstructure of HK40 alloy after high-temperature service in oxidizing/carburizing environment: II. Carburization and carbide transformations. Mater. Charact. 49, 23–34. DOI: 10.1016/S1044-5803(02)00284-X.

[11] H. Li, B. Zhang, Z. Jiang, S. Zhang, H. Feng, P. Han, N. Dong, W. Zhang, G. Li, G. Fan, Q. Lin. (2016). A new insight into high-temperature oxidation mechanism of super-austenitic stainless steel S32654 in air. *J. Alloys Compd.* 686, 326–338.DOI: 10.1016/j.jallcom.2016.06.023.

[12] M. Salehi Doolabi, B. Ghasemi, S.K. Sadrnezhaad, A. Feizabadi, A. HabibollahZadeh, D. Salehi Doolabi, M. AsadiZarch. (2017). Comparison of Isothermal with Cyclic Oxidation Behavior of “Cr-Aluminide” Coating on Inconel 738LC at 900 °C. *Oxid. Met.* 87, 57–74. DOI: 10.1007/s11085-016-9657-5.

[13] L.H. De Almeida, A.F. Ribeiro, I. Le May. (2002). Microstructural characterization of modified 25Cr-35Ni centrifugally cast steel furnace tubes. *Mater. Charact.* 49, 219–229. DOI: 10.1016/S1044-5803(03)00013-5.

[14] K. Nishimoto, K. Saida, M. Inui, M. Takahashi. (2001). Changes in microstructure of HP-modified, heat-resisting cast alloys under long-term aging. Repair weld cracking of service-exposed, HP-modified, heat-resisting cast alloys (2nd report). *Weld. Int.* DOI: 10.1080/09507110109549397.

[15] J.M. Joubert, W. St-Fleur, J. Sarthou, A. Steckmeyer, B. Fournier. (2014). Equilibrium characterization and thermodynamic calculations on highly alloyed refractory steels. *Calphad Comput. Coupling Phase Diagrams Thermochem.*

46, 55–61. DOI: 10.1016/j.calphad.2014.02.002.

[16] P.A. Ramos, R.S. Coelho, H.C. Pinto, F. Soldera, F. Mücklich, P.P. Brito. (2021). Microstructure and cyclic oxidation behavior of modified Nb-alloyed A297 HH refractory austenitic stainless steel. *Mater. Chem. Phys.* 263, 124361. DOI: 10.1016/j.matchemphys.2021.124361.

[17] P. Ramos, R.S. Coelho, F. Soldera, H.C. Pinto, F. Mücklich, P. Brito. (2020). Residual stress analysis in thermally grown oxide scales developed on Nb-alloyed refractory austenitic stainless steels. *Corros. Sci.* 178, 109066. DOI: 10.1016/j.corsci.2020.109066.

[18] E. McCafferty. (2010). Introduction to corrosion science. *Springer Science & Business Media.* DOI: 10.1007/978-1-4419-0455-3.

5 ARTICLE 3 - RESIDUAL STRESS ANALYSIS IN THERMALLY GROWN OXIDE SCALES DEVELOPED ON NB-ALLOYED REFRACTORY AUSTENITIC STAINLESS STEELS

The chapter 5 refers to the results obtained in this article mentioned in the title of the chapter. It was written in article format and the format followed the guidelines of the journal.

Authors:

Ramos, P. A., Coelho, R.S., Pinto, H.C., Soldera, F., Mücklich, F., Brito, P. P.

Paper published by Corrosion Science

RAMOS, P. *et al*. Residual stress analysis in thermally grown oxide scales developed on Nb-alloyed refractory austenitic stainless steels. **Corrosion Science**, v. 178, p. 109066, 2021.

Residual stress analysis in thermally grown oxide scales developed on Nb-alloyed refractory austenitic stainless steels

Abstract

Reliable high temperature operation of refractory metals depends on the mechanical integrity of the protective oxide formed on the material surface. The residual stress state in oxide layers developed on two modified Nb-alloyed ASTM A297 HH austenitic stainless steels, thermal expansion analysis of the substrate, steel microstructure, oxide layers morphology and phases composition were analyzed. The experimental analyses revealed that larger Nb additions increased NbC precipitates, which was connected to lower thermal expansion coefficient of the substrate. Despite similarities in the oxide scales, the higher Nb-alloyed samples exhibited lower magnitude residual stress values and larger spallation after long-term oxidation.

Key-Words: Heat resistant steel; residual stress analysis, niobium; high temperature oxidation; thermal expansion.

5.1 Introduction

The ASTM A297 austenitic stainless steels are classified as “refractory steels” and are used in applications that require elevated oxidation resistance and mechanical strength at high temperatures (> 900 °C) [1]. It is known from classical oxidation theory that the oxidation resistance of these steels depends on the formation of a protective oxide layer [2,3], which acts as a diffusion barrier preventing interactions between oxidative or corrosive environments with the underlying metallic substrate [4–7]. The high temperature mechanical strength is established with the presence of carbides dispersed in the austenitic matrix. Investigations to improve the mechanical strength of A297 steels have involved investigating niobium additions, that lead to NbC formation in partial replacement of the primary chromium carbides (M_7C_3) conventionally found in these steels after solidification [8,9].

One of the main factors that influences the oxidation resistance of high temperature steels is the mechanical integrity of the surface oxide layer, which in turn depends on the internal stresses that arise naturally during the oxidation process (due to the difference in molar volume between the metallic substrate and the oxide formed on the surface) [10–13] and on the residual stresses that appear during cooling (due to the difference in the thermal expansion/contraction coefficients observed between oxide and substrate) [10,14–17].

The residual stresses generated are elevated and are associated with the appearance of flaws in the oxide layer such as cracks and spalling [18–24], compromising component lifetime in situations involving numerous heating/cooling cycles. For this reason, several studies have sought to provide mechanisms for oxidation-induced stresses and to model the level of internal stresses in oxide layers [10,14] relating, for example, substrate and layer chemical composition with factors such as: grain size, cooling rate after oxidation, diffusion coefficients in the growing oxide layers, creep in the oxide layer and/or substrate, layer thickness, and oxide/substrate morphology [25–31].

In the present study, an experimental investigation of the residual stresses in oxide scales formed on two Nb-alloyed ASTM A297 HH refractory steels is presented. The materials were selected for investigation because the presence of niobium in the substrate modifies the carbide fraction and chromium concentration in the matrix, which may in turn change oxide scale development at high temperature.

The present work differs from recent investigations of the oxidation behaviour of Nb-alloyed refractory austenitic stainless steels by emphasizing the residual stresses present in the oxide layers developed at high temperature [6,32,33]. It is expected that with this investigation it will be possible to better understand the relation between substrate chemical/physical properties and oxidation resistance.

5.2 Experimental procedure

5.2.1 Materials

The materials used in the present study were ASTM A297 HH Nb-modified refractory austenitic stainless steels (Fe24Cr12Ni) produced by FULIG® casting which are currently used in high temperature applications. The modified composition of the ASTM A297 HH steels employed here was determined by optical emission spectroscopy using a spectrometer SHIMADZU OES 5500 II and the values obtained are presented in Table 1. The addition of tungsten and cobalt was performed to improve high temperature mechanical strength and creep resistance.

Table 5. 1 - Chemical composition of the materials employed in the study (wt%)

Modified A297 Gr. HH	0.77% Nb	0.09% Nb	Standard limits (max.)
C (modified)	0.73	0.89	0.2-0.5
Si	0.97	1.23	2.00
Mn	0.55	0.50	2.00
P	0.01	0.03	0.04
S	0.00	0.03	0.04
Ni	11.09	12.12	11.0-14.0
Cr	24.79	24.42	24.0-28.0
Mo	0.32	0.12	0.5
Co (modified)	0.28	0.47	-
Nb (modified)	0.77	0.09	-
Ti (modified)	0.10	0.01	-
Fe	60.32	59.74	Balance

The substrate microstructure was analyzed by Scanning Electron Microscopy (SEM) on a JEOL JSM-IT300 equipment with Oxford X-Max 20 Energy-Dispersive X-ray (EDX) spectroscopy detector, to evaluate the influence of niobium additions in the precipitated carbide fraction. Metallographic sample preparation, prior to microstructure analysis, was performed by grinding with SiC papers #80, #180, #320, #600, #1200, #2500 and polishing with 6, 3, 1 and 0.25 µm diamond suspension.

The steels were submitted to isothermal oxidation tests in atmospheric air at 900 °C for times of 1, 5, 10, 24, 48, 120, 240, 480 and 960 hours. The samples consisted of coupons with a 10 x 10 x 10 mm surface area (individual surface area measurements were carried out for each specimen). The edges of the samples, which could generate stress concentration effects, were removed by grinding. Prior to oxidation, all sample surfaces were ground to the same finish (#1200 SiC paper) and carefully cleaned with ethanol. The mass change measurements were performed with an analytical precision balance (0.0001g resolution). A total of three samples were weighed for each oxidation time, in order to register average and standard deviation values.

The Coefficient of Thermal Expansion (CTE) of the steels was evaluated by dilatometry tests, performed on a horizontal dilatometer NETZSCH DIL 402 C on samples with 0.09 and 0.77% Nb. The test was carried out with a controlled argon flow, with heating and cooling rates of 10°C/min and a 30-minute threshold at 1100°C.

5.2.2 Oxide layer characterization

In order to preserve oxide layer integrity during sample preparation and raise electrical conductivity for electron microscopy analyses, protective copper coatings were applied before mounting. The process consisted of depositing an Au-Pd 20 nm layer by plasma sputtering, which was accomplished by employing a 0.01 mbar pressure at 20-25 mA for 5 minutes. Subsequently, a 10 µm copper layer was electrochemically deposited by polarizing the samples in a 20g $CuSO_4$ + 100g H_2O solution, with a voltage of 1.5V DC for 12 minutes. The samples were embedded in high-strength conductive resin, ground and polished down to a 1 µm finish with OPS.

The oxide layers thickness was determined from cross section analyses of the oxidized samples performed by optical microscopy. The images were initially treated

using AxioVision® software. The thickness values were obtained by using automatic pixel counting routine in Matlab®. A total of three micrographs were recorded for each oxidation time in which a 100 μm oxide length visible. Thus, the oxide layer thickness measurements represent a total analyzed length of 300 μm. By analyzing differences in image contrast associated with composition variations in the oxide scale (determined by SEM/EDS), it was possible to evaluate the thickness of Cr_2O_3 and Fe-oxides separately.

The layer cross-section, oxide morphology and chemical composition were characterized SEM in a dual-beam workstation (FIB/SEM – FEI Helios NanoLab 600). The micrographs were made in the primary (BSE) and secondary (SE) electron mode with a voltage of 15KV.

Phase analyses of the oxide layers were performed by X-ray Diffraction (XRD) using an Empyrean PANalytical diffractometer with a Co-K_α radiation source operating at 40 KV in a 2θ range of 20° to 80° in the symmetrical Bragg Brentano geometry.

5.2.3 Residual stress analysis

The residual stress analyses were performed using the Empyrean PANalytical diffractometer operating with radiation source Cr-K_α wavelength. For the oxide layers developed after 120, 240, 480 and 960 hours, the residual stress state in the thermally grown oxide layers was determined experimentally by XRD using the conventional $\sin^2\psi$ method. The Cr_2O_3 (116), Fe_2O_3 (116) and Fe_3O_4 (440) reflections were selected and the values of the elastic constant values used for stress calculation (½S_2) were, respectively, 6.23×10^{-6}, 5.29×10^{-6} and 7.61×10^{-6} MPa^{-1}. For shorter oxidation times (up to 120 hours), because of reduced oxide layer thickness, the residual stresses were determined by using the $\sin^2\psi$ method with grazing incidence [34]. In these cases, the only assessable diffraction line was found to be the Cr_2O_3 (116) reflection. Under grazing incidence, the residual stress values are determined by a linear regression analysis relating the lattice strain with the term $\cos^2\alpha \sin^2\psi$, following in the form of Equation 1:

$$\varepsilon_{\alpha\psi} = \tfrac{1}{2}S_2\sigma\cos^2\alpha\sin^2\psi + \tfrac{1}{2}S_2\sigma\sin^2\psi - S_1\sigma \quad (1)$$

In which: $\varepsilon_{\alpha\psi}$ is the experimentally determined lattice strain, α is the difference between the diffraction angle and the grazing incidence angle, ψ is the angle between the sample surface and the diffraction plane normal, σ is the in plane surface stress and S_1, $\frac{1}{2}S_2$ are the X-ray elastic constants.

5.3 Results and discussions

5.3.1 Steel characterization

The microstructure of steels containing 0.09% and 0.77% Nb after aging at 900°C is compared in Figures 1(a) and 1(b), respectively. In both cases, it can be seen that the microstructure is formed by an austenitic matrix, with chromium carbides dispersion. By increasing niobium content precipitation of NbC takes place [1,35], causing a general reduction in the amount of primary chromium carbides. The NbC presence can be visualized with higher magnification in Figure 2(b) obtained in BSE mode, where the difference in chemical composition of the carbides allows the identification of the niobium carbides in the material interdendritic region (heavier elements appear with brighter contrast). The formation of NbC leads to an increase in the amount of chromium in solution, which in turn results in the formation of secondary chromium carbides after aging.

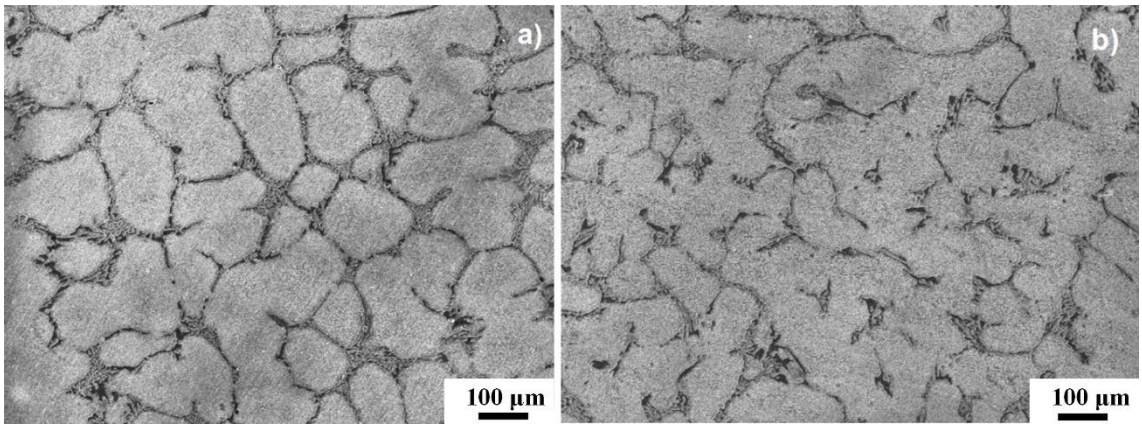

Figure 5. 1 – Microstructure of the aged (480 hours at 900°C) steels: (a) 0.09%Nb (b) 0.77%Nb.

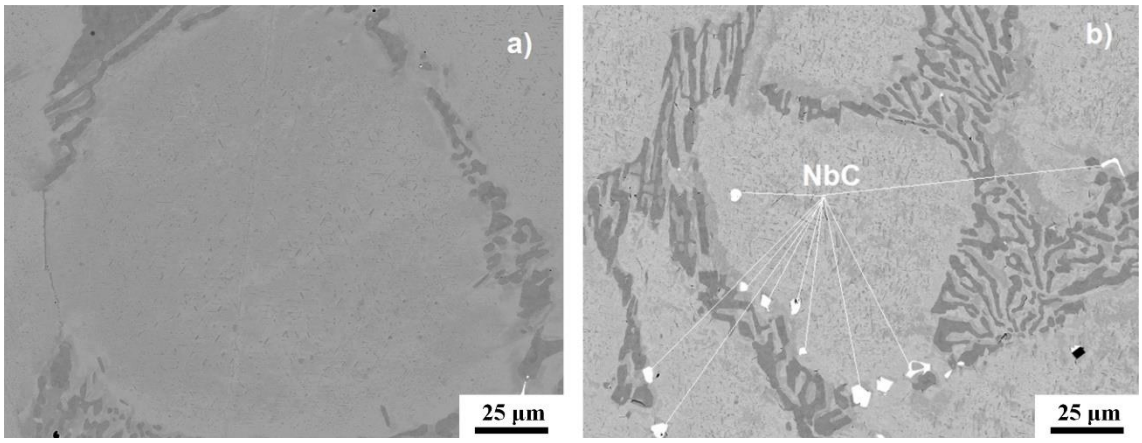

Figure 5. 2 – Microstructure of aged (480 hours at 900°C) steels evidencing the presence of niobium carbides: (a) 0.09%Nb and (b) 0.77%Nb

The thermal behavior of steels containing 0.09% and 0.77%Nb is compared in Figure 3, in which the results of dilatometry tests are presented in terms of the relative length variation (dL/L0) with temperature (T). The temperature specific CTE values were determined from the results shown in Figure 3 by applying Equation 2 [36]. Mean CTE values (±5°C) obtained at different temperatures for both steels for the cooling cycle of the dilatometry tests are compared in Table 2. The values registered here are consistent with existing literature [37], that reports CTE values between 12.4 and 13 x 10^{-6} K^{-1} for an Fe–17Cr at 750°C.

$$CTE = \frac{dx(T)}{x(T)dT} \quad (2)$$

Both tested steels exhibited similar behavior during the heating stages of the dilatometry experiments and for the steel containing lower niobium content, thermal contraction was found to be equivalent to thermal expansion. However, the alloy containing 0.77%Nb developed smaller tendency to thermal contraction during cooling compared to its own heating cycle and the overall behavior of the 0.09%Nb steel. This can be considered an indirect consequence of the presence of NbC in the 0.77%Nb alloy. With higher chromium availability, secondary chromium carbide precipitation takes place causing an increase in the steels refractive behavior.

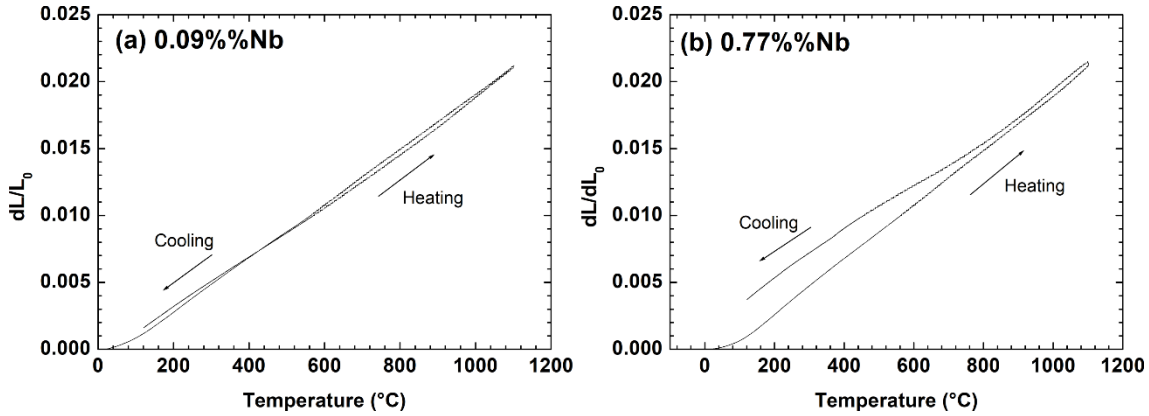

Figure 5. 3 - Relative length variation (dL/L0) per temperature (T) curves obtained by dilatometry for the 0.09%Nb and 0.77%Nb alloys.

For both steels, it can be noticed that the thermal expansion coefficient increases with temperature and that with the higher niobium content in the alloy, lower values were observed consistently in the entire temperature range investigated.

Table 5. 2 - Different linear substrate expansion coefficient for an average value of temperature around ±5°C.

Temperature (°C)	0.09%Nb - α(°C^{-1})	0.77%Nb - α(°C^{-1})
900	2.15E-05	1.90E-05
750	1.98E-05	1.65E-05
600	1.91E-05	1.48E-05
450	1.82E-05	1.64E-05
25	4.04E-06	2.31E-06

5.3.2 Oxide layer characterization

The evolution of oxide layer thickness and mass as a function of oxidation time at 900°C for times up to 960 hours is registered in Figure 4(a) and 4(b), respectively. Regarding the results presented in Figure 4(a), it can be seen that in both steels the oxide layers increase in thickness up to 240 hours of oxidation at 900°C. For longer times, the overall oxide scale formed in the alloy containing

0.77%Nb remains approximately 15 µm thick while in the alloy containing 0.09%Nb a thickness reduction to about 10 µm is observed. The results presented in Fig. 4(a) also show that the Cr_2O_3 layers developed on both alloys present similar evolution, reaching thickness values between 4 and 6 µm which remain relatively unchanged for oxidation times superior to 120 hours. Consequently, the increase in overall oxide scale thickness for longer oxidation times is due to the formation of Fe-oxides. Concurrently, the variation in mass gain presented in Figure 4(b) reveals a negative trend for the overall oxide mass starting at 48 hours oxidation. This was noticed to be connected with spallation of the oxide scales, which became severe starting from 120 hours oxidation and remained throughout the remainder of the oxidation process. Spallation was observed when removing samples of the oxidizing environment, and is indicated in Fig. 4(b). At 960 hours oxidation, significant mass loss caused by spallation was noticed for both alloys, with higher mass loss values observed for the 0.77% Nb alloy. The oxide scales remained continuous even with the mass-loss noticed in Fig. 4(b), indicating the formation of new oxides as spallation takes place.

Phase analyses by XRD is presented in Figure 5 for the oxide layers formed on both steels from 1 to 960 hours of isothermal oxidation at 900°C. It is possible to notice that up to 120 hours oxidation, for both steels, the oxide layers are comprised of mostly Cr_2O_3, and as oxidation progresses the formation of Fe oxides take place with the presence of Fe_3O_4 and Fe_2O_3. In the case of the 0.09%Nb steel, analysed in Figure 5(a), the Fe oxides might even be considered the predominant phases in the oxide scale given the relative intensity of the respective diffraction lines at 240 hours oxidation. For the 0.77%Nb steel, on the other hand (Figure 5(b)), while the Fe_3O_4 (311) peak is visible at 240 hours oxidation, Cr_2O_3 is still apparently the main constituent. With 480 hours oxidation, the phase composition of the oxide layers formed on both steels are similar.

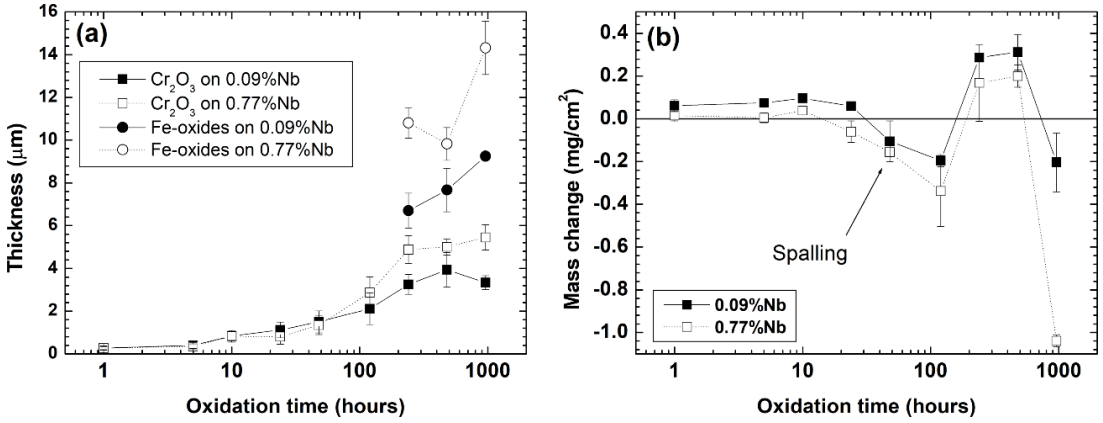

Figure 5. 4 – Oxidation behaviour of the 0.09 and 0.77%Nb alloyed steels at 900°C in atmospheric air: (a) evolution of Cr and Fe-oxide layer thickness and (b) mass change.

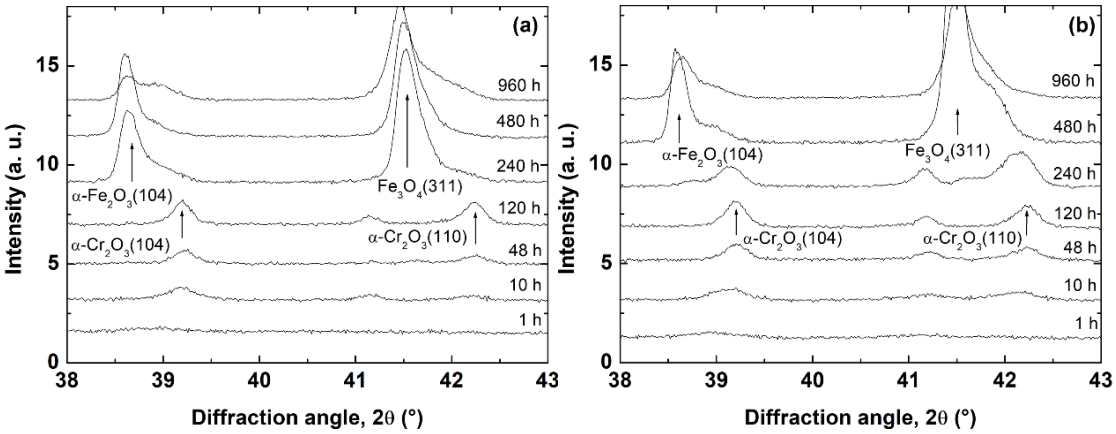

Figure 5. 5 – XRD phase analysis of oxide layers obtained after isothermal oxidation at 900°C for the: (a) 0.09%Nb and (b) 0.77%Nb steel.

More information on the oxide scale evolution is presented in Figure 6, which shows SEM/EDX analyses performed on the cross-section of samples oxidized at 900°C for different times (120, 240 and 960 hours). Consistent with the XRD results presented in Figure 5, the SEM/EDX analyses shown in Figs. 6(a) and 6(b) evidence that in the beginning of the oxidation process (up to 120 hours oxidation) a single Cr_2O_3 layer is present on the steel surface, with no signs of iron or nickel appearing in the oxide scale. It is possible to notice the presence of small amounts silicon and oxygen at the Cr_2O_3/metal interface, suggesting internal oxidation of the alloy with the formation of SiO_2, as observed recently for the oxidation of refractory steels at 1000°C [6].

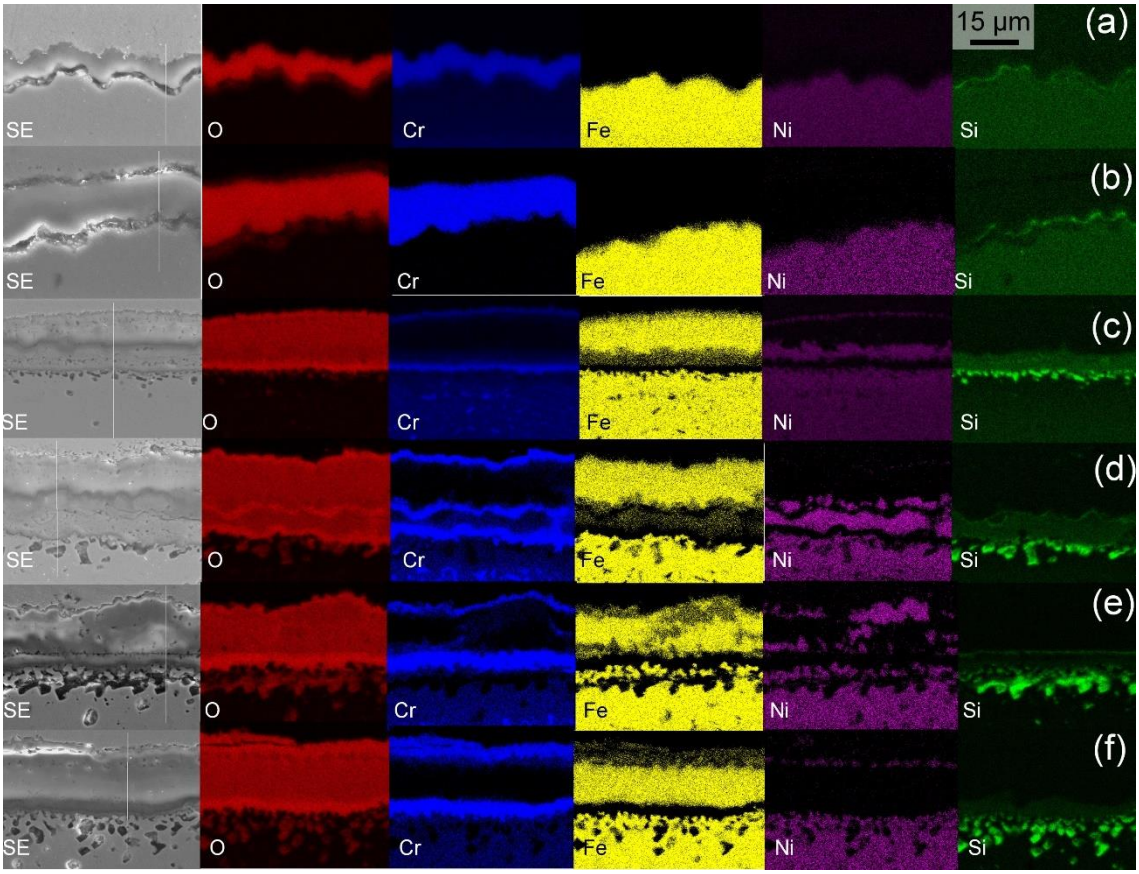

Figure 5. 6 – Cross-section SEM/EDX analyses of the oxide scales developed on the 0.09%Nb steel after (a) 120, (c) 240 and (e) 960 hours and on the 0.77%Nb steel after (b) 120, (d) 240 and (f) 960 hours oxidation at 900°C.

With increasing oxidation time to 240 and 960 hours, the presence of iron and nickel can be detected in the oxide scale, which assumes a multi-layered configuration, with Cr-oxides located at the metal/oxide and oxide/gas interface and Fe-oxides forming an intermediate layer within the oxide scale. It is important to mention that the Cr_2O_3 thickness evolution shown in Fig. 4(a) corresponds to the inner layer, which was noticed for all oxidation times. In addition, the Si-oxide particles coarsen (while remaining restricted to the Cr_2O_3/metal interface). While no signs of Mn-oxides could be identified, as has been noticed for steels containing larger manganese content [38], the development of Fe-oxides is also consistent with previous investigations of refractory austenitic stainless steels, which have shown multi-layered oxide scales consisting in general of an inner Cr_2O_3 layer and outer Fe-oxide (or spinel) phases [6,32].

The formation of Fe-oxides can be linked to the increase in oxidation rate observed after 120 hours oxidation in Figure 4(a) and 4(b), both in terms of oxide

layer thickness and the total mass gain. According to Kim *et al*. [39], once the formation of the initial Cr_2O_3 layer is complete, oxidation progresses by outward diffusion of other ions through the innermost oxide layer, as the diffusion coefficients in Cr_2O_3 decrease in the order $D_{Fe} > D_{Ni} > D_{Cr}$ [39,40]. The question remains concerning the presence of Cr_2O_3 at the oxide/gas interface. It is possible to speculate that these oxides are formed with re-oxidizing after spallation, but further analyses would be necessary to elucidate this matter.

The oxide scales developed after 960 hours are further analysed by EBSD in Figure 07. Because Fe_2O_3 and Cr_2O_3 share the same crystal structure and have similar lattice parameters, it was not possible to discern one oxide phase from the other while indexing the EBSD phase/texture maps presented in Figure 7, and both phases are identified as "Fe_2O_3". As such, it is necessary to consider the chemical composition distribution registered in Figure 6 along with the phase identification when analysing Figure 7. With this in mind, it is possible to notice that the Cr_2O_3 remains close to the metal/oxide interface and is composed of fine columnar grains, oriented along the oxide growth direction. The intermediate Fe-oxide layers are composed of both Fe_3O_4 and Fe_2O_3. This multi-layered configuration in which most Cr_2O_3 remains below the relatively thicker layers of Fe-oxides explains why the Cr_2O_3 diffraction lines became weaker over oxidation time (Figure 5). It is also worth noticing that the results presented in Figure 7 do not indicate the presence of a strong crystallographic texture in the oxide layers, which could hinder residual stress analyses by the $\sin^2\psi$ method.

Even though NbC formation was noticed for the 0.77%Nb alloy, as seen in Figure 2, it is possible to state that the amounts formed were not sufficient to significantly alter Cr-carbide precipitation and consequently the amount of chromium in solution. Considering that no Nb-oxide phases could be detected in the oxide scale or close to its interface with the metal substrate and the similar evolution of the oxidation process observed for both steels (Figs. 4 and 5), it is possible to state that in the investigated conditions the variation in Nb content did not lead to significant differences in oxide scale formation of the tested materials.

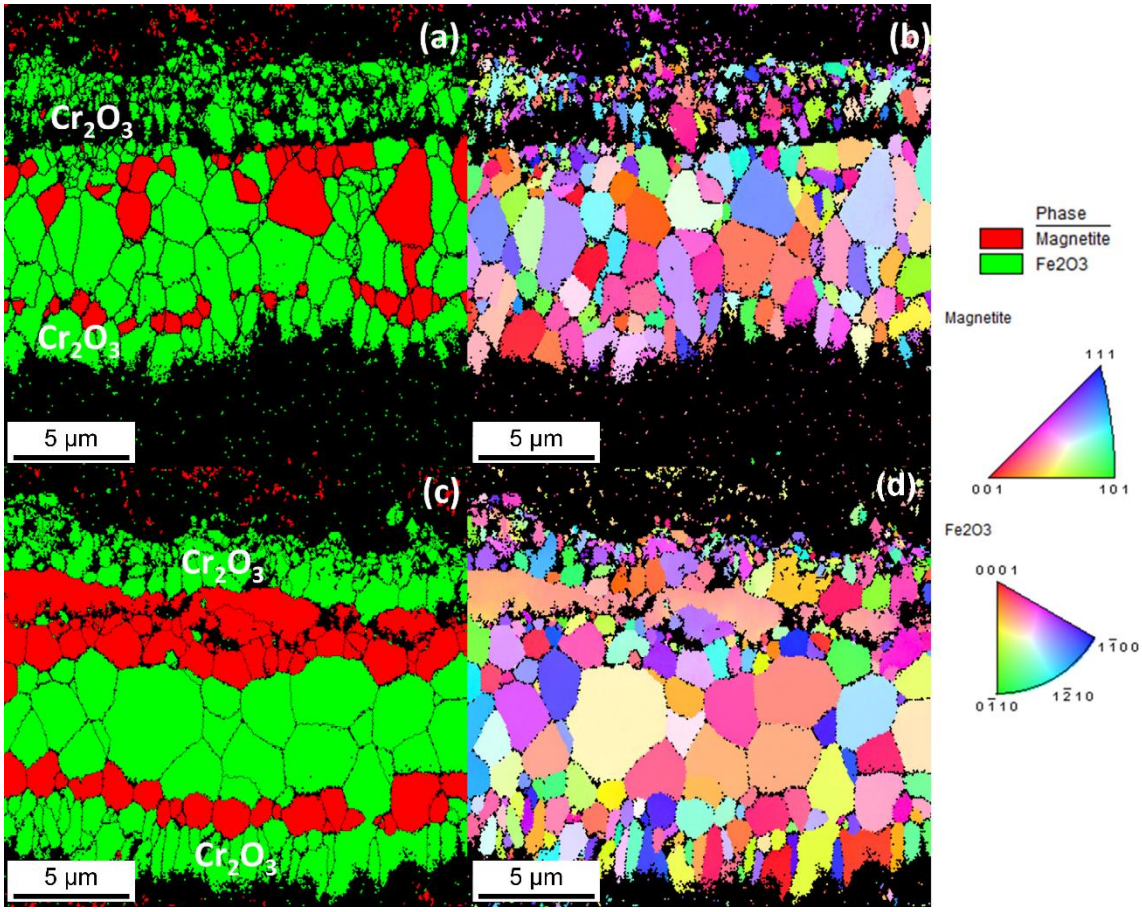

Figure 5. 7 – Cross-section SEM/EBSD analyses of the oxide scales developed after 960 hours oxidation at 900°C on the 0.09%Nb steel (a) phase map, (b) inverse pole figure map; and on the 0.77%Nb steel (c) phase map, (d) inverse pole figure map.

5.3.3 Residual stress analysis

Residual stress analyses by XRD were performed in order to provide insights concerning the mechanical integrity of the oxide layers formed on the steels containing 0.09% and 0.77% Nb at 900°C and the results are presented in Figure 8(a,b). The residual stress values determined over the entire oxidation range (from 1 to 960 hours) are presented in Figure 8(a) while the residual stresses determined for the final oxidation stage (from 240 to 960 hours) are presented in Figure 8(b). The error bars shown in Figure 8 were calculated from the linear regression errors found in the $\sin^2\psi$ and grazing-incidence $\sin^2\psi$ plots.

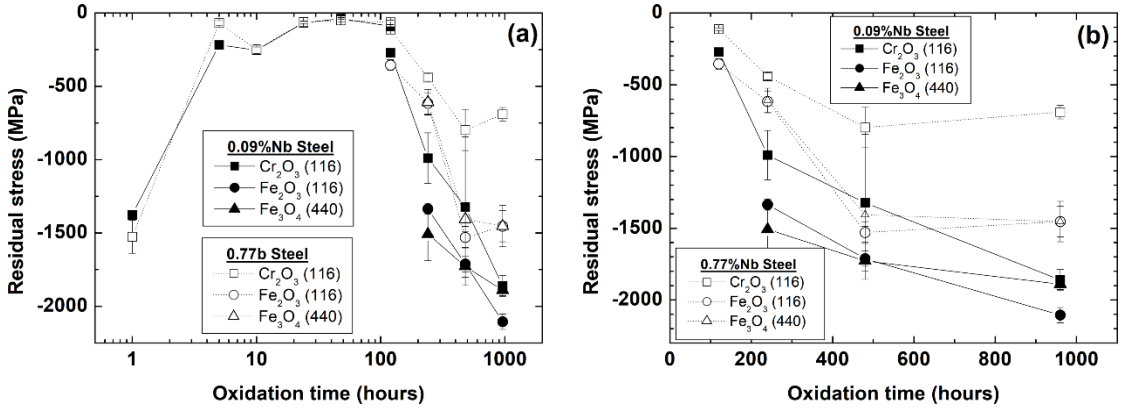

Figure 5. 8 – Residual stress evolution according to oxidation time at 900°C for the 0.09 and 0.77%Nb alloys: (a) whole oxidation range (1 to 960 hours) and (b) final oxidation stage (240 to 960 hours).

By analysing Figure 8, it is possible to notice that up to 120 hours oxidation the residual stress state in the oxide layers have a similar behaviour with oxidation time. In the very early stages of oxidation (1 hour) the residual stress level in the Cr_2O_3 layer is highly compressive (close to -1500 MPa), but shortly after the initial stages it can be seen that the stresses caused by cooling to room temperature balanced the intrinsic oxidation-induced stresses since the overall experimental results indicate low compressive residual stresses (< -300 MPa).

With the increase in oxide scale thickness after 120 hours oxidation (Figure 4), in association with the development of Fe-oxides (Figures 5 and 6) the residual stresses in the oxide scale become more compressive, with higher absolute values observed for the 0.09%Nb steel compared to the 0.77%Nb steel, as see in Figure 8(b). Particularly, after 960 hours of oxidation, stress levels in Cr_2O_3 of around -1500 and -500 MPa are perceived in the layers formed in the alloys containing 0.09%Nb and 0.77%Nb, respectively. For the remaining oxide phases, the same tendency is observed, but with a smaller relative difference in the residual stress values. These findings agree with the mass loss values reported in Fig. 4, since the larger spallation noticed for the 0.77% Nb alloy is expected to induce stress relief in the oxide scale [24].

The results presented here are in agreement with previous reports. For instance, Pantleon *et al*., [17] evaluated the residual stresses in Fe_2O_3 and Fe_3O_4 developed on coarse-grained austenitic stainless steel tubes. Although the authors report lower magnitude residual stresses (-777±94 MPa Fe_2O_3 and -592±124 MPa in

Fe_3O_4 depending on measurement direction) both oxide phases were shown to be under compression, while Mougin *et al*. [28] and Li *et al*. [20] reported residual stresses of approximately -1300GPa in Cr_2O_3 layers developed by isothermal oxidation.

According to Huntz and Schütze [10], growth stresses are relatively small during long term high temperature oxidation due to the effect of thermal relaxation by creep that occurs both in the oxide and substrate [25,30], even though in short oxidation times elevated internal stress levels are noticed [41]. Since there are no phase changes, restrictions to grain growth or even geometric restrictions that may induce stresses in initial oxidation times [20], the thermal stresses arising from CTE mismatch between substrate and oxide should account for the larger part of the overall residual stress values obtained upon cooling to room temperature after long term oxidation [10,29]. Hence, in order to evaluate whether the CTE mismatch could in fact account for the variations in residual stress values observed in Figure 9, the experimental residual stress values were compared with the theoretical values estimated according to Equation (3) [10].

$$\sigma_{ox} = \int_{T_f}^{T_i} \frac{\frac{E_{ox}(T)}{(1-\nu_{ox})}[\alpha_{ox}(T) - \alpha_m(T)]}{1 + \frac{t_{ox}}{t_m}\frac{E_{ox}(T)}{E_m(T)}\frac{1-\nu_m}{1-\nu_{ox}}} dT \quad (3)$$

Where E_{ox} is the oxide Young modulus, E_m is substrate Young modulus, t_{ox} is the oxide the layer thickness, t_m is the substrate thickness, ν_{ox} is the oxide Poisson coefficient and ν_m is the substrate Poisson Coefficient.

The theoretical stress values obtained using Eq. (3) for Cr_2O_3 and Fe_2O_3 phases (which from Figure 7 constitutes most of the intermediate Fe-rich oxide layer) are presented in Table 3. The substrate Young modulus and Poisson coefficient were considered constant with temperature and equal to 207 GPa and 0.29, respectively [42], while the CTE values were determined experimentally as a function of temperature by dilatometry (Table 2). The Young modulus of the oxides were considered equal to 290 GPa [43] and 280 GPa [43] for Cr_2O_3 and Fe_2O_3, respectively. The Poisson coefficient of the oxides was in turn considered equal to 0.33 [20] and 0.25 [44] for Cr_2O_3 and Fe_2O_3, respectively. Finally, the oxide CTE

values were calculated according to [45], as a function of the temperature. For all calculations, the values considered of oxide layer thickness (t_{ox}) were those corresponding to the final stages of oxidation (960 hours, Figure 4).

Table 5. 3 - Calculated residual stress values using Eq. (5.3)

Alloy	Cr_2O_3	Fe_2O_3
0.09%Nb	-4.78 GPa	-4.69 GPa
0.77%Nb	-3.95 GPa	-3.90 GPa

It is important to emphasize that in the present case the residual stress model is not influenced considerably by variations in thickness, since $t_{ox} << t_m$ for all oxidation times. Consequently, the model does not capture the observed variations in residual stress state with oxidation time. In addition, since only thermal effects on the residual stresses are taken into account, no stress-relief inducing mechanisms (such as creep or spallation) are considered. Therefore, it is expected that the values obtained by using Eq. (3) would indicate higher levels of compressive stresses compared to the experimental values. In spite of theses limitations, the simplified analysis does portray the tendency for larger compressive stresses following the CTE mismatch between oxide and metal substrate, which was observed in the present case, especially after 240 hours oxidation, since lower magnitude compressive residual stresses were found for both Cr_2O_3 and Fe_2O_3 on the 0.77%Nb alloy compared to the 0.09%Nb alloy. It is also significant to notice that if the CTE difference among the tested steels is in fact caused by carbide precipitation with aging, as the differences in the heating/cooling cycles of the dilatometry experiments indicated, during the initial oxidation stages similar thermal behavior is expected for both steels, which would explain the similarity in the residual stress values noticed up to 120 hours oxidation.

As such, it appears that two factors have contributed to the lower values of residual stresses determined experimentally in the oxide layers developed on the 0.77%Nb, which are the higher level of spallation (particularly after 120 hours oxidation) and the lower CTE mismatch between oxide and substrate noticed for this steel in comparison to the 0.09%Nb alloy.

5.4 Conclusions

In the present work, the microstructure, thermal properties of two ASTM A297 HH austenitic stainless steels with niobium additions (0.09 and 0.77%Nb) was analysed in an attempt to analyse the influence of these parameters on the oxidation behavior of the materials, specifically the residual stress state in the oxide layers. The following conclusions could be drawn:

- The two alloys presented similar microstructures concerning the austenitic matrix, but variations regarding carbide precipitations (with larger amounts of NbC in the 0.77%Nb alloy);
- The larger niobium content was associated with lower CTE values, as evaluated during the cooling stage in dilatometry measurements;
- Both steels presented similar mass gain in the beginning of the oxidation process, but in further stages larger spallation was observed for the 0.77%Nb alloy, particularly after 960h oxidation.
- The steel with higher niobium content exhibited lower magnitude residual stresses after long term oxidation, consistent with the lower CTE values observed for the 0.77%Nb alloy compared to the 0.09%Nb alloy.

5.5 Data availability statement

The raw/processed data required to reproduce these findings cannot be shared at this time as the data also forms part of an ongoing study.

Acknowledgments

The authors acknowledge support from FULIG® casting for providing the cast materials and Sebastian Slawik (UdS Germany) for assistance with residual stress analysis. This work was financially supported by the Coordination for the Improvement of Higher Education Personnel – CAPES (grant number 88887.302880/2018-00, PROBRAL project 88881.143948/2017-01 and Finance Code 01) and by the German Academic Exchange Service – DAAD (project DAAD PPP-Brazil 2018 – ID 57390937).

References

[1] M. Abbasi, I. Park, Y. Ro, Y. Ji, R. Ayer, J.H. Shim, G-phase formation in twenty-years aged heat-resistant cast austenitic steel reformer tube, Mater. Charact. 148 (2019) 297–306. https://doi.org/10.1016/j.matchar.2019.01.003.

[2] C. Wagner, Reaktionstypen bei der Oxydation von Legierungen, Zeitschrift Fuer Elektrochemie. 63 (1959) 772–782. https://doi.org/10.1002/bbpc.19590630713.

[3] G.C. Wood, The oxidation of iron-chromium alloys and stainless steels at high temperatures, Corros. Sci. (1962) 173–196. https://doi.org/10.1016/0010-938X(62)90019-7.

[4] R.A. Holm, H.E. Evans, The resistance of 20 Cr/25 Ni steels to carbon deposition. II: Internal oxidation and carburisation, Mater. Corros. 38 (1987) 166–175. https://doi.org/10.1002/maco.19870380403.

[5] R.C. Lobb, H.E. Evans, DETERMINATION OF THE CHROMIUM CONCENTRATION FOR “HEALING” LAYER FORMATION DURING THE OXIDATION OF CHROMIUM-DEPLETED 20Cr-25Ni-Nb STAINLESS STEEL., Corros. Sci. 24 (1984) 385–396. https://doi.org/10.1016/0010-938X(84)90065-9.

[6] N. Madern, J. Monnier, R. Baddour-Hadjean, A. Steckmeyer, J.M. Joubert, Characterization of refractory steel oxidation at high temperature, Corros. Sci. 132 (2018) 223–233. https://doi.org/10.1016/j.corsci.2017.12.029.

[7] C. Pascal, M. Braccini, V. Parry, E. Fedorova, M. Mantel, D. Oquab, D. Monceau, Relation between microstructure induced by oxidation and room-

temperature mechanical properties of the thermally grown oxide scales on austenitic stainless steels, Mater. Charact. 127 (2017) 161–170. https://doi.org/10.1016/j.matchar.2017.03.003.

[8] G.D. de Almeida Soares, L.H. de Almeida, T.L. da Silveira, I. Le May, Niobium additions in HP heat-resistant cast stainless steels, Mater. Charact. 29 (1992) 387–396. https://doi.org/10.1016/1044-5803(92)90045-J.

[9] G.D. Barbabela, L.H. de Almeida, T.L. da Silveira, I. Le May, Role of Nb in modifying the microstructure of heat-resistant cast HP steel, Mater. Charact. 26 (1991) 193–197. https://doi.org/10.1016/1044-5803(91)90053-7.

[10] A.M. Huntz, M. Schütze, Stresses generated during oxidation sequences and high temperature fracture, Mater. High Temp. 12 (1994) 151–161. https://doi.org/10.1080/09603409.1994.11689481.

[11] C. Xu, W. Gao, Pilling-bedworth ratio for oxidation of alloys, Mater. Res. Innov. 3 (2000) 231–235. https://doi.org/10.1007/s100190050008.

[12] K.C. Chou, Q. Luo, Q. Li, J.Y. Zhang, Influence of the density of oxide on oxidation kinetics, Intermetallics. 47 (2014) 17–22. https://doi.org/10.1016/j.intermet.2013.11.024.

[13] S. Leleu, B. Rives, J. Bour, N. Causse, N. Pébère, On the stability of the oxides film formed on a magnesium alloy containing rare-earth elements, Electrochim. Acta. 290 (2018) 586–594. https://doi.org/10.1016/j.electacta.2018.08.093.

[14] F. Rakotovao, B. Panicaud, J.L. Grosseau-Poussard, Z. Tao, G. Geandier, P.O. Renault, P. Girault, P. Goudeau, N. Blanc, N. Boudet, G. Bonnet, In situ Synchrotron X-Ray diffraction study of high-temperature stress relaxation in chromia scales containing the reactive element yttrium, Acta Mater. 159 (2018) 276–285. https://doi.org/10.1016/j.actamat.2018.07.055.

[15] D. Fettré, S. Bouvier, J. Favergeon, L. Kurpaska, Residual stresses in high temperature corrosion of pure zirconium using elasto-viscoplastic model: Application to the deflection test in monofacial oxidation, Appl. Surf. Sci. 357 (2015) 777–786. https://doi.org/10.1016/j.apsusc.2015.08.225.

[16] Y. Suo, Z. Zhang, X. Yang, Residual stress analysis with stress-dependent growth rate and creep deformation during oxidation, J. Mater. Res. 31 (2016) 2384–2391. https://doi.org/10.1557/jmr.2016.262.

[17] K. Pantleon, M. Montgomery, Phase identification and internal stress analysis

of steamside oxides on plant exposed superheater tubes, in: Metall. Mater. Trans. A Phys. Metall. Mater. Sci., 2012: pp. 1477–1486. https://doi.org/10.1007/s11661-011-0874-x.

[18] V.K. Tolpygo, D.R. Clarke, Alumina scale failure resulting from stress relaxation, in: Surf. Coatings Technol., 1999: p. 7. https://doi.org/10.1016/S0257-8972(99)00331-X.

[19] B.R. Barnard, T.R. Watkins, P.K. Liaw, An evaluation of the use of X-ray residual stress determination as a means of characterizing oxidation damage of nickel-based, Cr 2O 3-forming superalloys subjected to various oxidizing conditions, Oxid. Met. 74 (2010) 305–318. https://doi.org/10.1007/s11085-010-9214-6.

[20] N. Li, J. Xiao, N. Prud'homme, Z. Chen, V. Ji, Residual stresses in oxide scale formed on Fe-17Cr stainless steel, Appl. Surf. Sci. 316 (2014) 108–113. https://doi.org/10.1016/j.apsusc.2014.07.195.

[21] X. Zhang, D. Li, Y. Li, S. Lu, Effect of aging treatment on the microstructures and mechanical properties evolution of 25Cr-20Ni austenitic stainless steel weldments with different Nb contents, J. Mater. Sci. Technol. 35 (2019) 520–529. https://doi.org/10.1016/j.jmst.2018.10.017.

[22] P. Chen, Z. Liu, R. Li, X. Li, The effect of manganese additions on the high temperature oxidation behaviour of the high-vanadium cast iron, J. Alloys Compd. 767 (2018) 181–187. https://doi.org/10.1016/j.jallcom.2018.07.113.

[23] Y. Wang, W. Jiang, Y. Luo, Y. Zhang, S.T. Tu, Evolution of thermal stress and failure probability during reduction and re-oxidation of solid oxide fuel cell, J. Power Sources. 371 (2017) 65–76. https://doi.org/10.1016/j.jpowsour.2017.10.034.

[24] H.E. Evans, R.C. Lobb, The influence on oxide spallation of annealing periods during a cooling cycle, Corros. Sci. 35 (1993) 999–1005. https://doi.org/10.1016/0010-938X(93)90318-B.

[25] H.E. Evans, Stress effects in high temperature oxidation of metals, Int. Mater. Rev. 40 (1995) 1–40. https://doi.org/10.1179/imr.1995.40.1.1.

[26] V.K. Tolpygo, D.R. Clarke, Spalling failure of α-alumina films grown by oxidation: I. Dependence on cooling rate and metal thickness, Mater. Sci. Eng. A. 278 (2000) 142–150. https://doi.org/10.1016/S0921-5093(99)00581-X.

[27] V.K. Tolpygo, D.R. Clarke, Spalling failure of α-alumina films grown by

oxidation. II. Decohesion nucleation and growth, Mater. Sci. Eng. A. 278 (2000) 151–161. https://doi.org/10.1016/s0921-5093(99)00582-1.

[28] J. Mougin, N. Rosman, G. Lucazeau, A. Galerie, In situ Raman monitoring of chromium oxide scale growth for stress determination, J. Raman Spectrosc. 32 (2001) 739–744. https://doi.org/10.1002/jrs.734.

[29] L. Antoni, J. Mougin, A. Galerie, M. Dupeux, N. Rosman, G. Lucazeau, A.M. Huntz, In-situ determination of growth and thermal stresses in chromia scales formed on a ferritic stainless steel, Mater. Corros. 53 (2002) 486–490. https://doi.org/10.1002/1521-4176(200207)53:7<486::AID-MACO486>3.0.CO;2-P.

[30] M.P. Taylor, H.E. Evans, E.P. Busso, Z.Q. Qian, Creep properties of a Pt-aluminide coating, Acta Mater. 54 (2006) 3241–3252. https://doi.org/10.1016/j.actamat.2006.03.010.

[31] M.P. Taylor, H.E. Evans, C.B. Ponton, J.R. Nicholls, A method for evaluating the creep properties of overlay coatings, Surf. Coatings Technol. 124 (2000) 13–18. https://doi.org/10.1016/S0257-8972(99)00629-5.

[32] X. Zhang, D. Li, Y. Li, S. Lu, Oxidation behaviors of Fe-25Cr-20Ni-χNb austenitic weld metals at 1100 °C in ambient air: Role of elemental niobium, Corros. Sci. 159 (2019) 108137. https://doi.org/10.1016/j.corsci.2019.108137.

[33] H. Chen, H. Wang, Q. Sun, C. Long, T. Wei, S.H. Kim, J. Chen, C. Kim, C. Jang, Oxidation behavior of Fe-20Cr-25Ni-Nb austenitic stainless steel in high-temperature environment with small amount of water vapor, Corros. Sci. 145 (2018) 90–99. https://doi.org/10.1016/j.corsci.2018.09.016.

[34] C.H. Ma, J.H. Huang, H. Chen, Residual stress measurement in textured thin film by grazing-incidence X-ray diffraction, Thin Solid Films. 418 (2002) 73–78. https://doi.org/10.1016/S0040-6090(02)00680-6.

[35] S. Shi, J.C. Lippold, Microstructure evolution during service exposure of two cast, heat-resisting stainless steels - HP-Nb modified and 20-32Nb, Mater. Charact. 59 (2008) 1029–1040. https://doi.org/10.1016/j.matchar.2007.08.029.

[36] G.R. Holcomb, A review of the thermal expansion of magnetite, Mater. High Temp. 36 (2019) 232–239. https://doi.org/10.1080/09603409.2018.1520953.

[37] B. Hua, Y. Kong, W. Zhang, J. Pu, B. Chi, L. Jian, The effect of Mn on the oxidation behavior and electrical conductivity of Fe-17Cr alloys in solid oxide fuel cell cathode atmosphere, J. Power Sources. 196 (2011) 7627–7638.

https://doi.org/10.1016/j.jpowsour.2011.05.007.

[38] T. Liu, K. Zheng, J. Wang, Y. Lin, Z. Zheng, J. Long, Effect of Ce on oxidation behaviour and microstructure evolution of a nickel-saving austenitic heat-resistant cast steel, Corros. Sci. 166 (2020) 108423. https://doi.org/10.1016/j.corsci.2019.108423.

[39] J.H. Kim, B.K. Kim, D.I. Kim, P.P. Choi, D. Raabe, K.W. Yi, The role of grain boundaries in the initial oxidation behavior of austenitic stainless steel containing alloyed Cu at 700°C for advanced thermal power plant applications, Corros. Sci. 96 (2015) 52–66. https://doi.org/10.1016/j.corsci.2015.03.014.

[40] R.E. Lobnig, H.P. Schmidt, K. Hennesen, H.J. Grabke, Diffusion of cations in chromia layers grown on iron-base alloys, Oxid. Met. 37 (1992) 81–93. https://doi.org/10.1007/BF00665632.

[41] P. Brito, H. Pinto, C. Genzel, M. Klaus, A. Kaysser-Pyzalla, Epitaxial stress and texture in thin oxide layers grown on Fe-Al alloys, Acta Mater. 60 (2012). https://doi.org/10.1016/j.actamat.2011.11.033.

[42] M. Fukuhara, A. Sanpei, Elastic Moduli and Internal Friction of Low Carbon and Stainless Steels as a Function of Temperature, Isij Int. 33 (1993) 508–512. https://doi.org/10.2355/isijinternational.33.508.

[43] I. Saeki, T. Ohno, D. Seto, O. Sakai, Y. Sugiyama, T. Sato, A. Yamauchi, K. Kurokawa, M. Takeda, T. Onishi, Measurement of Young's modulus of oxides at high temperature related to the oxidation study, Mater. High Temp. 28 (2011) 264–268. https://doi.org/10.3184/096034011X13182685579795.

[44] D. Chicot, J. Mendoza, A. Zaoui, G. Louis, V. Lepingle, F. Roudet, J. Lesage, Mechanical properties of magnetite (Fe3O4), hematite (α-Fe2O3) and goethite (α-FeO·OH) by instrumented indentation and molecular dynamics analysis, Mater. Chem. Phys. 129 (2011) 862–870. https://doi.org/10.1016/j.matchemphys.2011.05.056.

[45] Y. Fei, Thermal expansion, in: Miner. Phys. Crystallogr. a Handb. Phys. Constants 2, 1995: pp. 29–44. https://doi.org/10.1029/RF002p0029.

6 FINAL CONSIDERATIONS

6.1 Summary of results

The addition of niobium revealed changes in the microstructure, forming precipitates that improve mechanical strength and generated a richer chromium austenitic matrix. However, even with higher values of chromium in solution, no significant changes were observed in the oxidation resistance through the well-knonw mass gain tests as well as in the chemical composition of the oxide layer, for the tests carried out at 900 °C and up to 960 h of isothermal and cyclic oxidation.

The precipitates were found to have induced a change in the thermal expansion coefficient of the metallic substrate, in which the addition of niobium favored a substrate lower dilatation, and hence a lower level of residual stresses in the oxide layer, promoting greater mechanical stability of the layer and, consequently, better durability of the material also through carbides thermal stability.

From the thermodynamic computational analyzes, microstructural characterization of the substrate, the multilayer oxide scale characterization, high temperature oxidation tests, residual stresses measurements and dilatometry tests the main concluions were:

- Generally the microstructure analyses performed by OM and SEM/EDX agreed with the thermodynamic simulations in Matcalc® concerning phase precipitation, carbides stoichiometry and chromium and carbon partitioning trend;
- The thermodynamic simulations indicated that the presence of niobium led to an overall decrease of the chromium carbide fraction, while increasing NbC as well as increase carbides stability at high temperatures.
- The observed morphology by microstructural characterization and localized chemical composition analyses suggested the presence of M_7C_3, $M_{23}C_6$, NbC and (Ti,Nb)C carbides in as-cast and aged conditions.
- The Solidification model proposed by Scheil showed secondary chromium carbides ($M_{23}C_6$) which appeared after the primary ones. However, in phase diagrams are the more stable form found after high temperature exposure when compared to primary chromium carbides (M_7C_3).

- The multilayer oxide scale was composed by Fe_2O_3, $Cr_{0.03}Fe_{2.96}Ni_{0.01}O_4$ and Cr_2O_3 characterized by the XRD phase analyses and SEM/EDX analyses for both materials.
- The addition of niobium did not impair the oxidation resistance of the modified A297 HH heat-resistant austenitic stainless steel, since no noticeable differences on oxide scales and mass change was observed in this range of niobium addition (0 – 0.77 wt%) and 900°C oxidation temperature exposure;
- High temperature oxidation up to 120h was characterized by protective oxidation, after this period a non-protective oxidation started generating a multilayer Fe-based oxide scale;
  - The oxides found in this work has the following PBR ratio: Fe_2O_3 = 2.14, Fe_3O_4 = 2.10, and Cr_2O_3 = 2.07, indicating compressive stresses for all of them;
- The larger niobium content (0.77%Nb) caused carbides precipitation and was associated with lower CTE(thermal expansion coefficient) values, introducing lower residual stress state on the oxide layer of this steel as evaluated during the cooling stage in dilatometry measurements.

6.2 Suggestions for future investigations

- Analyze alloys with the least variation in chemical composition possible and with higher levels of niobium changing isolatedly to pronounce its effect;
- Conduct oxidation tests at higher temperatures in order to amplify the effects of thermal expansion and diffusion during oxide layer growth but without causing the carbides dissolution;
- Conduct oxidation tests in different atmospheres such as carburizing, sulphiting and water vapor as well as analyze the oxides formed and the mass gain of each material;
- Evaluate the microstructure and mechanical properties according to different heat treatment parameters (temperature, time and oxidation condition);
- Characterize precipitates with EBSD technique in order to provide more clearly and complete information about them;

- Conduct dilatometry tests of aged samples to deeply understand the influence of precipitation in thermal expansion coeffients;
- Analyze the chemical elements added in the alloys and the expected effects for each one of them, especially for Molybdenum and Nickel;
- Perform high temperature thermomechanical tests to analyze fluency resistance, deformation mechanisms and carbides precipitation during plastic deformation process. Also possible to investigate deformation plans and microstructural texture during deformation process conjugated with XRD and EBSD experiments.

6.3 Original contribution from this thesis

1) "Microstructure and cyclic oxidation behavior of modified Nb-alloyed A297 HH refractory austenitic stainless steel”

- Authors: Ramos, P. A., Coelho, R.S., Pinto, H.C., Soldera, F., Mücklich, F., Brito, P. P.
- Paper published by Materials Chemistry and Physics. RAMOS, P. A. *et al.* Microstructure and cyclic oxidation behavior of modified Nb-alloyed A297 HH refractory austenitic stainless steel. Materials Chemistry and Physics, v. 263, p. 124361, 2021.

2) “Oxide Layer Evolution of Cast Fe24Cr12NiXNb heat-resistant cast steels at 900°C in Atmospheric Air”
- Authors: Ramos, P. A., Coelho, R.S., Pinto, H.C., Soldera, F., Mücklich, F., Brito, P. P.
- Paper published by Archives of Foundry Engineering - RAMOS, P. A. *et al.* Oxide Layer Evolution of Cast Fe24Cr12NiXNb Heat-Resistant Cast Steels at 900° C in Atmospheric Air. Archives of Foundry Engineering, p. 119-124-119-124, 2021.

3) “Residual stress analysis in thermally grown oxide scales developed on Nb-alloyed refractory austenitic stainless steels”
- Authors: Ramos, P. A., Coelho, R.S., Pinto, H.C., Soldera, F., Mücklich, F., Brito, P. P.
- Paper published by Corrosion Science - RAMOS, P. *et al.* Residual stress analysis in thermally grown oxide scales developed on Nb-alloyed refractory austenitic stainless steels. Corrosion Science, v. 178, p. 109066, 2021.

4) “Microstructural characterization and corrosion resistance of modified austenitic stainless steel A-297 HH with niobium additions”
- Authors: Ramos, P. A., Guitar, M. A., Britz, D., Mücklich, F. and Brito, P. P. - Abstract published in the Proceedings of the 8th DocMASE Professional Summer School 2019, Saarbrücken, Germany, September, 2019.

Saarland University
PO Box 15 11 50 | 66041 Saarbrücken

To whom it may concern

Prof. Dr.-Ing. Frank Mücklich
Chairman

Dr.-Ing. Flavio Soldera
General Manager

European School of Materials
Saarland University
Campus D3₃
66123 Saarbrücken

Sekr: +49 (0) 681 302-70500
Fax: +49 (0) 681 302-70502
Website: www.eusmat.net
Email: office@eusmat.net

Contact person:
Flavio Soldera
Phone:
+49 (0)681 302-70511
E-Mail:
f.soldera@matsci.uni-sb.de

Date **27.09.2020**

Reference **Certificate of participation –**
8th DocMASE Professional Summer School 2019, Saarbrücken

To whom it may concern,

hereby it is confirmed that Mr. Pedro Augusto Ramos has successfully participated in the 8th DocMASE Summer School **"Surface Engineering: surface structuring and functional coatings"** in September 2019.

The participation included a presentation about research activities of the participants. Mr. Ramos gave an insight into the following research project:

"Microstructural characterization and corrosion resistance of modified austenitic stainless steel A-297 HH with niobium additions"

The 8th summer school took place from September 23th to 27th at the Saarland University in Saarbrücken. Well renowned experts of our consortium and from external institutions provided insights on following fields: laser structuring, mechanical finishing treatments, electroechemical machining, coatings, plasma physic in PVD processes, HiPIMS.

Yours sincerely,

Dr.-Ing. Flavio Soldera